Shock and Vibration

International Conference on Acoustics and Vibration 2012

Guest Editors: Hamid Mehdigholi, Hamid Ahmadian, and Abdolreza Ohadi

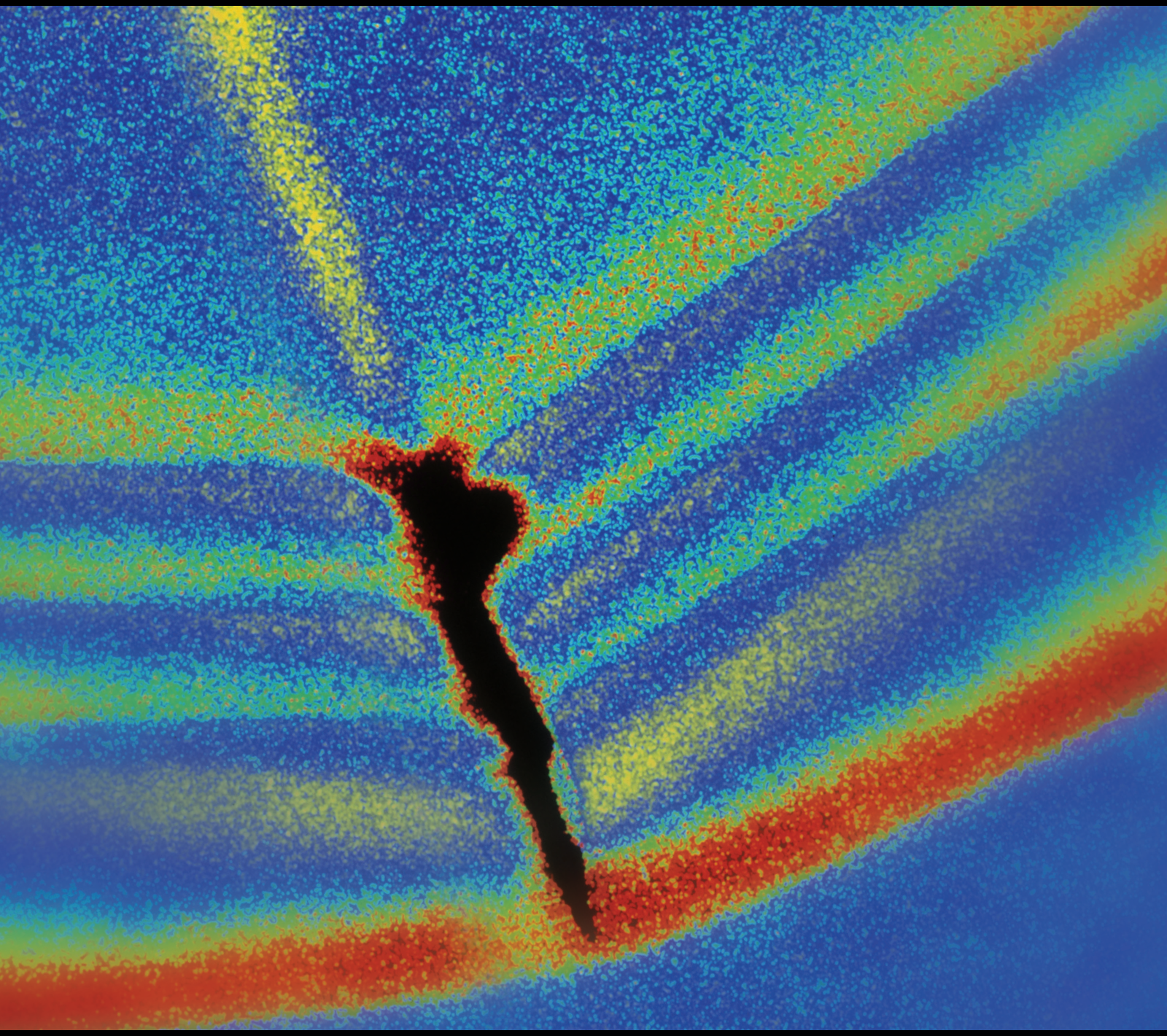

International Conference on Acoustics and Vibration 2012

Shock and Vibration

International Conference on Acoustics and Vibration 2012

Guest Editors: Hamid Mehdigholi, Hamid Ahmadian, and Abdolreza Ohadi

Contents

Hindawi Publishing Corporation
Shock and Vibration
Volume 2014, Article ID 340285, 1 page
http://dx.doi.org/10.1155/2014/340285

Editorial

International Conference on Acoustics and Vibration 2012

Hamid Mehdigholi,[1,2] Hamid Ahmadian,[3] and Abdolreza Ohadi[4]

[1] *International Communication Committee of ISAV, Iran*
[2] *Department of Mechanical Engineering, Sharif University of Technology, Tehran 14588-89695, Iran*
[3] *School of Mechanical Engineering, Iran University of Science and Technology, Narmak, Tehran 16846, Iran*
[4] *Acoustics Research Laboratory, Department of Mechanical Engineering, Amirkabir University of Technology, Hafez Avenue 424, Tehran 15916-34311, Iran*

Correspondence should be addressed to Abdolreza Ohadi; a_r_ohadi@aut.ac.ir

Received 19 November 2012; Accepted 22 November 2012; Published 10 July 2014

The Second International Conference on Acoustics and Vibration (ISAV2012) was held on December 26-27, 2012, at the Sharif University of Technology, Tehran, Iran. This is an annual conference organized by the Iranian Society of Acoustics and Vibration (ISAV) in order that the researchers and engineers share their findings and mutual concerns in this field.

The growing significance of acoustics and vibration in all branches of engineering is fully clear, which undoubtedly has led to new grounds for improving and serving the society. Vibrations, more precisely, mechanical vibrations, as the main field along with acoustics—as they complement one another—express their vitality in all aspects of engineering.

Among the 450 abstracts that were received for the conference, 280 were selected for a review process. During the review process by three experts for each paper, 243 papers were chosen for presentation at the conference. 44 papers were included in a poster session; the remaining papers were presented in 8 parallel sessions in two days. The conference Scientific Committee nominated the top research papers to be published in the special issues of a well-known journal. The committee asked the authors of the 11 selected English papers to declare their agreement and also make further improvements to their papers for Shock and Vibration journal, resulting in this special issue.

Acknowledgment

On behalf of the organizing committee of the conference, I would like to express my sincere thanks to the researchers who contributed to the success of the conference by presenting their research findings at the conference. In particular, I would like to express my appreciation to the authors of the 11 papers selected for this special issue for their archival contribution.

Hamid Mehdigholi
Hamid Ahmadian
Abdolreza Ohadi

Hindawi Publishing Corporation
Shock and Vibration
Volume 2014, Article ID 434187, 6 pages
http://dx.doi.org/10.1155/2014/434187

Research Article

Numerical Time-Domain Modeling of Lamb Wave Propagation Using Elastodynamic Finite Integration Technique

Hussein Rappel,[1] Aghil Yousefi-Koma,[1] Jalil Jamali,[2] and Ako Bahari[3]

[1] *Center of Advanced Systems and Technologies (CAST), School of Mechanical Engineering, College of Engineering, University of Tehran, Tehran 14399 57131, Iran*
[2] *Department of Mechanical Engineering, Islamic Azad University, Shushtar Branch, Shushtar, Iran*
[3] *School of Railway Engineering, Iran University of Science and Technology, Tehran 16846 13114, Iran*

Correspondence should be addressed to Aghil Yousefi-Koma; aykoma@ut.ac.ir

Received 19 October 2012; Accepted 19 November 2012; Published 10 July 2014

Academic Editor: Hamid Mehdigholi

This paper presents a numerical model of lamb wave propagation in a homogenous steel plate using elastodynamic finite integration technique (EFIT) as well as its validation with analytical results. Lamb wave method is a long range inspection technique which is considered to have unique future in the field of structural health monitoring. One of the main problems facing the lamb wave method is how to choose the most appropriate frequency to generate the waves for adequate transmission capable of properly propagating in the material, interfering with defects/damages, and being received in good conditions. Modern simulation tools based on numerical methods such as finite integration technique (FIT), finite element method (FEM), and boundary element method (BEM) may be used for modeling. In this paper, two sets of simulation are performed. In the first set, group velocities of lamb wave in a steel plate are obtained numerically. Results are then compared with analytical results to validate the simulation. In the second set, EFIT is employed to study fundamental symmetric mode interaction with a surface braking defect.

1. Introduction

Lamb wave testing technique is increasingly used for assessing defects in thin-wall structures like plate and pipes [1–3]. Lamb waves are elastic waves whose wavelength is in the same order as thickness of the structure [4]. One of the main advantages of lamb wave technique is that it allows long-range inspection in contrast to traditional ultrasonic testing, where the coverage is limited to a small area in vicinity of each transducer. Lamb waves were first described theoretically by Horace Lamb in 1917 [5]. These waves arise from coupling between shear and longitudinal waves reflected at the top and bottom edges of a thin wall structure [6]. Lamb wave theory can be found in a number of text books [7]. Defects such as corrosion and fatigue cracks cause changes in effective thickness and local material properties and therefore measurement of variations in lamb wave propagation can be used to assess the integrity of plate [1]. Successful usage of lamb waves in an inspection system needs to understand its schemes of propagation in a waveguide and its scattering at defects. Thus, there is an increasing demand for powerful, flexible, and accurate simulation techniques. First works on numerical simulation of ultrasonic waves were done by Harumi (1986) and Yamawaki and Saito (1992) who calculated and visualized bulk wave propagation [8]. Now, numerical simulation of lamb waves is possible. Common techniques which are used to simulate lamb wave propagation are finite difference time domain (FDTD) [9], finite element method (FEM) [5], boundary element method (BEM) [10], elastodynamic finite integration technique (EFIT) [11, 12], and specialized methods for guided wave calculations such as hybrid methods [13] and semianalytical finite element method (SAFEM) [8].

In this work, calculations are based on elastodynamic finite integration technique; historically, finite integration technique was introduced by Weiland in electrodynamics. Fellinger and Langenberg used Weiland's idea for governing equations of ultrasonic waves in solid, calling it EFIT [14]. EFIT is a grid based numerical time-domain method, using velocity-stress formalism, and easily treats with different

boundary conditions which are essential to model ultrasonic wave propagation [12]. Because of its relative simplicity and flexibility, Schubert et al. used EFIT equations to cylindrical coordinates (CEFIT) to simulate axisymmetric wave propagation in pipes with a 2D grid [15]. Schubert also used finite integration technique to simulate elastic wave propagation in porous concrete and showed efficiency of EFIT to model a diverse range of applications [16].

Two sets of simulation results are presented in this work using a program developed in MATLAB environment. In the first one, lamb wave propagation in a 2D steel plate is discussed. Results are then compared with analytical results to validate the accuracy of modeling and, in the second example, interaction lamb wave with a surface breaking defect is investigated.

2. The Elastodynamic Finite Integration Technique for Linear Elastics

2.1. Governing Equations. The governing equations of elastic waves in a general media are the Cauchy equation of motion and equation of deformation rate. These equations are given in integral form for a finite volume V and surface S as follows:

$$\frac{\partial}{\partial t}\int_V \rho v_i dV = \int_S T_{ij} n_i dS + \int_V f_i dV, \tag{1}$$

$$\frac{\partial}{\partial t}\int_V s_{ijkl} T_{kl} dV = \frac{1}{2}\int_S \left(v_i n_j + v_j n_i\right) dS, \tag{2}$$

where v is the particle velocity vector, T is stress tensor, ρ is density, n is the outward normal vector on surface S, f is the body force vector, and s is the compliance tensor. The inverse of s is the stiffness tensor c. Thus, using stiffness tensor, deformation rate equation can be expressed in another form. Consider

$$\frac{\partial}{\partial t}\int_V T_{kl} dV = \frac{1}{2}\int_S c_{klij}\left(v_i n_j + v_j n_i\right) dS = \int_S c_{klij} v_i n_j dS. \tag{3}$$

In the case of isotropic material c can be written as [17]

$$c_{ijkl} = \lambda \delta_{ij}\delta_{kl} + \mu\left(\delta_{ik}\delta_{jl} + \delta_{il}\delta_{jk}\right), \tag{4}$$

where λ and μ are lame constants.

2.2. Spatial Discretized Form of Two Dimensional EFIT. Consider the Cartesian coordinate $\{x, y, z\}$ and ultrasonic wave which propagates in two dimensional xz-plane. To apply FIT to (1) and (2), squares shown in Figure 1 are used as integral volume V, assuming constant v and T for each volume.

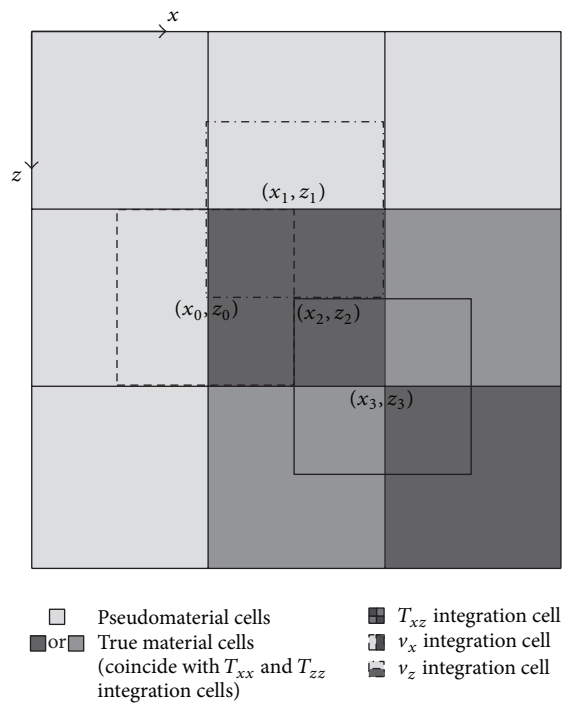

Figure 1: Definition of integration cells for stress and velocity components. The geometry consists of four true material cells and four pseudomaterial cells [12].

The final results for discretized form are

$$\begin{aligned}\frac{\partial v_x(x_0, z_0)}{\partial t} &= \frac{1}{\rho}\left[\frac{T_{xx}(x_0 + (\Delta x/2), z_0) - T_{xx}(x_0 - (\Delta x/2), z_0)}{\Delta x}\right.\\ &\quad + \frac{T_{xz}(x_0, z_0 + (\Delta z/2)) - T_{xz}(x_0, z_0 - (\Delta z/2))}{\Delta z}\\ &\quad \left. + \frac{f_x}{\Delta x \Delta z}\right].\end{aligned} \tag{5}$$

A same manner of integration equation (1) about a v_z integration cell centered at (x_1, z_1) results in

$$\begin{aligned}\frac{\partial v_z(x_1, z_1)}{\partial t} &= \frac{1}{\rho}\left[\frac{T_{xz}(x_1 + (\Delta x/2), z_1) - T_{xz}(x_1 - (\Delta x/2), z_1)}{\Delta x}\right.\\ &\quad + \frac{T_{zz}(x_1, z_1 + (\Delta z/2)) - T_{zz}(x_1, z_1 - (\Delta z/2))}{\Delta z}\\ &\quad \left. + \frac{f_z}{\Delta x \Delta z}\right].\end{aligned} \tag{6}$$

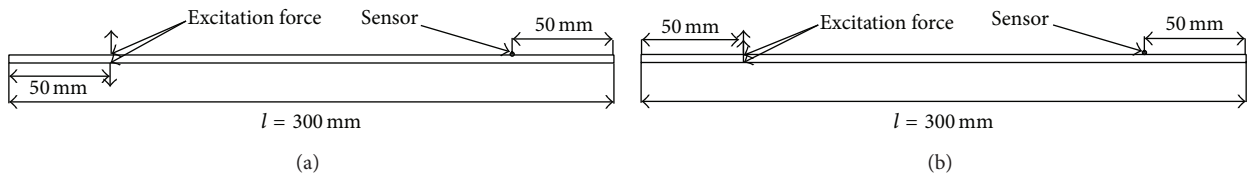

Figure 2: Steel sheet with length $l = 300$ mm and thickness $d = 2$ mm. (a) Excitation pattern for symmetric mode. (b) Excitation pattern for axisymmetric mode.

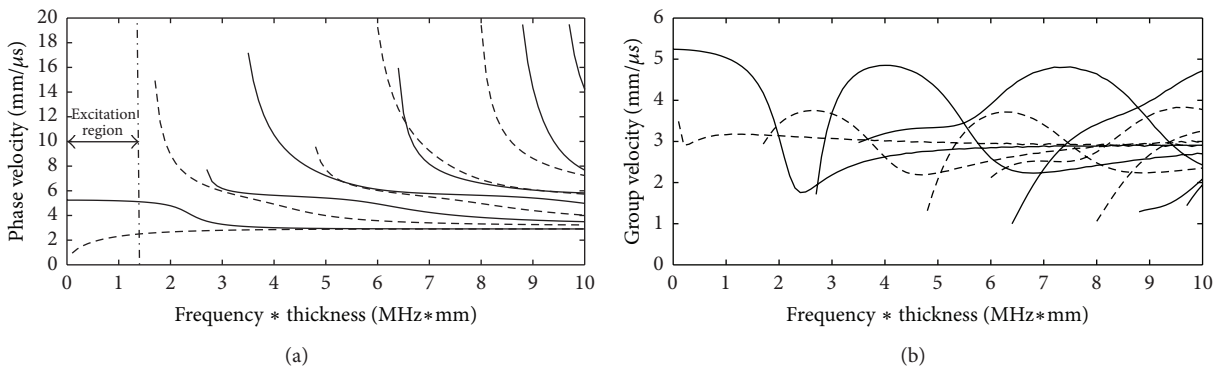

Figure 3: Dispersion diagram for a plate steel (a) phase velocity curve and (b) group velocity curve.

Now, using the normal stress equations, integration of (3) about T_{xx} and T_{zz} centered at (x_2, z_2) yields

$$\begin{aligned}
&\frac{\partial T_{xx}(x_2, z_2)}{\partial t} \\
&= (\lambda + 2\mu)\left[\frac{v_x(x_2 + (\Delta x/2), z_2) - v_x(x_2 - (\Delta x/2).z_2)}{\Delta x}\right] \\
&\quad + \lambda\left[\frac{v_z(x_2, z_2 + (\Delta z/2)) - v_z(x_2, z_2 - (\Delta z/2))}{\Delta z}\right], \\
&\frac{\partial T_{zz}(x_2, z_2)}{\partial t} \\
&= (\lambda + 2\mu)\left[\frac{v_z(x_2, z_2 + (\Delta z/2)) - v_z(x_2, z_2 - (\Delta z/2))}{\Delta z}\right] \\
&\quad + \lambda\left[\frac{v_x(x_2 + (\Delta x/2), z_2) - v_z(x_2 - (\Delta x/2), z_2)}{\Delta x}\right].
\end{aligned} \tag{7}$$

Finally, integration of (3) over T_{xz} integration cell centered at (x_3, z_3) the intersection for material cells results in

$$\begin{aligned}
&\frac{\partial T_{xz}(x_3, z_3)}{\partial t} \\
&= \mu\left[\frac{v_x(x_3, z_3 + (\Delta z/2)) - v_x(x_3, z_3 - (\Delta z/2))}{\Delta z}\right. \\
&\quad \left. + \frac{v_z(x_3 + (\Delta x/2), z_3) - v_z(x_3 - (\Delta x/2), z_3)}{\Delta x}\right].
\end{aligned} \tag{8}$$

As shown in Figure 1, to simplify indexing into stress and velocity arrays of staggered grids when programming the numerics and to keep the same array sizes for all quantities, pseudomaterial cells are used. These cells have the same material properties as the true material they are added to but are not part of physical simulations.

2.3. Time Discretization. Central differences are used to discretize the equations in time domain which results in the velocity and stress components being staggered in time by $\Delta t/2$ [15]. Consider

$$\begin{aligned}
v^n &= v^{n-1} + \Delta t \dot{v}^{n-(1/2)}, \\
T^{n+(1/2)} &= T^{n-(1/2)} + \Delta t \dot{T}^n,
\end{aligned} \tag{9}$$

where Δt is time interval, superscript n is integer number of time step, and dot $\{\cdot\}$ denotes the time differentiation.

Equations (5)–(8) are solved at all points in simulation space and, by use of (9), the simulation proceeds in time in a "leap frogging" manner. A specific stability condition and adequate spatial resolution must be satisfied to guarantee EFIT convergence and accurate answers [15].

3. Propagation of Lamb Wave in a Steel Plate

In this part, the propagation of lamb wave in a steel plate is simulated using 2D-EFIT. The steel plate has the length $l = 300$ mm and the thickness $d = 2$ mm. Table 1 shows material properties used in this paper.

As excitation source, point sources at top and bottom borders of plate are used. Figure 2 shows location of applied loads.

Using excitation patterns shown in Figure 2 and dispersion diagram for steel plate (Figure 3), single mode lamb wave is generated which makes signal interpretation easier.

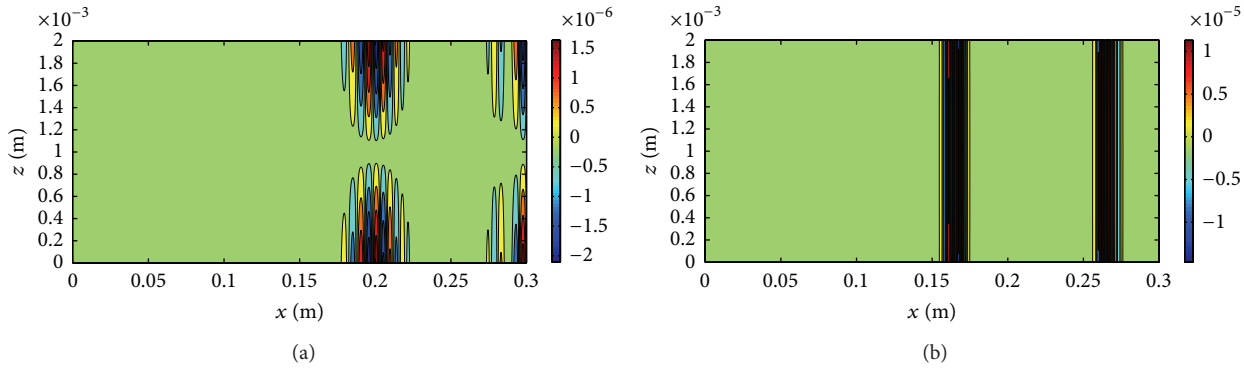

Figure 4: Lamb wave propagation in a steel plate at time $T = 80\,\mu$s. The snapshot represents normal component of particle velocity (v_z): (a) symmetric mode and (b) axisymmetric mode.

Table 1: Material properties used for simulation.

Property	Value
Density	7700 (kg/m^3)
Elastic modulus	195 Gpa
Lame constant λ	96.95 Gpa
Lame constant μ	76.17 Gpa

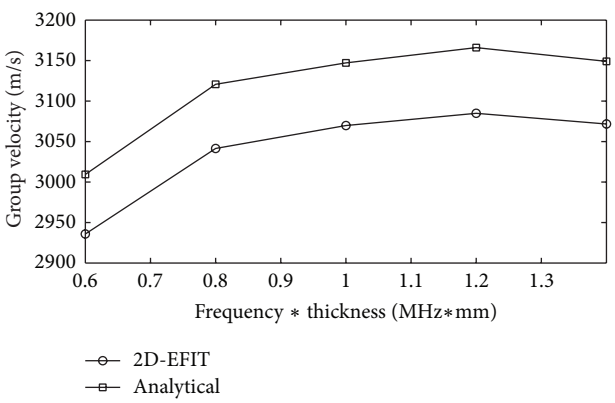

Figure 5: Analytical group velocities comparison with 2D-EFIT results for fundamental axisymmetric mode.

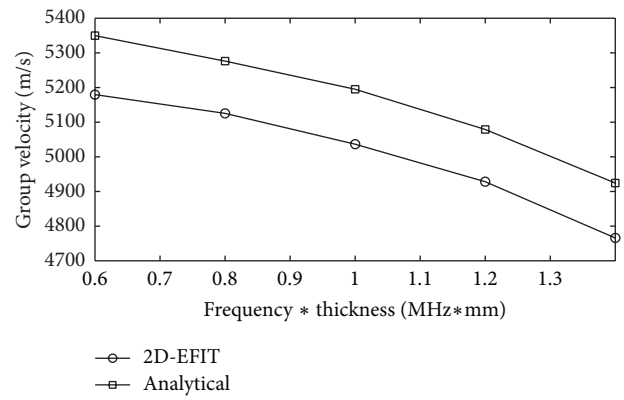

Figure 6: Analytical group velocities comparison with 2D-EFIT results for fundamental symmetric mode.

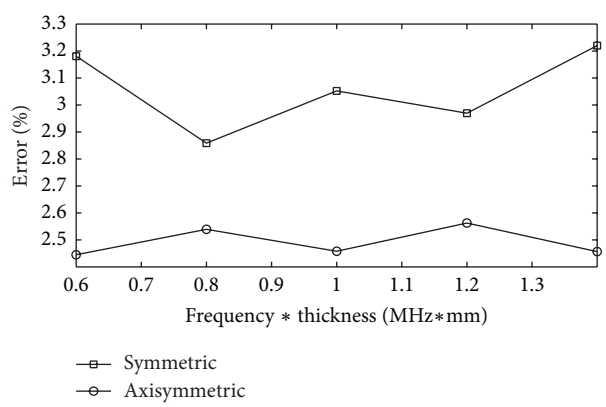

Figure 7: Error comparison for symmetric and axisymmetric modes.

Using 2D-EFIT code developed in MATLAB, propagation of lamb wave in the steel plate is simulated. To guarantee stability and accuracy of results, Δx and Δz are chosen 0.2 mm and Δt is 20 ns. The simulation results using EFIT-tool for symmetric and axisymmetric modes are presented in Figure 4, where the ultrasonic wave field in the plate at time $T = 80\,\mu$s is shown (excitation pulse is a raised cosine with five cycles with center frequency of 500 kHz).

As shown in Figure 4, for the fundamental symmetric mode (S_0), the lamb wave field is symmetric about half plane line and, for the fundamental axisymmetric mode (A_0), normal component of particle velocity v_z has the same value for every particle with same longitudinal position. From dispersion curve, we find that S_0 travels faster than A_0 which is validated by simulation results (see Figure 4).

In order to check EFIT accuracy, group velocities obtained from simulation are compared with analytical results at both symmetric and axisymmetric modes (Figures 5 and 6).

Figures 5–7 show good agreement for simulation results with analytical ones; also Figure 7 shows error dependence

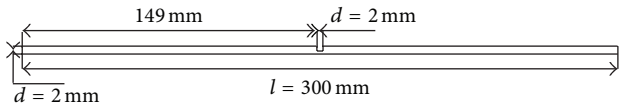

Figure 8: Schematic of model used for studying interaction lamb wave with a defect in a steel plate.

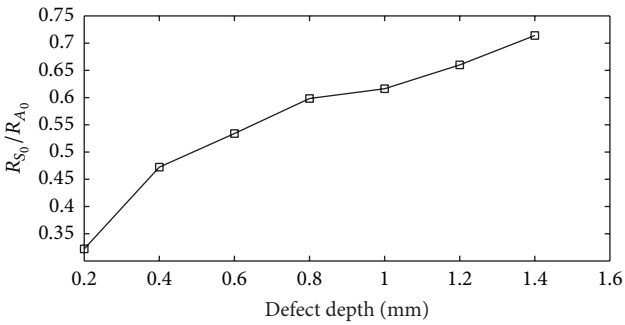

Figure 9: Ratio of reflection coefficients as function of crack depth.

on frequency for axisymmetric mode is less than symmetric mode.

4. Reflection of the Fundamental Symmetric Mode (S_0) from a Defect

In this section, interaction of the S_0 mode with a defected steel plate is analyzed. The results presented here were used for a sizing study of rectangular surface braking defect with different depths and opening length 2 mm on a steel plate (Figure 8).

The same method used in the proceeding section is used to generate single mode with center frequency of 500 kHz. However, as the lamb wave interacts with a defect, the axisymmetric mode will be generated. To study lamb wave interaction with a defect, the ratio of the maximum amplitudes for two modes R_{S_0}/R_{A_0} is then calculated and compared at different depths (Figure 9).

Figure 10 shows the ultrasonic wave field in the defected plate at time $T = 60\,\mu$s; the defect depth is 0.4 mm. As shown in Figure 10, because symmetric modes travel faster than axisymmetric ones, mode separation happens after lamb wave interaction with defect.

5. Conclusion

EFIT was used for studying lamb wave propagation in a steel plate using a program developed in MATLAB environment. Two sets of simulation results were presented in this paper. In the first example, group velocities of lamb wave for different frequencies were obtained using numerical signals and then the results were compared with analytical results; the comparison shows, for both fundamental symmetric and axisymmetric modes, the group velocity values are in good agreement with theoretical ones. In the second example, reflection of S_0 mode from a defect is studied and ratio of

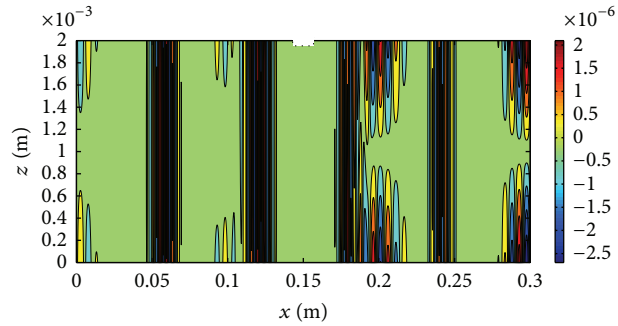

Figure 10: Lamb wave propagation in a steel plate with defect at time $T = 60\,\mu$s. The snapshot represents normal component of particle velocity (v_z (m/s)).

reflection coefficients was obtained as a function of crack depth which shows that as the crack depth increases the ratio R_{S_0}/R_{A_0} increases. Each calculation presented in this paper was done on ordinary PC (Core i5, 2.4 GHz, 4 GB RAM).

Conflict of Interests

The authors declare that there is no conflict of interests regarding the publication of this paper.

References

[1] J. G. Yu, F. E. Ratolojanhary, and J. E. Lebvre, "Guided waves in functionally graded viscoelastic plates," *Journal of Composite Structures*, vol. 93, pp. 2671–2677, 2011.

[2] V. T. Rathod and D. R. Mahapatra, "Ultrasonic lamb wave based monitoring of corrosion type of damage in plate using a circular array of piezoelectric transducer," *NDT & E International*, vol. 44, no. 7, pp. 628–636, 2011.

[3] A. Raghavan and C. E. S. Cesnik, "Review of guided wave structural health monitoring," *Journal of The Shock and Vibration Digest*, vol. 39, pp. 91–113, 2007.

[4] C. M. Yeum, H. Sohn, and J. B. Ihn, "Lamb wave mode decomposition using concentric ring and circular piezoelectric transducers," *Wave Motion*, vol. 48, no. 4, pp. 358–370, 2011.

[5] S. Sorohan, N. Constantin, M. Gavan, and V. Anghel, "Extraction of dispersion curves for waves propa-gating in free complex waveguides by standard finite element codes," *Ultrasonics*, vol. 51, pp. 503–515, 2011.

[6] V. B. Yadav, T. Piralima, V. Raghuram, and N. N. Kishore, "A finite difference simulation of multi-mode lamb waves in aluminium sheet with experimental verification using laser based ultrasonic generation," in *Proceedings of the 12th Asia-Pacific conference on NDT*, Aukland, New Zeland, November 2006.

[7] K. F. Graff, *Wave Motion on Elastic Solids*, Dover Publications, New York, NY, USA, 1991.

[8] T. Hayashi and J. L. Rose, "Guided wave simulation and visualization by a semianalytical finite element method," *Journal of Materials Evaluation*, vol. 61, pp. 75–79, 2003.

[9] D. Gsell, T. Leutenegger, and J. Dual, "Modeling three-dimensional elastic wave propagation in circular cylindrical structures using a finite-difference approach," *Journal of Acoustic Society of America*, vol. 116, no. 6, pp. 3284–3293, 2004.

[10] Z. Xiaoliang and J. L. Rose, "Boundary element modeling for defect characterization potential in a wave guide," *International Journal of Solid and Structures*, vol. 40, pp. 2645–2658, 2003.

[11] C. A. C. Leckey, M. D. Rogge, C. A. Miller, and M. K. Hinders, "Multiple-mode lamb wave scattering simu-lations using 3D elastodynamic finite integration technique," *Journal of Ultrasonics*, vol. 52, pp. 193–207, 2012.

[12] D. C. Calvo, K. E. Rudd, M. Zampolli, W. M. Sanders, and L. D. Bibee, "Simulation of acoustic scattering from an aluminum cylinder near a roughinterface using the elastodynamic finite integration technique," *Wave Motion Journal*, vol. 47, pp. 616–634, 2010.

[13] Y. Cho, D. Hongerholt, and J. L. Rose, "Lamb wave scattering analysis for reflector characterization," *IEEE Transactions on Ultrasonics*, vol. 44, pp. 44–52, 1997.

[14] R. Marklein, "The finite integration technique as a general tool to computeacoustic, electromagnetic, elastodynamic, and coupled wave fields," in *Review of Radio Science: 1999–2002 URSI*, W. Stone, Ed., IEEE Press and John Wiley and Sons, New York, NY, USA, 2002.

[15] F. Schubert, A. Peiffer, B. Kohler, and T. Sanderson, "The elastodynamic finite integration technique for waves in cylindrical geometries," *The Journal of the Acoustical Society of America*, vol. 104, no. 5, pp. 2604–2614, 1998.

[16] F. Schubert and B. Koehler, "Three-dimensional time domain modeling of ultrasonic wave propagation in concrete in explicit consideration of aggregates and porosity," *Journal of Computational Acoustics*, vol. 9, no. 4, pp. 1543–1560, 2001.

[17] K. Takata, K. Nakahata, F. Schubert, and B. Kohler, "Image-based FIT modeling for coupled elastody-namic and acoustic problems," in *Proceedings of AIP Conference*, vol. 1335, pp. 720–727, 2011.

Hindawi Publishing Corporation
Shock and Vibration
Volume 2014, Article ID 718140, 5 pages
http://dx.doi.org/10.1155/2014/718140

Research Article

Experimental Parametric Identification of a Flexible Beam Using Piezoelectric Sensors and Actuators

Sajad Saraygord Afshari, Hadi Nobahari, and Seyed Ali Hosseini Kordkheili

Department of Aerospace Engineering, Sharif University of Technology, Azadi Avenue, P.O. Box 11365-11155, Tehran, Iran

Correspondence should be addressed to Hadi Nobahari; nobahari@sharif.edu

Received 19 October 2012; Accepted 19 November 2012; Published 29 June 2014

Academic Editor: Abdolreza Ohadi

Experimental system identification of a flexible beam based on sweep square excitation is studied. For the purpose of nonparametric identification, an excitation signal is conducted to evaluate the frequency response of the system. The experiment is designed to excite the beam using a piezo actuator, in a way to raise the chance of exciting first three natural modes. In order to find the best linear representation of the real system, two different identification methods are applied. First, autoregressive moving average eXogenous method is employed to identify the transfer function of the beam. Then, the identification is carried out using the subspace identification method to obtain the state space model. A comparison is made between different orders of prediction and the best chosen models of the two identification methods are compared with each other to select the most accurate linear system. Furthermore, as the identified model has to fulfill the controllability and observability conditions, the amenable system is achieved after some order reductions. Two reduction methods called minimum truncation and maximum DC gains matching are utilized to find the most effective reduced order. The outcome of this study will bring in the best linear representation of the beam coupled with piezoelectric sensors/actuators.

1. Introduction

As the need to lightweight systems increases, we will face more problems on behalf of satisfying inertia and size requirements, and vibration can become a major factor in dynamic behavior of designed structures. This vibration is unwanted and active control methods are required to adapt the dynamic response. Many of the devices used for passive and active structural vibration attenuation are large, heavy, and inappropriate for desired applications. Considering new advances in materials science, which have led to a range of functional materials, we will be able to reach our goals in designing modern configurations with no constraint in dynamical behavior. These structures have been labeled "smart structures" and are commonly used to deal with the vibration control problem in lightweight flexible structures such as flexible beams [1].

Successful vibration control is known as minimizing the possibility of structural failure. In most previous works, various approaches have been utilized to find the theoretical models for the structures embedded with smart materials, such as piezoelectric sensors/actuators. Most of the models were usually limited to either analytical models with ignoring inertia and stiffness of the piezoelectric patches, or finite element models with approximate simulation of the actual identity and properties of the system [1].

Analytical and numerical approaches in modeling dynamical systems coupled with piezo patches are usually time consuming and their applications for accurate control are sometimes defeated by factors such as the assumption of perfect bonding at the interface between the structure and transducers. Besides, these modeling approaches are occasionally impossible for highly complex structures. Considering these limitations, system identification can be introduced as a viable approach in modeling structural systems, such as flexible beams.

In this area, the system identification modeling based on autoregressive moving average eXogenous (ARMAX) and prediction error method (PEM) techniques was successfully developed. The major effort of this study was aimed at establishing a perfect structure model between the system input and output using a parametric system identification

approach based on nonparametric results. For this purpose, we will apply different methods of linear estimation and the best fitting frequency response will be represented for a flexible beam.

The organization of this paper is as follows. In Section 2, the experimental setup, developed for identification of the fixable beam, is introduced. Parametric and nonparametric system identification and the concept of model reduction are expressed in Section 3. Section 4 is devoted to the experimental results. Finally, a conclusion is made in Section 5.

2. Experimental Setup

In order to find an accurate model of the system, a cantilevered aluminum beam ($E = 70\,\text{GPa}$, $\nu = 0.3$, $\rho = 2700\,\text{Kg/m}^3$) is developed. Figure 1 shows the experimental setup of the beam in a cantilevered configuration. Two piezoceramic patches are attached on both sides of the beam for the purpose of strain sensing and applying the excitation force to the beam. The aluminum and piezoelectric patches thicknesses are 0.5 mm and 0.6 mm, respectively. Schematic diagram of the experimental setup is also illustrated in Figure 2.

The beam damping coefficient is very low and it will go under substantial vibrations when excited. Both piezoelectric patches were surface bonded at the cantilever end since this is the best position for sensor and actuator to detect and excite desired modes [2]. The piezo actuator is excited using a PIEZO SYSTEM INC. 20X amplifier, and an ADVANTECH USB-4716 device plays a role as an analog/digital interface.

3. System Identification

System identification can be defined as developing a mathematical model for an existing dynamic system and it is widely used in modelling dynamic systems. Capturing the behaviour of a system in a full and accurate model, we will be able to use it to simulate the time response of the system, to develop controller in a fast and precise way using the simulated system behaviour, and so forth [2].

3.1. Nonparametric System Identification. In order to reach an inclusive model of the system, frequency response function (FRF) data is severely required. Hence, an experiment based on sweep square excitation method is performed and the FRF is obtained from a zero initial condition. The input voltage is applied to the piezoceramic actuator of the uncontrolled flexible beam system. The voltage is sensed by the piezo sensor on the other side of the beam [2].

The evaluation test is performed to excite the beam with a square wave voltage, the frequency of which varies from 0.5 to 40 Hz to have the chance of exciting the first three modes. Time of the experiment is 60 s with a sampling frequency of 200 Hz and a digital low pass filter set at 100 Hz. The FRF is calculated using MATLAB signal processing tools.

Figure 1: Experiment setup of piezo-laminated at smart materials Lab.

3.2. Parametric System Identification. To design a controller for vibration suppression of the first three modes, it is imperative to have a parametric state space model of the system. A proper parametric model can be identified by suitably minimizing the error between the frequency response of predicted and real systems.

In this study, two different system identification methods have been compared to find the most useful and accurate parametric model of the system. First, the well-known method, called ARMAX, is employed to identify the transfer function of the beam structure, equipped with two piezoceramic patches. Then, the identification is carried out using the available subspace identification method of MATLAB platform, namely, `pem32`, and the state-space model is obtained.

3.3. ARMAX System Identification. Autoregressive moving average models calculate the current system output as a function of past inputs and outputs and ARMAX is an iterative search algorithm which minimizes a quadratic prediction error criterion. The iterations are terminated either when max iteration limit is reached, or when the expected improvement is less than predefined tolerance, or when a lower value of the criterion cannot be found. The general linear form of the ARMAX model is [3]

$$\begin{aligned} y_t + a_2 y_{t-1} + \cdots + a_{na} y_{t-na} \\ = b_1 u_{t-1} + b_2 u_{t-2} + \cdots + b_{nb} u_{t-nb}, \end{aligned} \tag{1}$$

or in discrete linear transfer function form as follows:

$$\frac{y_t}{u_t} = \frac{b_1 z^{-1} + b_2 z^{-2} + \cdots + b_n z^{-nb}}{1 + a_1 z^{-1} + a_2 z^{-2} + \cdots + a_{na} z^{-na}}. \tag{2}$$

The first practical step in realizing an ARMAX model is to select the degrees of denominator and numerator (na and nb). ARMAX identifies the parameters ai and bi using system input-output data. These data should, if possible, be densely populated in the input space. This will help to reduce the interpolation error when calculating the output for unused data.

3.4. Subspace System Identification. A linear system can be characterized in the state space advanced form as

$$\begin{aligned} x(t+1) &= Ax(t) + Bu(t) + Ke(t), \\ y(t) &= Cx(t) + Du(t) + e(t), \end{aligned} \tag{3}$$

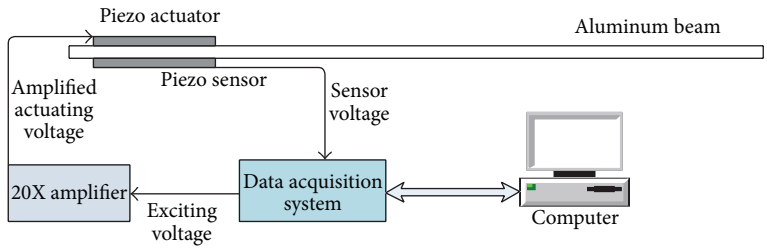

Figure 2: Schematic diagram of the Experiment.

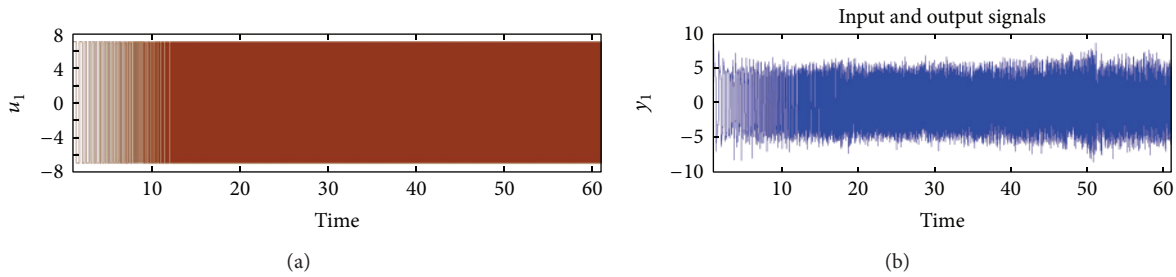

Figure 3: (a) Excitation signal applied to the system; (b) system experimental time response.

where $e(t)$ is the output that cannot be predicted from the past data, $x(t)$ is the state vector, $y(t)$ is the output, $u(t)$ is the input, and K is the Kalman gain [4].

The subspace method can be used to estimate A, B, C, D, and K matrices. Assuming that $x(t)$, $y(t)$, and $u(t)$ are known, (3) becomes a linear regression. This will enable us to estimate the matrices C and D by the least-squares method and will lead us to determine $e(t)$. Then, $e(t)$ can be treated as a known signal and this will lead us to determine A, B, and K using the least-squares method. The Kalman gain K is computed using Riccati equation. In the above method, it is assumed that $x(t)$ is known; however, it needs to be determined. The states $x(t)$ can be formed as a linear combination of the k step ahead predicted outputs. The above model, derived from the subspace method is then used as the base model for further refining by the prediction error method (PEM). Substantial details for PEM can be found in the MATLAB system identification manual [5]. In this paper, we consider a state space realization that does not model the noise properties; that is, $K = 0$.

Here in this study, after applying ARMAX method, MATLAB `pem32` tool is utilized to predict the system linear model with PEM method. Comparing the consequences of different prediction orders results in the most effective degrees of freedom for linear estimation of the system using prediction error method and subspace system identification.

3.5. Model Reduction. Finding the most appropriate model of the system is not always enough. Furthermore, the identified model has to fulfill the controllability and observability conditions. Accordingly, after finding the most suitable parametric system, a controllable and observable system can be achieved utilizing some order reduction methods. The order reduction should be performed in a way which results in the slightest deviation from the nonparametric model [6].

Here, the first step after choosing the appropriate linear model is to find the minimal realization of the estimated system. For this purpose, the MATLAB function `balreal`, is employed. After finding the minimal realization, we may apply modal reduction techniques to reach both controllable and observable system. Again, this objective can be achieved using MATLAB function `modred`. In both mentioned order reduction functions, two reduction methods, called minimum truncation and maximum DC gains matching, are utilized and the results are compared to find the most helpful reduced order model.

4. Result and Discussion

System identification procedures utilized to model the first three modes of vibration in a highly-flexible smart beam. The modes successfully modeled using ARMAX and PEM system identification methods and both obtained models were shown to have sufficient accuracy to design a controller. For each method, different estimation orders have tried to find the best fit model to the original system. Results demonstrated that an order 20 ARMAX and order 25 PEM estimation are applicable in representing desired dynamics of such a cantilevered system. The results show that increasing the system order will not significantly improve the frequency response. Here the models were extracted from the experimental time response of the system under a sweep square excitation as it can be seen in Figure 3.

Finally, a comparison is made between different orders of prediction and the best chosen models of the two identification methods are compared with each other to select the most

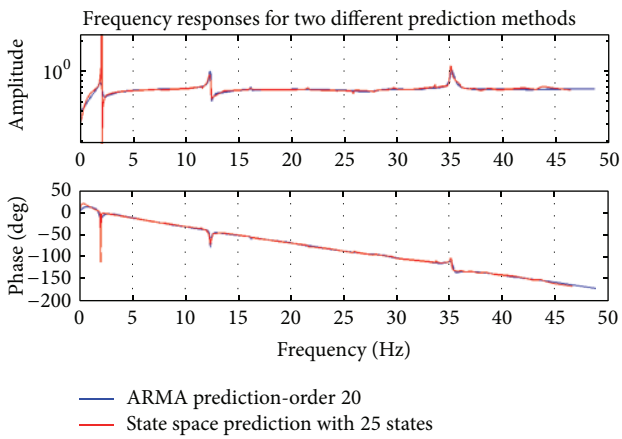

Figure 4: Frequency responses of estimated parametric models.

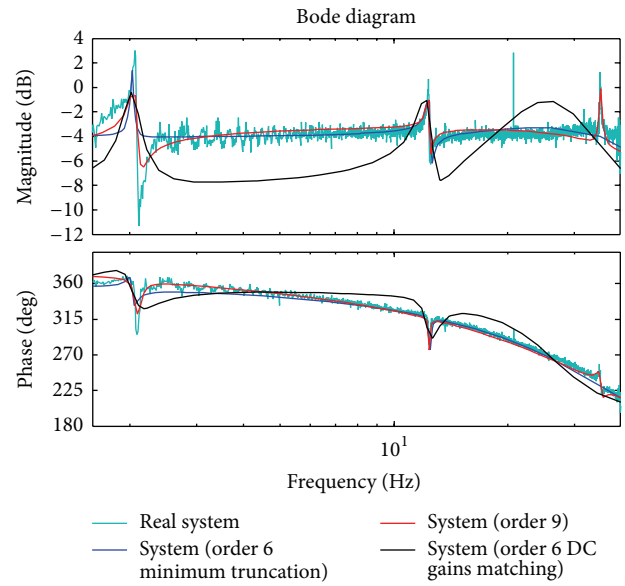

Figure 5: Comparison of frequency responses for reduced order models.

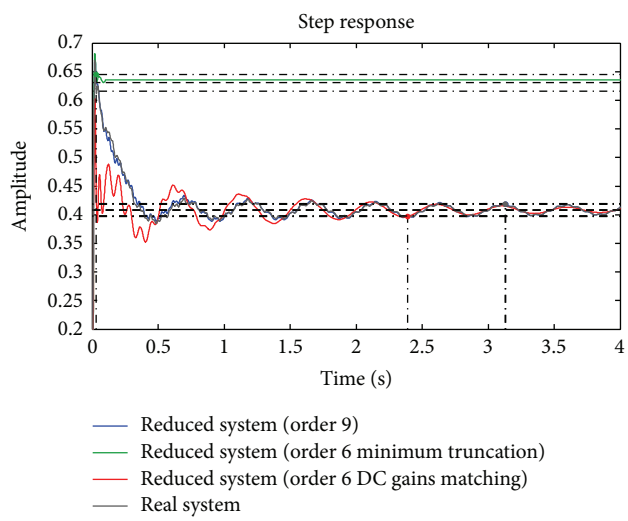

Figure 6: Comparison of step response for different reduced order systems.

accurate representation of the system. The model of order 25, obtained using `pem32` method, is finally proposed as it gives a more precise model especially in the first mode frequency. Figure 4 illustrates a comparison between the ARMAX and PEM in their best estimating performance.

Choosing the model of order 25 in state space representation, the observability and controllability of the estimated model are checked, and as it is expected, the model could not satisfy the desired conditions. So MATLAB `balreal` and `modred` were utilized consequently in order to reduce the model. Minimal realization of the system which does not affect the frequency response characteristics is obtained by an order 9 system. But, the controllability and observability matrices will not be fully ranked. So, implementing `modred`, we found a controllable and observable model of order 6 with minimum deviation from the original one.

As it was stated in the previous section, we may use two different methods for reducing the order of system which are matching the DC gains and finding the reduced system using minimum truncation in frequency response. We applied both methods and the results can be seen in Figure 5. In this figure, it can be seen that the parametric system of order 9 matches well the nonparametric model of the original system in its frequency response and it is a good choice for extracting the transfer function. The reduced system of order 6 with minimum truncation method models the first 2 natural frequencies of the system with an acceptable adaptation, although its performance around natural frequencies is not appropriate enough and it cannot model the antiresonance frequencies as well.

The other method, DC gains matching, performs better in the modal frequencies and it is more desirable in active control problems [7]. Finally, step response of the nonparametric identified system is compared with the step responses of different linear models (Figure 6). It can be seen from this figure that the order 6 system using "DC gains matching" method performs better in its time response and it will match the real system after 2 seconds. It is also noticeable that the system of order 9 is very similar to the real system in its time response behaviour.

5. Conclusion

Problem of identifying a flexible beam coupled with piezoceramic patches is studied in this paper. Parametric system identification procedures are used to obtain a suitable model of the system from its input-output measurement data. Through the comparison of measured and model-based frequency responses, a good representation of the structural dynamics by the identified model was demonstrated and a subspace estimation of order 25 using `pem32` was presented as the most effective linear estimation for this system. Finally, by implementing some model reduction methods, an observable and controllable model was achieved in a way, in

which the system experiences the slightest deviation from the original system. The final outcome of the process provides the system frequency behaviour which can be adopted for different control applications.

Conflict of Interests

The authors declare that there is no conflict of interests regarding the publication of this paper.

Acknowledgment

The experiments were conducted at Mechanics of Smart Materials (MSM) Laboratory, Aerospace Engineering Department, Sharif University of Technology.

References

[1] W. J. Manning, A. R. Plummer, and M. C. Levesley, "Vibration control of a flexible beam with integrated actuators and sensors," *Smart Materials and Structures*, vol. 9, no. 6, pp. 932–939, 2000.

[2] V. Sethi and G. Song, "Multimodal vibration control of a flexible structure using piezoceramic sensor and actuator," *Journal of Intelligent Material Systems and Structures*, vol. 19, no. 5, pp. 573–582, 2008.

[3] X. Bu, L. Ye, Z. Su, and C. Wang, "Active control of a flexible smart beam using a system identification technique based on ARMAX," *Smart Materials and Structures*, vol. 12, no. 5, pp. 845–850, 2003.

[4] V. Sethi and G. Song, "Optimal vibration control of a model frame structure using piezoceramic sensors and actuators," *Journal of Vibration and Control*, vol. 11, no. 5, pp. 671–684, 2005.

[5] http://www.mathworks.com/.

[6] Y. Xie, T. Zhao, and G. Cai, "Model reduction and active control for a flexible plate," *Acta Mechanica Solida Sinica*, vol. 24, no. 5, pp. 467–476, 2011.

[7] X.-J. Dong, G. Meng, and J.-C. Peng, "Vibration control of piezoelectric smart structures based on system identification technique: numerical simulation and experimental study," *Journal of Sound and Vibration*, vol. 297, no. 3–5, pp. 680–693, 2006.

Hindawi Publishing Corporation
Shock and Vibration
Volume 2014, Article ID 530131, 7 pages
http://dx.doi.org/10.1155/2014/530131

Research Article

Analytical Solution for the Sound Radiation Field of a Viscoelastically Supported Beam Traversed by a Moving Load

Rezgar Shakeri and Davood Younesian

Center of Excellence in Railway Transportation, School of Railway Engineering, Iran University of Science and Technology, Tehran 16846-13114, Iran

Correspondence should be addressed to Davood Younesian; younesian@iust.ac.ir

Received 20 October 2012; Accepted 19 November 2012; Published 23 June 2014

Academic Editor: Abdolreza Ohadi

Sound radiation from a beam resting on a viscoelastic foundation is analytically studied when it is subjected to a moving load. The topic could cover a range of applications such as submerged floating tunnels, buried pipelines, and railway tracks. Galerkin's method is employed to obtain the transverse vibration of the beam. Based on the Rayleigh integral approach, acoustic pressure distribution around the beam is obtained in the time domain. In the second part of this paper, corresponding displacement and acoustic pressure are obtained by the use of the Rayleigh-Ritz approach in conjunction with the Laplace transform method and by the use of the Fourier transform, respectively. Durbin's numerical Laplace transform inversion scheme is eventually employed to obtain dynamic responses. A parametric study is then carried out and influences of the design parameters as well as the loading conditions on the acoustic pressure field are investigated.

1. Introduction

The investigation of the dynamic response of beams resting on viscoelastic foundation is a very interesting problem, with applications in various fields of engineering and technology. In particular, acoustic radiation can be found in a different array of practical applications such as submerged floating tunnels, railway tracks, and civil structures. Numerical, analytical, and experimental studies have been performed in the past decades to study the dynamic analysis of soil-structure interaction problem. Beam on elastic foundation has been studied by several authors [1–4]. Kenney [5] studied the steady-state deformation when the point load is moving with constant speed. Kargarnovin et al. [6–8] and Muscolino and Palmeri [9] investigated the response of beam on viscoelastic foundation under moving loads. Andersen et al. [10], Weitsman [11], Choros and Adams [12], and Lin and Adams [13] investigated the response of Euler-Bernoulli beams on tensionless Winkler foundations. The response of embedded railway track using the Winkler foundation model was studied by Shamalta and Metrikine [14]. Steele [15] and Chen and Huang [16, 17] investigated the response of Timoshenko beam on Winkler foundation for a variety of beam, foundation, and loading conditions. Yang and Ge [18] and Senalp et al. [19] investigated the dynamic behavior of Euler-Bernoulli beam resting on viscoelastic foundation subjected to moving load by using the mode decomposition method together with the precise time integration method (MDPIM). Vlasov and Leont'ev [20] showed that the mechanical behavior of an elastic continuum can be quite accurately simulated using springs with shear interactions between them. The tensile resistance is generated in the ground due to shear strain of the soil. Basu and Kameswara Rao [21] studied the steady-state response of an infinite beam resting on a viscoelastic foundation, modeled using springs with shear interactions and subjected to a concentrated moving load with a constant velocity. In this paper, Galerkin's method is proposed to investigate the dynamic response of Euler-Bernoulli beam resting on viscoelastic foundation and shear stiffness of soil is considered. Acoustic radiation is examined by using appropriate 2D images of the sound field for selected foundation parameters. This paper is an invited article selected from the ISAV2012 conference proceedings.

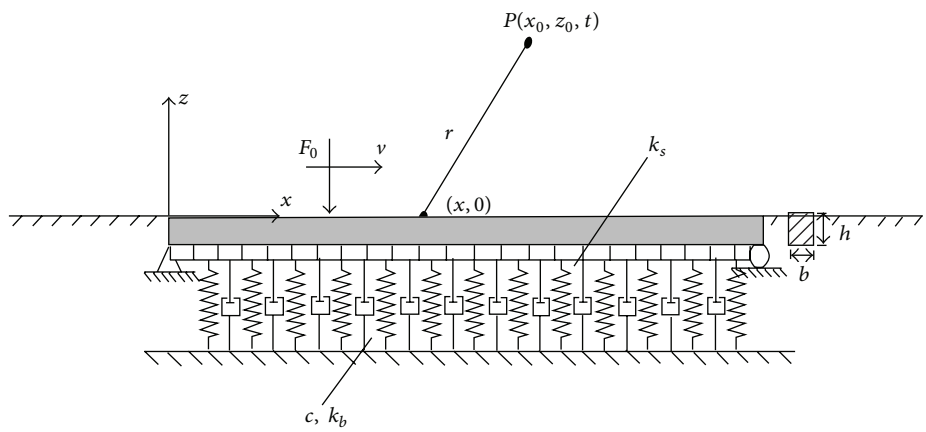

Figure 1: Beam on foundation under moving load.

2. Formulation

2.1. Analytical Method. Consider a simply supported uniform beam of length L, mass per unit length ρA, and bending rigidity EI, resting on viscoelastic foundation, indicated by a bending layer coefficient k_b, a shear layer coefficient k_s, and a viscous coefficient c subjected to a moving load with constant speed v along the beam as shown in Figure 1. The equation of motion for the transverse vibration of the beam is given by [21]

$$EI\frac{\partial^4 w}{\partial x^4} - k_s\frac{\partial^2 w}{\partial x^2} + k_b w + c\frac{\partial w}{\partial t} + \rho A\frac{\partial^2 w}{\partial t^2} = -F_0\delta(x - vt), \tag{1}$$

where w is transverse deflection of the beam and F_0 is applied moving concentrated load. The displacement of the beam is expanded using the eigenfunction of the uniform beam as [22]

$$W_n(x) = \sqrt{\frac{2}{\rho AL}}\sin\frac{n\pi}{L}x,$$
$$w_n = \sqrt{\frac{EI}{\rho A}\left(\frac{n^4\pi^4}{L^4} + \frac{k_s n^2\pi^2}{EIL^2} + \frac{k_b}{EI}\right)}, \tag{2}$$
$$n = 1, 2, \ldots,$$

where ω_n is the natural frequency of the nth mode and $W_n(x)$ is the eigenfunction. The orthogonality condition is

$$\int_0^L \rho A W_i(x) W_j(x)\, dx = \delta_{ij}, \tag{3}$$

where δ_{ij} is Kronecker's delta. The transverse displacement can be expanded as follows:

$$w(x,t) = \sum_{n=1}^{\infty} q_n(t) W_n(x), \tag{4}$$

where $q_n(t)$ is the modal coordinate that must be determined by solving an ordinary differential equation. By direct substitution of expansion (4) into (1) and making use of the general orthogonality relation (3) between the distinct normal modes and the fact that the normal modes, $W_n(x)$, must satisfy the classical relation $EI(d^4W_n(x)/dx^4) - k_s(d^2W_n(x)/dx^2) + k_bW_n(x) = \rho A\omega_n^2 W_n(x)$, (1) can be reduced to

$$\frac{d^2 q_n(t)}{dt^2} + \frac{c}{\rho A}\frac{dq_n(t)}{dt} + \omega_n^2 q_n(t) = Q_n(t), \tag{5}$$

where $Q_n(t) = -\int_0^L W_n(x)F_0\delta(x - vt)dx = -F_0W_n(vt)$. The solution of (5) with the zero initial condition can be expressed as

$$q_n(t) = \int_0^t Q_n(t-\tau) \times \frac{2\exp(-c\tau/2\rho A)\sinh\left(0.5\tau\sqrt{(c/\rho A)^2 - 4\omega_n^2}\right)}{\sqrt{(c/\rho A)^2 - 4\omega_n^2}}d\tau. \tag{6}$$

2.2. Rayleigh-Ritz Method. The Rayleigh-Ritz method is based on an energy or variational principle, such as those provided by the principles of virtual work or their variants, which account for the natural boundary conditions as a part of the principle. The total strain and kinetic energy and the work done by the nonconservative forces are given by [22]

$$U = \frac{1}{2}\int_0^L \left(EI\left(\frac{\partial^2 w}{\partial x^2}\right)^2 + k_b w^2\right)dx,$$
$$T = \frac{1}{2}\int_0^L \rho A\left(\frac{\partial w}{\partial t}\right)^2 dx,$$
$$V = -\int_0^L w(x,t)F_0\delta(x - vt)\,dx - \int_0^L c\frac{\partial w}{\partial t}w dx - \frac{1}{2}\int_0^L k_s\left(\frac{\partial w}{\partial x}\right)^2 dx. \tag{7}$$

Substituting for U, T, and V from (7) in Hamilton's principle, we obtain

$$\begin{aligned} 0 &= \delta \int_0^t (U - T - V)\, dt \\ &= \int_0^t \left\{ \int_0^L \left[EI \frac{\partial^4 w}{\partial x^4} + k_b w + \rho A \frac{\partial^2 w}{\partial t^2} + c \frac{\partial w}{\partial t} \right.\right. \\ &\qquad \left.\left. - k_s \frac{\partial^2 w}{\partial x^2} + F_0 \delta (x - vt) \right] \delta w\, dx \right\} dt. \end{aligned} \tag{8}$$

In the Ritz method, a dependent unknown (e.g., the displacement) $w(x,t)$ is approximated by a finite linear combination as the form [23]

$$w(x,t) = \sum_{n=1}^{N} c_n(t)\, \varphi_n(x) + \varphi_0, \tag{9}$$

where $c_n(t)$ are time-dependent parameters to be determined for all times $t > 0$ and $\varphi_n(x)$ are called the approximation functions. Since the specified geometric boundary condition is homogeneous, we have $\varphi_0 = 0$. The approximation functions $\varphi_n(x)$ must satisfy the simple support's condition. Direct substituting of (9) into (8) and equating coefficients of δc_m to zero may advantageously be put in matrix form as

$$\begin{aligned} &\begin{bmatrix} M_{11} & \cdots & M_{1N} \\ \vdots & \ddots & \vdots \\ M_{N1} & \cdots & M_{NN} \end{bmatrix} \begin{bmatrix} c_1'' \\ \vdots \\ c_N'' \end{bmatrix} + \begin{bmatrix} C_{11} & \cdots & C_{1N} \\ \vdots & \ddots & \vdots \\ C_{N1} & \cdots & C_{NN} \end{bmatrix} \begin{bmatrix} c_1' \\ \vdots \\ c_N' \end{bmatrix} \\ &+ \begin{bmatrix} K_{11} & \cdots & K_{1N} \\ \vdots & \ddots & \vdots \\ K_{N1} & \cdots & K_{NN} \end{bmatrix} \begin{bmatrix} c_1 \\ \vdots \\ c_N \end{bmatrix} = \begin{bmatrix} Q_1 \\ \vdots \\ Q_N \end{bmatrix}, \end{aligned} \tag{10}$$

where

$$\begin{aligned} c_n'' &= \frac{d^2 c_n}{dt^2}, \qquad c_n' = \frac{dc_n}{dt}, \\ M_{nm} &= \int_0^L \rho A \varphi_m(x)\, \varphi_n(x)\, dx, \\ C_{nm} &= \int_0^L c \varphi_m(x)\, \varphi_n(x)\, dx, \\ K_{nm} &= \int_0^L \left(EI \frac{d^4 \varphi_n(x)}{dx^4} - k_s \frac{d^2 \varphi_n(x)}{dx^2} + k_b \varphi_n(x) \right) \\ &\quad \times \varphi_m(x)\, dx, \\ Q_m(t) &= -\varphi_m(vt). \end{aligned} \tag{11}$$

By taking Laplace transform of (10), one obtains

$$R(s)\, C(s) = Q(s), \tag{12}$$

where $C(s)$ is the unknown coefficients vector and $Q(s)$ is the load vector which are given as

$$\begin{aligned} C(s) &= \left[\bar{c}_1(s), \bar{c}_2(s), \ldots, \bar{c}_N(s) \right]^T, \\ Q(s) &= \left[-\bar{\varphi}_1(s), -\bar{\varphi}_2(s), \ldots, -\bar{\varphi}_N(s) \right]^T. \end{aligned} \tag{13}$$

And the coefficient matrix $R(s)$ is rewritten as

$$R(s) = \begin{bmatrix} s^2 M_{11} + sC_{11} + K_{11} & \cdots & s^2 M_{1N} + sC_{1N} + K_{1N} \\ \vdots & \ddots & \vdots \\ s^2 M_{N1} + sC_{N1} + K_{N1} & \cdots & s^2 M_{NN} + sC_{NN} + K_{NN} \end{bmatrix}. \tag{14}$$

The unknown coefficient can readily be determined from

$$C(s) = R^{-1}(s)\, Q(s). \tag{15}$$

In the current work, Durbin's approach [24] for numerical inversion of the Laplace transforms which involves the discretized form of the complex Laplace inversion formula $\Lambda(t) = (1/2\pi j) \int_{\sigma - j\infty}^{\sigma + j\infty} \overline{\Lambda}(s) e^{st} ds$, where $j = \sqrt{-1}$ and σ is an arbitrary real number greater than all the real parts of the singularities of $\overline{\Lambda}(s)$ and $\overline{\Lambda}(s)$ can be $\overline{w}(x,s)$ or $\overline{p}(x,z,s)$ in the interval $[0, 2T_0]$, shall be adopted. Accordingly, one could readily employ expansion [25]

$$\begin{aligned} \Lambda(t) &= \frac{2 \exp(\sigma t)}{T_0} \\ &\quad \times \left\{ \frac{1}{2} \operatorname{Re}\left(\overline{\Lambda}(\sigma) \right) \right. \\ &\quad + \sum_{l=1}^{M} \left[\operatorname{Re}\left(\overline{\Lambda}\left(\sigma + j \frac{2\pi l}{T_0} \right) \right) \cos\left(\frac{2\pi l}{T_0} t \right) \right. \\ &\quad \left.\left. - \operatorname{Im}\left(\overline{\Lambda}\left(\sigma + j \frac{2\pi l}{T_0} \right) \right) \sin\left(\frac{2\pi l}{T_0} t \right) \right] \right\}, \end{aligned} \tag{16}$$

where M is the truncation constant and the suggested value of "σT_0" is between 5 and 10 for sufficient accuracy [24].

2.3. Acoustic Radiation. The acoustic pressure radiated from a vibration beam in an infinite baffle can be obtained by evaluating the Rayleigh surface integral where each elemental area on the beam surface is regarded as a simple point source of an outgoing wave and its contribution is added with an appropriate time delay. Referring to Figure 1, the acoustic pressure $P(x_0, z_0, t)$ at the observation point p with Cartesian coordinates (x_0, z_0) at time t caused by the vibration of the beam is given by [26]

$$P(x_0, z_0, t) = \frac{\rho_0}{2\pi} \int_0^b \int_0^L \ddot{w}\left(x, t - \frac{r}{c_0} \right) \frac{1}{r} dx\, dy, \tag{17}$$

where ρ_0 and c_0 are the mass density and wave velocity of the acoustic medium, respectively, $\ddot{w}(x,t)$ is the acceleration time history of the beam obtained previously, and $r = \sqrt{(x - x_0)^2 + z_0^2}$ is the distance between the observation point p and the point at $(x, 0)$ on the beam surface.

Table 1: Properties of the UIC60 rail, foundation, load, and acoustic medium [8].

Item	Notation	Value
Young's modulus (steel)	E	210 GPa
Mass density of beam	ρ	7850 kg/m^3
Cross-sectional area	A	7.69×10^{-3} m^2
Second moment of area	I	30.55×10^{-6} m^4
Bending stiffness	k_b	202 MN/m^2
Viscous damping	c	141 kN s/m^2
Load	F_0	65 kN
Mass density of acoustic medium (air)	ρ_0	1.2 kg/m^3
Wave velocity	c_0	343 m/s

In addition, the pressure distribution in the acoustic fluid domain can be obtained from the solution of the wave equation as follows:

$$\left(\frac{\partial^2}{\partial x^2} + \frac{\partial^2}{\partial z^2}\right) p(x,z,t) = \frac{1}{c_0^2}\frac{\partial^2 p}{\partial t^2}. \quad (18)$$

In frequency domain, (18) reduces to $((\partial^2/\partial x^2) + (\partial^2/\partial z^2) + (\omega^2/c_0^2))p(x,z,\omega) = 0$, and referring to Figure 1, the Rayleigh integral in the frequency domain [27] is $P(x_0,z_0,\omega) = (\rho_0/2\pi)\int_0^b\int_0^L \ddot{w}\ (x,\omega)(\exp(ikr)/r)dx\,dy$, where $k = \omega/c_0$ and $\ddot{w}\ (x,\omega)$ is the acceleration of the beam in the frequency domain. Taking Laplace transform of (18) leads to $((\partial^2/\partial x^2)+(\partial^2/\partial z^2) + (-s^2/c_0^2))\overline{p}(x,z,s) = 0$, and then, the Rayleigh integral in the Laplace domain is

$$\overline{P}(x_0,z_0,s) = \frac{s^2\rho_0}{2\pi}\int_0^b\int_0^L \overline{w}(x,s)\frac{\exp(i\overline{k}r)}{r}dx\,dy, \quad (19)$$

where $\overline{k} = js/c_0$ and $\overline{w}(x,s) = \sum_{n=0}^{\infty} q_n(s)W_n(x)$ is the displacement of the beam in the Laplace domain where $W_n(x)$ is given by (2) and $q_n(s)$ is obtained from (5). Finally, the acoustic pressure can be calculated by (16). In the following section, the comparison between these two methods is considered.

3. Numerical Results

A parametric study is directed in this section to investigate the effects of different parameters on the acoustic pressure field radiated from the vibrating beam series of numerical simulations that have been carried out and some of the numerical results are presented as a few samples in this section. The physical and geometrical properties of the beam and acoustic medium are listed in Table 1 [8].

Figure 2 exhibits the midspan displacement of the beam with respect to the time. Because of the foundation under the beam, the vibration around the maximum deflection is zero. The maximum deflection will occur at the location of the load. Furthermore, excellent agreement of the present result and [19] for load velocity $v = 50$ m/s is obtained. Figure 3 displays the comparison between the results of the analytical and Rayleigh-Ritz methods for selected load velocity $v = 55$ m/s and for a beam extended 15 m in longitudinal direction. The results show a good agreement between these two methods. Taking shear layer coefficient into consideration, the maximum deflection of the beam will decrease when the shear layer coefficient is increased due to increment of natural frequencies of the beam.

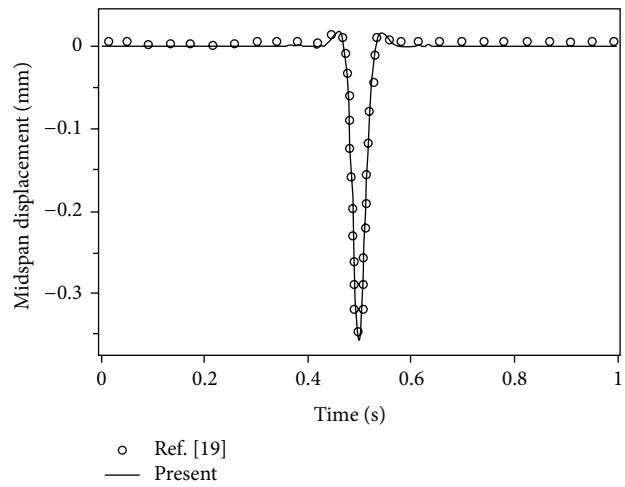

Figure 2: Comparison of the displacement response with [19].

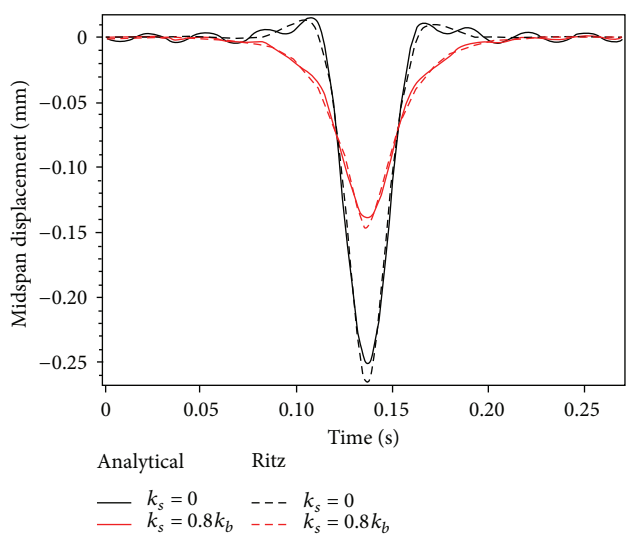

Figure 3: Comparison of analytical and Rayleigh-Ritz methods.

Figure 4 shows the acoustic pressure response at two selected points and for $k_s = 0$, $k_s = 0.8k_b$ when the load passes through the beam. The acoustic pressure decreases as the viscoelastic and bending stiffness and height of selected points increase. Also for $k_s = 0.8k_b$, an interesting reduction of the first radiated pressure wave from the vibrating beam is seen at $t_0 = z_0/c_0 = (0.014\ \&\ 0.058)$ sec.

Figure 5 displays the acoustic pressure response and comparison between two methods for $t \geq r/c_0$. The results show good agreement between two equations. Equation (17) exhibits instabilities for time interval of $0 \leq t < r/c_0$;

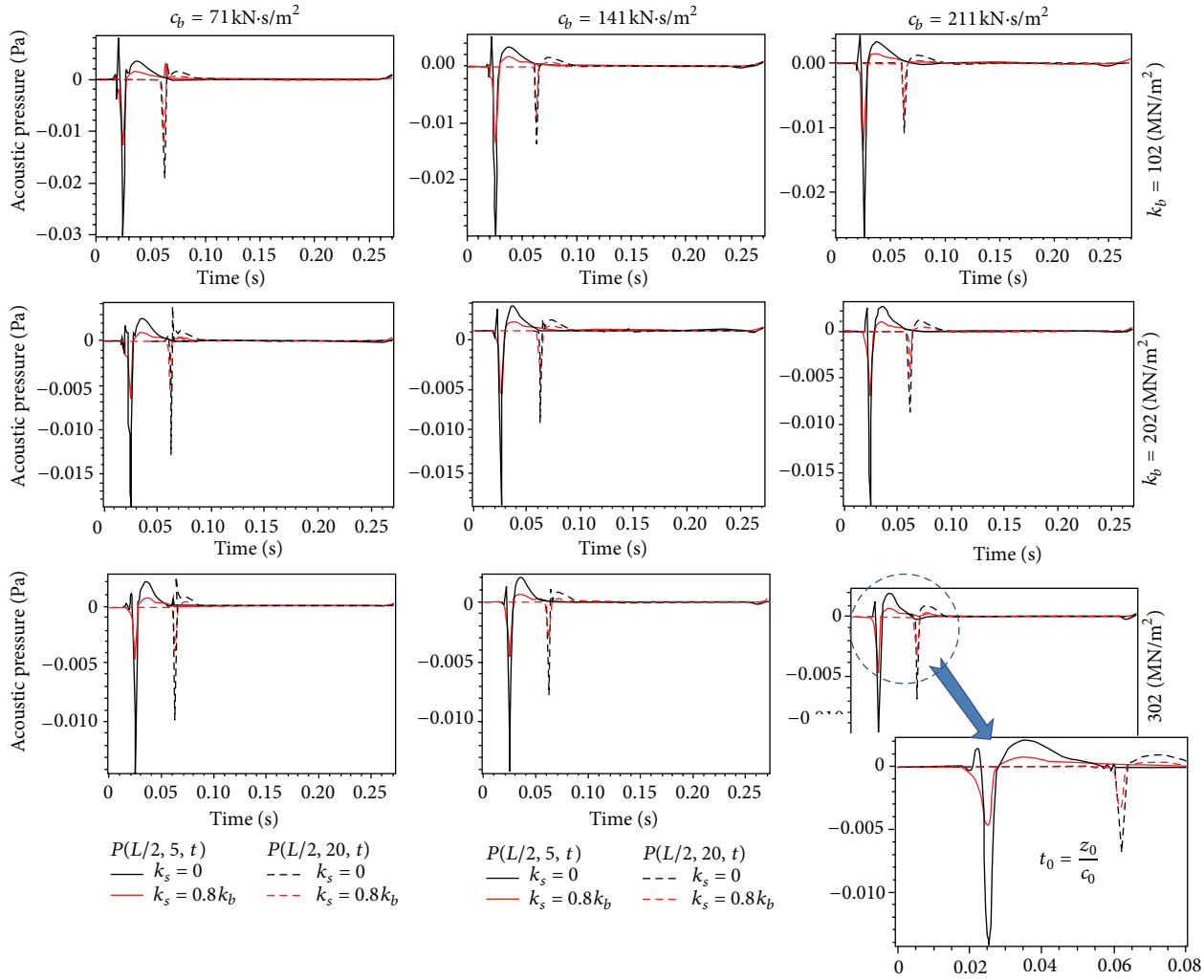

Figure 4: Acoustic pressure at different heights (midspan).

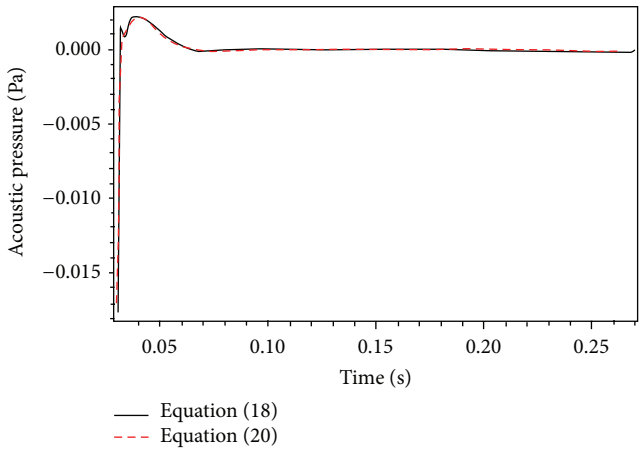

Figure 5: Comparison between two methods for calculating acoustic radiation.

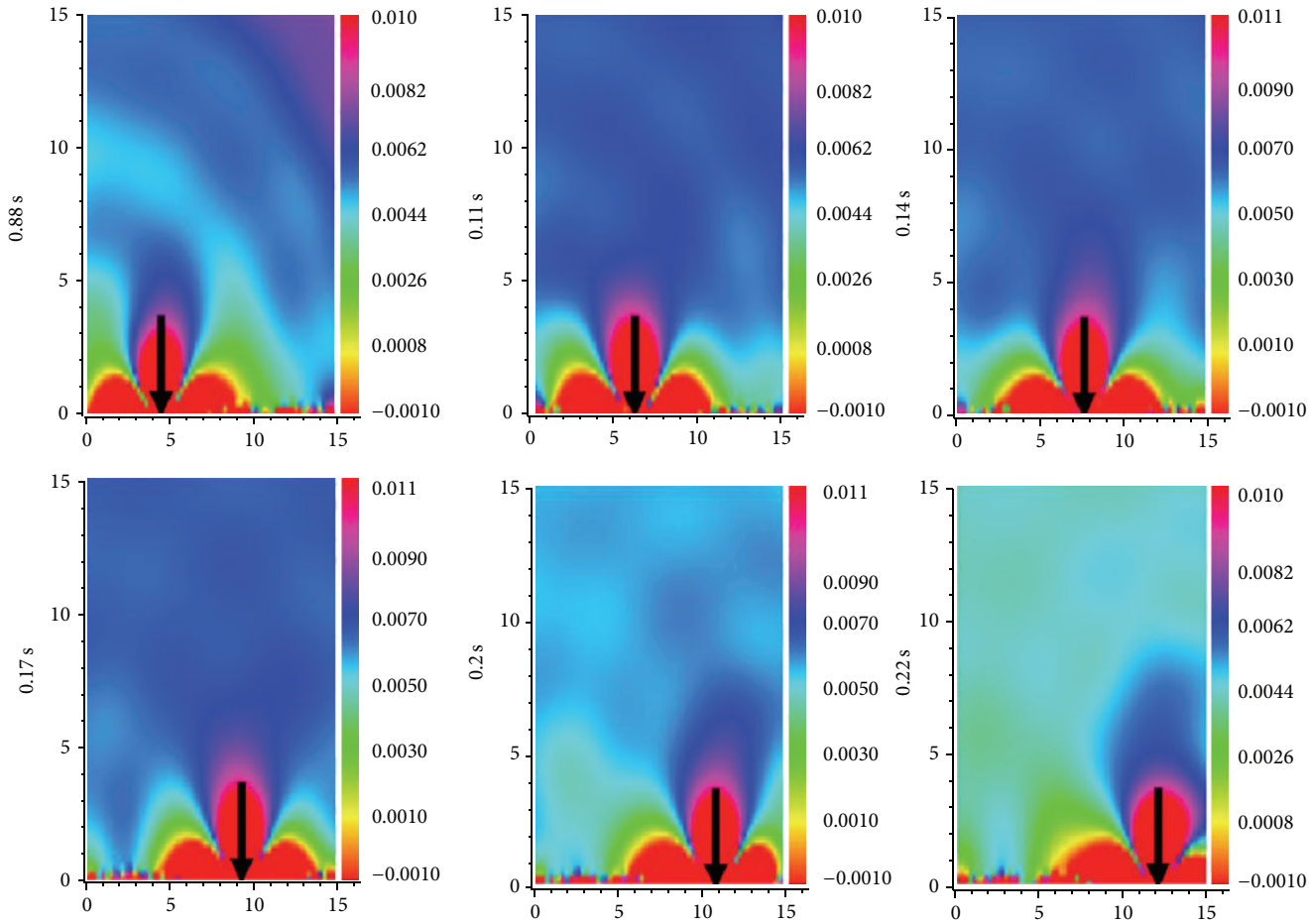

Figure 6: Acoustic pressure field (Pa) along the beam (15 m) at different positions of moving load.

therefore, it must be calculated by numerical techniques such as standard trapezoidal rule [26]. On the other hand, robustness of (19) was seen in both of the mentioned time spans.

Figure 6 shows the series of time snapshots of acoustic pressure distribution while the moving load is passing on the beam for shear layer coefficient $k_s = 0.8\,k_b$, length of the beam $L = 15$, bending layer coefficient $k_b = 202\,\mathrm{MN/m^2}$, viscous coefficient $c = 141\,\mathrm{kN{\cdot}sec/m^2}$, and typical vehicle load (65 kN). The acoustic pressure fields around the beam show that maximum distribution pressure appears around the location of the moving load which is a result of maximum deflection of the beam.

4. Conclusion

In this paper, transient response of simply supported, Euler-Bernoulli beam resting on viscoelastic foundation subjected to a moving load is studied. Based on the Rayleigh integral and dynamic response of the beam, the acoustic pressure distribution around the beam was obtained for the first time. The time responses of the beam with and without shear stiffness effects of the soil are presented for various foundations of moving load. The effects of $k_s = 0$ and $k_s = 0.8\,k_b$ can be easily observed from Figure 4. The most important observations are summarized as follows:

(i) the beam structural vibration is observed to radiate sound into acoustic medium. In particular, increasing the magnitude of foundation is seen to decrease the acoustic pressure;

(ii) increasing the height of selected points decreases the acoustic pressure radiation, while the time response keeps the same trend;

(iii) the delay of the first acoustic pressure wave radiated from the beam is easily seen;

(iv) the contours of acoustic pressure fields around the beam show that maximum distribution pressure appears around the location of the moving load which is a result of maximum deflection of the beam.

Conflict of Interests

The authors declare that there is no conflict of interests regarding the publication of this paper.

References

[1] M. Hetenyi, in *Beams on Elastic Foundations*, vol. 16 of *Scientific Series*, The University of Michigan Press, University of Michigan Studies, Ann Arbor, Mich, USA, 1946.

[2] L. Andersen, S. R. K. Nielsen, and P. H. Kirkegaard, "Finite element modelling of infinite Euler beams on Kelvin foundations exposed to moving loads in convected co-ordinates," *Journal of Sound and Vibration*, vol. 241, no. 4, pp. 587–604, 2001.

[3] D. Thambiratnam and Y. Zhuge, "Dynamic analysis of beams on an elastic foundation subjected to moving loads," *Journal of Sound and Vibration*, vol. 198, no. 2, pp. 149–169, 1996.

[4] L. Fryba, *Vibration of Solids and Structures Under Moving Loads*, Thomas Telford, London, UK, 1999.

[5] J. T. Kenney, "Steady-state vibrations of beam on elastic foundation for moving load," *Journal of Applied Mechanics*, vol. 21, pp. 359–364, 1954.

[6] M. H. Kargarnovin, D. Younesian, D. J. Thompson, and C. J. C. Jones, "Response of beams on nonlinear viscoelastic foundations to harmonic moving loads," *Computers and Structures*, vol. 83, no. 23-24, pp. 1865–1877, 2005.

[7] M. H. Kargarnovin and D. Younesian, "Dynamics of Timoshenko beams on Pasternak foundation under moving load," *Mechanics Research Communications*, vol. 31, no. 6, pp. 713–723, 2004.

[8] D. Younesian and M. H. Kargarnovin, "Response of the beams on random Pasternak foundations subjected to harmonic moving loads," *Journal of Mechanical Science and Technology*, vol. 23, no. 11, pp. 3013–3023, 2010.

[9] G. Muscolino and A. Palmeri, "Response of beams resting on viscoelastically damped foundation to moving oscillators," *International Journal of Solids and Structures*, vol. 44, no. 5, pp. 1317–1336, 2007.

[10] L. Andersen, S. R. K. Nielsen, and R. Iwankiewicz, "Vehicle moving along an infinite beam with random surface irregularities on a Kelvin foundation," *Journal of Applied Mechanics, Transactions ASME*, vol. 69, no. 1, pp. 69–75, 2002.

[11] Y. Weitsman, "Onset of separation between a beam and a tensionless elastic foundation under a moving load," *International Journal of Mechanical Sciences*, vol. 13, no. 8, pp. 707–711, 1971.

[12] J. Choros and G. G. Adams, "Steadily moving load on an elastic beam resting on a tensionless winkler foundation," *Journal of Applied Mechanics, Transactions ASME*, vol. 46, no. 1, pp. 175–180, 1979.

[13] L. Lin and G. G. Adams, "Beam on tensionless elastic foundation," *Journal of Engineering Mechanics*, vol. 113, no. 4, pp. 542–553, 1987.

[14] M. Shamalta and A. V. Metrikine, "Analytical study of the dynamic response of an embedded railway track to a moving load," *Archive of Applied Mechanics*, vol. 73, no. 1-2, pp. 131–146, 2003.

[15] C. R. Steele, "The Timoshenko beam with a moving Load," *Journal of Applied Mechanics*, vol. 35, no. 3, pp. 481–488, 1968.

[16] Y.-H. Chen and Y.-H. Huang, "Dynamic stiffness of infinite Timoshenko beam on viscoelastic foundation in moving coordinate," *International Journal for Numerical Methods in Engineering*, vol. 48, no. 1, pp. 1–18, 2000.

[17] Y.-H. Chen and Y.-H. Huang, "Dynamic characteristics of infinite and finite railways to moving loads," *Journal of Engineering Mechanics*, vol. 129, no. 9, pp. 987–995, 2003.

[18] Y. Yang and X. Ge, "A new method for vibration response of beam on foundation under moving load," *International Journal of Modern Physics B*, vol. 22, no. 31-32, pp. 5615–5620, 2008.

[19] A. D. Senalp, A. Arikoglu, I. Ozkol, and V. Z. Dogan, "Dynamic response of a finite length euler-bernoulli beam on linear and nonlinear viscoelastic foundations to a concentrated moving force," *Journal of Mechanical Science and Technology*, vol. 24, no. 10, pp. 1957–1961, 2010.

[20] V. Z. Vlasov and U. N. Leont'ev, *Beams, Plates and Shells on Elastic Foundations*, Israel Program for Scientific Translations, Jerusalem, Israel, 1966.

[21] D. Basu and N. S. V. Kameswara Rao, "Analytical solutions for Euler-Bernoulli beam on visco-elastic foundation subjected to moving load," *International Journal for Numerical and Analytical Methods in Geomechanics*, vol. 37, no. 8, pp. 945–960, 2013.

[22] S. S. Rao, *Vibration of Continuous Systems*, Wiley, New York, NY, USA, 2007.

[23] J. N. Reddy, *Theory and Analysis of Elatic Plates and Shells*, CRC Press, New York, NY, USA, 2007.

[24] F. Durbin, "Numerical inversion of laplace transforms: an efficient improvement to dubner and abate's method," *Computer Journal*, vol. 17, no. 4, pp. 371–376, 1974.

[25] S. M. Hasheminejad, R. Shakeri, and S. Rezaei, "Vibro-acoustic response of an elliptical plate-cavity coupled system to external shock loads," *Applied Acoustics*, vol. 73, no. 8, pp. 757–769, 2012.

[26] F. T. K. Au and M. F. Wang, "Sound radiation from forced vibration of rectangular orthotropic plates under moving loads," *Journal of Sound and Vibration*, vol. 281, no. 3–5, pp. 1057–1075, 2005.

[27] M. C. Junger and D. Feit, *Sound, Structures and Interaction*, MIT Press, Cambridge, Mass, USA, 1986.

Hindawi Publishing Corporation
Shock and Vibration
Volume 2014, Article ID 697450, 5 pages
http://dx.doi.org/10.1155/2014/697450

Research Article

Vibration Transfer Path Analysis and Path Ranking for NVH Optimization of a Vehicle Interior

B. Sakhaei[1] and M. Durali[2]

[1] *Department of Mechanical Engineering, Sharif University of Technology and NVH Department of Iran Khodro Powertrain Company (IPCO), Tehran 11365-11155, Iran*
[2] *Department of Mechanical Engineering, Sharif University of Technology, Tehran 11365-11155, Iran*

Correspondence should be addressed to M. Durali; durali@sharif.edu

Received 19 October 2012; Accepted 19 November 2012; Published 17 June 2014

Academic Editor: Hamid Ahmadian

By new advancements in vehicle manufacturing, evaluation of vehicle quality assurance has got a more critical issue. Today noise and vibration generated inside and outside the vehicles are more important factors for customers than before. So far several researchers have focused on interior noise transfer path analysis and the results have been published in related papers but each method has its own limitations. In present work, the vibration transfer path analysis and vibration path ranking of a car interior have been performed. As interior vibration is a source of structural borne noise problem, thus, the results of this research can be used to present the structural borne noise state in a vehicle. The proposed method in this paper does not need to disassemble the powertrain from the chassis. The procedure shows a good ability of vibration path ranking in a vehicle and is an effective tool to diagnose the vibration problem inside the vehicle. The simulated vibration spectrums in different speeds of the engine have a good compliance with the tested results; however, some incompatibilities exist and have been discussed in detail. The simulated results show the strength of the method in engine mount optimization.

1. Introduction

Noise and vibration which are perceived by passengers in a vehicle are important in the pleasantness of customers. Transfer path analysis of noise in a vehicle is a subject that many researchers from the 90s up to now have worked on it to find the root cause of a noise problem in a vehicle. By taking help of these methods, the paths of noise, which usually starts from engine, mounts through body, and ends to passenger compartment, are investigated. Transfer path analysis can find the weak points of every path of the vehicle; then, the paths of high noise are identified and ranked. An NVH engineer then is able to find the problem and find a design solution for making the transmission of noise better.

The earliest work in this subject refers to Bendat and Piersol [1] in 1980 which used coherence analysis of the noise paths to find various contributions. In late 80s, an alternate method was proposed which considers the system as a source-transfer function-receiver and assumes that the noise in a vehicle compartment is a linear summation of different paths. In this method the response in target point in vehicle compartment is determined by multiplication of interface loading and transfer function from engine mount to that target point. Then noise contributions are summed to get the overall noise in the vehicle [2, 3]. As it is clear, the main challenge in this method is measuring the interface loads [3].

Because of complexity in measuring the excitation forces on interfaces, the indirect procedures were developed. In these methods there is no need for direct measurement of interfacing forces. Instead, FRFs between all points of source and the FRFs between source and receiver (targets) are measured. Then, by inversing the FRF matrices and multiplying it with the operational accelerations at the input side, the shares of each path from overall noise are calculated [4]. Although much advancement has promoted this method, and the accuracy of the results has been improved, indirect measurements have the limitations of cost and time of tests. In 2008, a new method based on operational modal analysis

was proposed. This method named operational path analysis (OPA) which shortened the test time but it had accuracy problem because excitation in one direction often has side effect responses in other directions and putting this method into effect needs high experience [5].

Multilevel TPA has the strength of indirect measurement but can be done in a shorter time relative to indirect method. It was first introduced in 2002 by Eisele et al. [6] which analyzed the interior structural noise in a vehicle. However the method is effective in prediction of the critical paths but less attention has been paid to it.

Although almost all publications in interior noise transfer path analysis have focused on interior noise simulation, there is no work on the interior vibration simulation. In this paper, an interior vibration simulation of the vehicle for the first time was done. The method was based on multilevel TPA and the results show that this method has the ability of TPA analysis effectively. It is a fast method which rarely has the problem of measurement noise interfering. The results show that vehicle interior vibration simulation has good potential of engine mount optimization behaviour. By this method, also vibration fault diagnosis is more effective than conventional noise path ranking methods.

2. General Formulation

Vibrations in a vehicle mostly transfer from engine mount locations through vibration transfer paths into the body of the car and finally receives to the target locations in passenger compartment. Elements in vibration generation and transfer into the vehicle are divided into two major parts: active and passive elements. IC engine is an active vibration source, and the engine mounts and body transfer functions from mount locations to target points in the vehicle compartment are passive elements.

In passive part of vibration transfer, each engine mount in each vehicle principal coordinate comprises one path. Thus, for a vehicle with 3 engine mounts, there are 9 transfer paths. These engine mount paths beside relative body and chassis transfer functions send vibration energy to the passenger compartment.

Basic equation in transfer path analysis assumes that the total noise and vibration felt at passenger position are superposing the contribution of each path. Equation (1) implies the relation [4] as follows:

$$y(f) = \sum_{1}^{n} y_i(f), \tag{1}$$

where $y(f)$ = vibration at passenger location and $y_i(f)$ = contribution of vibration from each path.

The system approach to the transfer path analysis explains that the partial contribution $y_i(f)$ of the vibration in the target point is a product of input force of the active part and the transfer function between the interface and the receiver like

$$y_i(f) = \mathrm{FRF}_{ik}(f) * F_i(f). \tag{2}$$

By combining (1) and (2), general basic equation of transfer path analysis is given by

$$y(f) = \sum_{i=1}^{n} \mathrm{FRF}_{ik}(f) * F_i(f). \tag{3}$$

As it is clear from (3), it is assumed that vibration transfer paths have linear behaviour. Also it is obvious that transfer path analysis is performed in frequency region. In this method, as soon as any problem arises in overall amplitude of vibration, the different path contribution will be investigated and the responsible path for that problem will be identified. As each contribution is equal to the product of the input force and the transfer function, then, it is easier to locate the exact location of problem.

Multilevel TPA is classified in fast TPA groups of methods in which the contribution to a target response is a chain of linked subsystems. In this method, few FRF measurements are being performed and then by multiplying the input signal to this chain, the output will be the vibration share of each path at target location (4). Consider

$$\{y_i(f)\} = [H_1][H_2][H_3]\cdots\{F_i(f)\}, \tag{4}$$

where $F_i(f)$ = input forces at engine mount interface.

By noting (4), the basic equation of multilevel TPA can be written as follows:

$$\begin{aligned}\{a_{\text{interior}}\} &= \{F_i(f)\} \times \frac{a_{\text{interior}}}{a_{\text{body}}(f)} \longrightarrow \frac{a_{\text{interior}}}{F_{\text{body}}(f)} \\ &= a_{\text{engine}}(f) \times \frac{a_{\text{body}}(f)}{a_{\text{engine}}(f)} \times \frac{F_{\text{body}}(f)}{a_{\text{body}}(f)} \\ &\quad \times \frac{a_{\text{interior}}(f)}{F_{\text{body}}(f)}.\end{aligned} \tag{5}$$

According to (5), for evaluation of a_{interior} from each path, it is needed to measure three transfer functions of mount transmissibility, apparent mass, and chassis transfer function, respectively.

3. Interior Vibration Simulation of a Sedan Car

For evaluation of interior vibration in a sedan car compartment, a procedure of interior vibration simulation was applied based on multilevel TPA. The vehicle was equipped with a four-cylinder engine of 1.7 L. The engine and gearbox were installed on the chassis with three mounts, two rubber mounts and one hydraulic mount. The mounts are named RH mount, LH mount, and Rear mount. The RH mount was a hydraulic mount and LH and Rear mounts were rubber mounts. Figure 1 shows the transverse engine mounting system [7].

According to (5), two transfer functions of apparent mass and body were measured by presence of engine on the vehicle. In some publications the transfer function was measured without engine. As it was tested (the results have not been

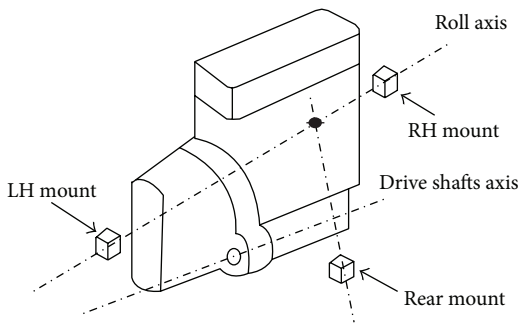

Figure 1: Transverse engine mounting system [7].

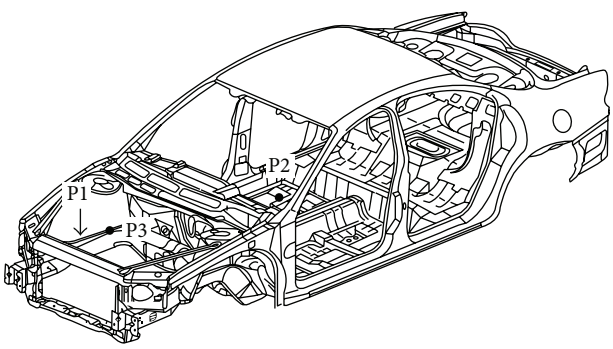

Figure 2: P1: hammer excitation, P2: triaxial accelerometer for body transfer function, and P3: triaxial accelerometer for chassis apparent mass [7].

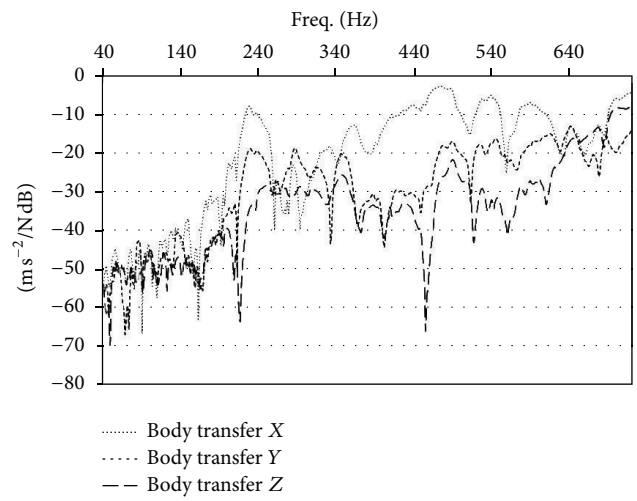

Figure 3: Body transfer function of RH mount at different directions.

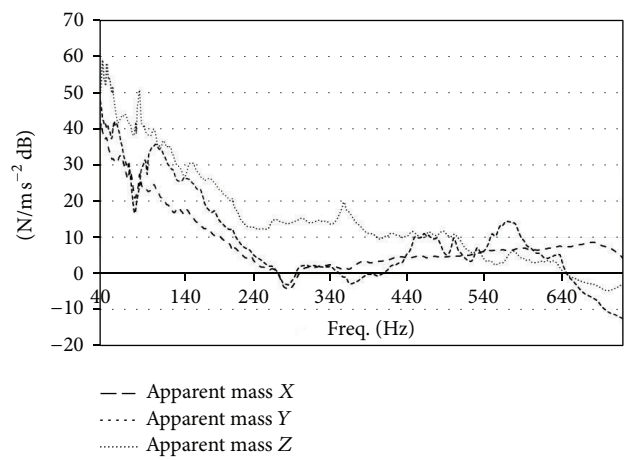

Figure 4: Apparent mass of RH mount region.

reported), transfer functions without engine caused significant error in calculating the contributions.

All of the measurements were performed with a B&K 3570 data acquisition with 25 Khz range FFT analyzer. There are two 4524 B&K triaxial accelerometers and a piezoelectric impact hammer of maximum 5 KN force range. The signals were recorded with a 7 Hz high pass filter to prevent double hit error of impact hammer.

First, the body transfer function ($a_{\text{interior}}(f)/F_{\text{body}}(f)$) was measured by exciting the engine mount location with an impact hammer. The impact was applied on the body side of engine mount and the force was measured with piezoelectric element of hammer. Simultaneously, a triaxial accelerometer was installed on the vehicle compartment floor (point P2 in Figure 2). As it was mentioned, the excitation was applied at presence of engine and gearbox at original location. The frequency span of the body transfer function was taken up to 800 Hz because only the interior vibration of the vehicle was important. The frequency resolution of FFT analyzer was 0.25 Hz.

Figure 3 shows the body transfer function between RH mount location and vehicle compartment on passenger foot bottom at different principal directions.

Apparent mass also was measured at engine mount locations. A triaxial accelerometer was installed on body near the engine mount location of the vehicle and the impact hammer applied the force beside the accelerometer position (Figure 2). By calculating the ratio of $F_{\text{body}}(f)/a_{\text{body}}(f)$ an approximation of apparent mass could be got (Figure 4).

Mount transmissibility is the ratio of acceleration on both sides of the mount on engine and body sides. The mount transmissibility was calculated by installing one accelerometer on engine side of each mount and another accelerometer on chassis side of mounts. Input and output acceleration on each engine mount were measured during a run-up of engine speed on the chassis dynamometer. The 3rd gear was engaged during the test and engine was under full load condition (fully open throttle). Figure 5 shows the test setup to measure the mount transmissibility on chassis dyno.

The coherency spectrum of the mount transmissibility signal showed that only the main orders of the engine were coherent. Then only the transmissibility of these main orders was taken into account.

With a Matlab code the transmissibility of each mount at each direction was calculated at different engine speeds.

By multiplying the derived transfer functions with the input acceleration on engine side and summing the vibrations

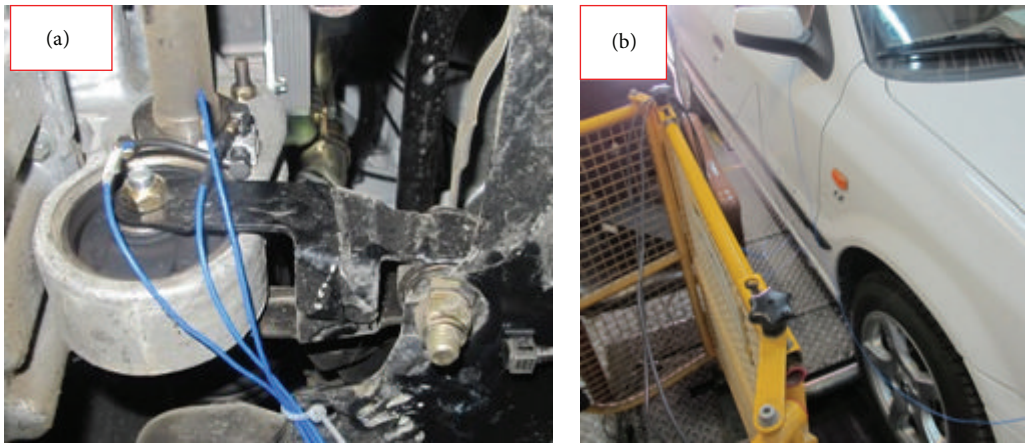

Figure 5: Test setup—(a) accelerometer installation on both sides of engine mount, (b) vehicle on chassis dyno.

from different paths, the interior acceleration at passenger foot bottom could be simulated.

For comparison between simulated and real vibration at target point, a triaxial accelerometer also mounted at the target point (Figure 2 P3) and simultaneously during the run-up test, the vibration was measured. The results of the measurements are expressed in the next section.

4. Results

Calculation of mount dynamic stiffness in real conditions of mounts preload, temperature, and under engine operation is one valuable benefit of multilevel TPA, while dynamic mount stiffness measurement in test lab by a power shaker usually has large error.

Mount dynamic stiffness will be in hand by multiplying the mount transmissibility and apparent mass at different frequencies (see (5)).

Figure 6 shows the mount dynamic stiffness of RH mount. The mount dynamic stiffness decreases with frequency which complies with conventional engine mounts [6].

Figure 7 shows the comparison between simulated and measured overall accelerations at target point. There is a complete accordance between the trends of simulated and real signal but also still some differences exist.

The differences between measured and simulated vibration signal in the vehicle come from the damping of the materials which covered the chassis of the vehicle on the foot bottom region. It was an asphalt layer. The property of damping of asphalt in this region is nonlinear which depends on temperature. As described earlier, the linear transfer function of body was taken into account in the analysis; then, the damping nonlinear behaviour of this layer cannot be considered in the analysis.

The effect of damping also grows with the velocity of excitation. Therefore, at higher speeds the measured vibration curve in Figure 7 was below the simulated results.

These evidences show that the damping of body transfer paths has nonlinear frequency dependent behaviour and this property should be studied with more care.

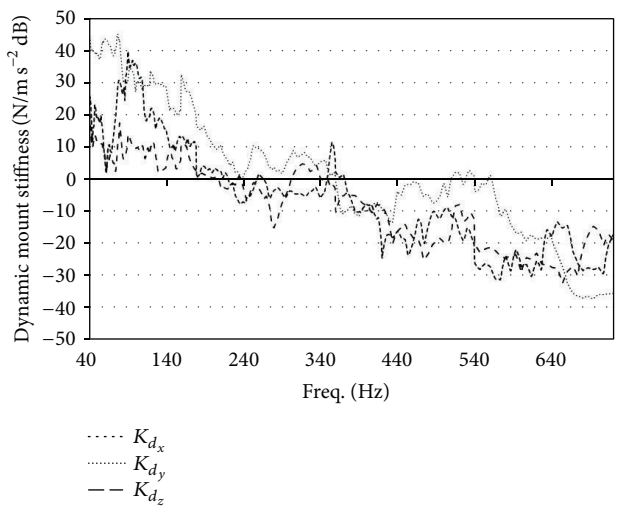

Figure 6: Dynamic mount stiffness derived by simulation.

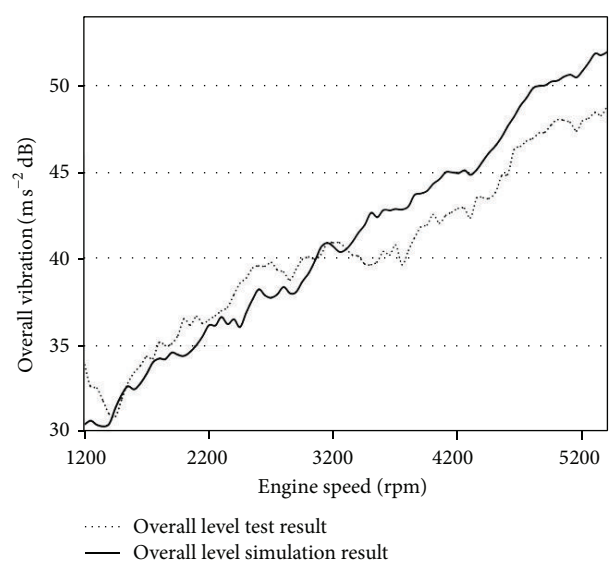

Figure 7: Dynamic mount stiffness derived by simulation.

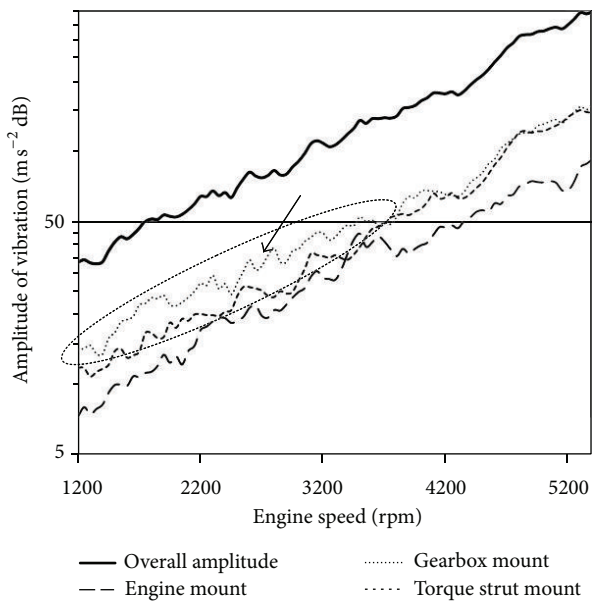

Figure 8: Dynamic mount stiffness obtained by simulation.

Figure 8 shows the contribution of each mount in overall vibration level. The LH mount has higher share of vibration in the compartment during engine run-up especially from 1000 to 3500 rpm although RH mount behaviour in vibration transmission is desirable.

This shows that LH mount needs to be modified. Then softening of the LH mount can be a solution to this problem. Of course the side effect of mount softening on rigid body displacements of engine should be studied.

5. Conclusion

Although there were many advancements in the transfer path analysis of noise in the vehicle, rare publications exist on vibration simulation of vehicle interior. Interior vibration of a vehicle can be taken as a representative of structural borne noise. Also vibration simulation of a vehicle interior is a powerful tool for engine mounts optimization. As it was proved, one can give applicable modifications on engine mount system to make the vibration behaviour better. Vibration TPA can realize the dynamic weak points of body chassis.

The results of vehicle interior vibration simulation and real measurements of this quantity showed a good compliance. The existing differences come from the nonlinear damping effect. Because of the linear assumption of body transfer functions in this method, these differences are inevitable.

A complete study on damping ratio effect on the simulated signal and also detailed mount optimization by this method will be performed in the next work. Also, further investigations are needed to be made on the effect of different gears on the amount of vibration at target point.

Conflict of Interests

The authors declare that there is no conflict of interests regarding the publication of this paper.

Acknowledgment

The authors are grateful to the IPCO (Iran Khodro Powertrain Company) for supporting this research.

References

[1] J. S. Bendat and A. G. Piersol, *Engineering Applications of Correlation and Spectral Analysis*, John Wiley & Sons, New York, NY, USA, 1980.

[2] J. Verheij, *Multipath sound transfer from resiliently mounted shipboard machinery [Ph.D. thesis]*, Technische Physische Dienst TNO-TH, Delft, The Netherlands, 1986.

[3] D. de Vis, W. Hendricx, and P. van der Linden, "Development and integration of an advanced unified approach to structure borne noise analysis," in *Proceedings of the 2nd International Conference on Vehicle Comfort*, pp. 465–473, ATA, October 1992.

[4] K. Janssens, P. Mas, L. Gielen, P. Gajdatsy, and H. van der Auweraer, "A novel transfer path analysis method delivering a fast and accurate noise contribution assessment," in *Proceedings of the SAE Symposium on Ineternational Automotive Technology*, SAE Paper no. 2009-26-047, 2009.

[5] P. Gajdatsy, K. Janssens, W. Desmet, and H. van der Auweraer, "Application of the transmissibility concept in transfer path analysis," *Mechanical Systems and Signal Processing*, vol. 24, no. 7, pp. 1963–1976, 2010.

[6] N. W. Alt, N. Wiehagen, and M. W. Schlitzer, "Interior noise simulation for improved vehicle sound," in *Proceedings of the SAE Noise and Vibration Conference and Exposition*, SAE Paper no. 2001-01-1539, 2001.

[7] J. C. Brown, A. J. Robertson, and S. T. Serpento, *Motor Vehicle Structures: Concepts and Fundamentals*, Butterworth Heinemann, Oxford, UK, 2002.

Hindawi Publishing Corporation
Shock and Vibration
Volume 2014, Article ID 410514, 6 pages
http://dx.doi.org/10.1155/2014/410514

Research Article

Calculation of Wave Dispersion Curves in Multilayered Composite-Metal Plates

Ameneh Maghsoodi,[1] Abdolreza Ohadi,[1] and Mojtaba Sadighi[2]

[1] *Acoustics Research Laboratory, Department of Mechanical Engineering, Amirkabir University of Technology, 424 Hafez Avenue, Tehran 15916-34311, Iran*
[2] *Department of Mechanical Engineering, Amirkabir University of Technology, 424 Hafez Avenue, Tehran 15916-34311, Iran*

Correspondence should be addressed to Abdolreza Ohadi; a_r_ohadi@aut.ac.ir

Received 19 October 2012; Accepted 19 November 2012; Published 12 June 2014

Academic Editor: Hamid Mehdigholi

The major purpose of this paper is the development of wave dispersion curves calculation in multilayered composite-metal plates. At first, equations of motion and characteristic equations for the free waves on a single-layered orthotropic plate are presented. Since direction of wave propagation in composite materials is effective on equations of motion and dispersion curves, two different cases are considered: propagation of wave along an axis of material symmetry and along off-axes of material symmetry. Then, presented equations are extended for a multilayered orthotropic composite-metal plate using the transfer matrix method in which a global transfer matrix may be extracted which relates stresses and displacements on the top layer to those on the bottom one. By satisfying appropriate boundary conditions on the outer boundaries, wave characteristic equations and then dispersion curves are obtained. Moreover, presented equations may be applied to other materials such as monoclinic, transversely isotropic, cubic, and isotropic materials. To verify the solution procedure, a number of numerical illustrations for a single-layered orthotropic and double-layered orthotropic-metal are presented.

1. Introduction

Nondestructive inspection based on the propagation of elastic waves that relies generally on calculation of dispersion curves plays an important role in damage identification in multilayered structures. From this point of view, calculation of dispersion curves is one of the essential stages for inspection of structures.

Most of the researches have been done on the single-layered isotropic or quasi-isotropic materials [1, 2]. However, Nayfeh [3] has presented a transfer matrix technique to obtain the dispersion curves of elastic waves propagating in multilayered anisotropic media, that is, composite laminates. Demcenko and Mazeika [4] have developed global matrix method to calculate dispersion curves of multilayered isotropic plate. Lowe [5] has presented a review of development of the matrix method and global matrix method to obtain dispersion curves in isotropic materials. Also, they have discussed the problems with large value of frequency thickness, material damping, and leaky wave. Verma [6] has investigated the harmonic thermoelastic waves and dispersion relations in layered anisotropic plate by utilizing the transfer matrix method.

Nowadays, composite-metal structures have developed significantly in the industry because of the great mechanical properties rather than other materials. Furthermore, damage detection using wave propagation is one of the most interesting topics that have attracted the attention of researchers. Thus, in this paper, we extend the relations of dispersion curves for multilayered composite-metal plates using the transfer matrix method presented in previous studies. Presented procedure can be used for damage detection in multilayered composite-metal structures using the wave propagation methods.

2. Wave Propagation Formulation

2.1. Wave Propagation in a Single-Layered Orthotropic Plate. Consider an orthotropic plate stacked normal to the axis

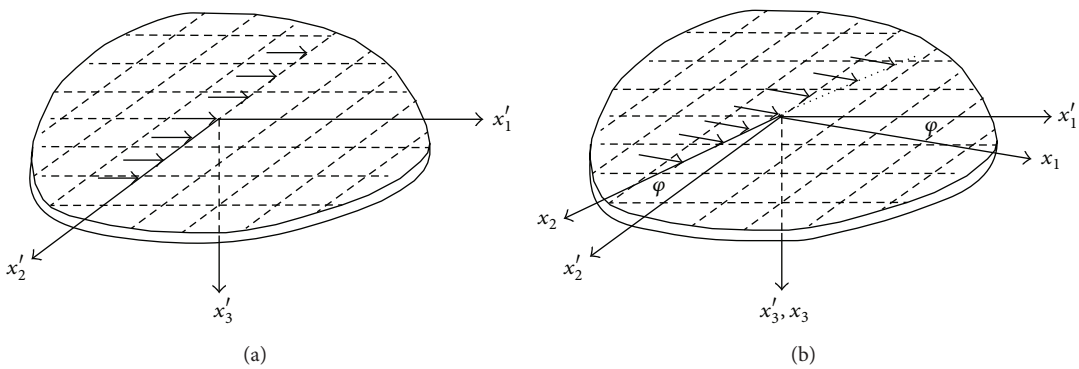

Figure 1: Wave propagation along (a) principle-axes and (b) off-principle-axes.

x_3 of the global coordinate system (x_1, x_2, x_3) and consider $x_1 - x_2$ plane coincides with the upper surface of the plate. Generally, the global coordinate system (x_1, x_2, x_3) does not coincide with the principle material coordinate system (x_1', x_2', x_3'). In this paper two different cases are considered: wave propagation along principle-axes, x_1' or x_2', and wave propagation along off-principle-axes (see Figure 1).

2.1.1. Wave Propagation along Principle-Axes. With respect to the local coordinate system (x_1', x_2', x_3'), equations of motion are as follows:

$$\frac{\partial \sigma_{11}'}{\partial x_1'} + \frac{\partial \sigma_{12}'}{\partial x_2'} + \frac{\partial \sigma_{13}'}{\partial x_3'} = \rho \frac{\partial^2 u_1'}{\partial t^2}, \tag{1a}$$

$$\frac{\partial \sigma_{12}'}{\partial x_1'} + \frac{\partial \sigma_{22}'}{\partial x_2'} + \frac{\partial \sigma_{23}'}{\partial x_3'} = \rho \frac{\partial^2 u_2'}{\partial t^2}, \tag{1b}$$

$$\frac{\partial \sigma_{13}'}{\partial x_1'} + \frac{\partial \sigma_{23}'}{\partial x_2'} + \frac{\partial \sigma_{33}'}{\partial x_3'} = \rho \frac{\partial^2 u_3'}{\partial t^2}, \tag{1c}$$

and stress-strain relations are given by

$$\begin{Bmatrix} \sigma_{11}' \\ \sigma_{22}' \\ \sigma_{33}' \\ \sigma_{23}' \\ \sigma_{31}' \\ \sigma_{12}' \end{Bmatrix} = \begin{bmatrix} C_{11}' & C_{12}' & C_{13}' & 0 & 0 & 0 \\ C_{12}' & C_{22}' & C_{23}' & 0 & 0 & 0 \\ C_{13}' & C_{23}' & C_{33}' & 0 & 0 & 0 \\ 0 & 0 & 0 & C_{44}' & 0 & 0 \\ 0 & 0 & 0 & 0 & C_{55}' & 0 \\ 0 & 0 & 0 & 0 & 0 & C_{66}' \end{bmatrix} \begin{Bmatrix} \varepsilon_{11}' \\ \varepsilon_{22}' \\ \varepsilon_{33}' \\ \varepsilon_{23}' \\ \varepsilon_{31}' \\ \varepsilon_{12}' \end{Bmatrix}, \tag{2}$$

where $\sigma', \varepsilon', u'$ are the components of stress, strain, and displacement, respectively, and ρ and C' are the material density and stiffness coefficient, respectively.

Furthermore, the linear strain-displacement relations are

$$\varepsilon_{11}' = \frac{\partial u_1'}{\partial x_1'}, \qquad \varepsilon_{22}' = \frac{\partial u_2'}{\partial x_2'}, \qquad \varepsilon_{33}' = \frac{\partial u_3'}{\partial x_3'},$$
$$\varepsilon_{23}' = \frac{\partial u_2'}{\partial x_3'} + \frac{\partial u_3'}{\partial x_2'}, \qquad \varepsilon_{31}' = \frac{\partial u_1'}{\partial x_3'} + \frac{\partial u_3'}{\partial x_1'}, \tag{3}$$
$$\varepsilon_{12}' = \frac{\partial u_2'}{\partial x_1'} + \frac{\partial u_1'}{\partial x_2'}.$$

Substituting (2) and (3) into (1a), (1b), and (1c) concludes the three following equations:

$$C_{11}' \frac{\partial^2 u_1'}{\partial x_1'^2} + C_{55}' \frac{\partial^2 u_1'}{\partial x_3'^2} + \left(C_{13}' + C_{55}'\right) \frac{\partial^2 u_3'}{\partial x_1' \partial x_3'} = \rho \frac{\partial^2 u_1'}{\partial t^2}, \tag{4a}$$

$$C_{66}' \frac{\partial^2 u_2'}{\partial x_1'^2} + C_{44}' \frac{\partial^2 u_2'}{\partial x_3'^2} = \rho \frac{\partial^2 u_2'}{\partial t^2}, \tag{4b}$$

$$C_{33}' \frac{\partial^2 u_3'}{\partial x_3'^2} + C_{55}' \frac{\partial^2 u_3'}{\partial x_1'^2} + \left(C_{13}' + C_{55}'\right) \frac{\partial^2 u_1'}{\partial x_1' \partial x_3'} = \rho \frac{\partial^2 u_3'}{\partial t^2}. \tag{4c}$$

Two coupled equations, (4a) and (4c), are related to pressure wave (P wave) and shear vertical wave (SV wave). Also, the uncoupled equation (4b) is related to horizontal wave (SH wave). Formal solutions for these equations are assumed as follows [3]:

$$u_j' = U_j e^{ik(x_1' + \beta x_3' - ct)}, \quad j = 1, 2, 3, \tag{5}$$

where U_j and c are displacement amplitude along direction x_j' and phase velocity in direction x_1', respectively, and $k(= \omega/c)$, ω, and β are x_1'-component of wavenumber and ratio of x_3', circular frequency, and x_1'-components of wavenumber, respectively. For clarification, the rest of the solution procedure for coupled and uncoupled equations is described next.

(a) Solution for SH wave: according to (5), it is assumed the solution of (4b) has the following form:

$$u_2' = U_2 e^{ik(x_1' + \beta x_3' - ct)}; \tag{6}$$

substituting (6) into (4b) results in

$$\beta_1 = -\beta_2 = \left[\frac{\left(\rho c^2 - C_{66}'\right)}{C_{44}'} \right]^{1/2}; \tag{7}$$

therefore

$$u_2' = U_{21}e^{ik(x_1'+\beta_1 x_3'-ct)} + U_{22}e^{ik(x_1'+\beta_2 x_3'-ct)}. \quad (8)$$

Also, stress-strain relation is

$$\sigma_{23}' = C_{44}'\frac{\partial u_2'}{\partial x_3'}; \quad (9)$$

thus

$$\sigma_{23}' = ikC_{44}'\left[\beta_1 U_{21}e^{ik(x_1'+\beta_1 x_3'-ct)} + \beta_2 U_{22}e^{ik(x_1'+\beta_2 x_3'-ct)}\right]. \quad (10)$$

Using (8) and (10) and after some simplifications, stress and displacement at $x_3' = 0$ may be related to those at $x_3' = h$ (h is thickness of plate) by following the relation

$$\begin{bmatrix} u_2' \\ \sigma_{23}^* \end{bmatrix}_{x_3'=h} = [T]\begin{bmatrix} u_2' \\ \sigma_{23}^* \end{bmatrix}_{x_3'=0}, \quad \sigma_{23}^* = \frac{\sigma_{23}'}{ik}, \quad (11)$$

where $[T]$is transfer matrix and is given by

$$[T] = \begin{bmatrix} \cos(\beta kh) & \dfrac{i}{(\beta C_{44}')}\sin(\beta kh) \\ i\beta C_{44}'\sin(\beta kh) & \cos(\beta kh) \end{bmatrix}. \quad (12)$$

By invoking free stress boundary conditions at lower and upper surfaces of plate, characteristic equation for single-layered plate may be obtained as follows:

$$T_{21} = 0 \Longrightarrow \sin(\beta kh) = 0. \quad (13)$$

Substituting $k = \omega/c$ into (13) results in an equation with two unknown parameters ω and c called "dispersion equation of SH wave."

(b) Solution for P and SV waves: according to (5), suggested solutions of (4a) and (4c) are

$$u_1' = U_1 e^{ik(x_1'+\beta x_3'-ct)}, \qquad u_3' = U_3 e^{ik(x_1'+\beta x_3'-ct)}. \quad (14)$$

Substituting (14) into (4a) and (4c) results in

$$\begin{bmatrix} C_{11} - \rho c^2 + C_{55}\beta^2 & (C_{13}+C_{55})\beta \\ (C_{13}+C_{55})\beta & C_{55} - \rho c^2 + C_{33}\beta^2 \end{bmatrix}\begin{Bmatrix} U_1 \\ U_3 \end{Bmatrix} = 0. \quad (15)$$

To obtain nontrivial solution, determinant of coefficients matrix of displacement vector is vanished. Therefore, a four-degree polynomial equation in β is obtained as follows:

$$A\beta^4 + B\beta^2 + C = 0. \quad (16)$$

There are four solutions for β or in other words two pairs of solutions for β^2 as follows:

$$\beta_1 = -\beta_2, \qquad \beta_3 = -\beta_4; \quad (17)$$

therefore

$$u_1' = \sum_{j=1}^{4} U_{1j}e^{ik(x_1'+\beta_j x_3'-ct)}, \qquad u_3' = \sum_{j=1}^{4} U_{3j}e^{ik(x_1'+\beta_j x_3'-ct)}. \quad (18)$$

Also, stress-strain relation is

$$\sigma_{33}' = C_{13}'\frac{\partial u_1'}{\partial x_1'} + C_{33}'\frac{\partial u_3'}{\partial x_3'}, \qquad \sigma_{13}' = C_{55}'\left(\frac{\partial u_3'}{\partial x_1'} + \frac{\partial u_1'}{\partial x_3'}\right); \quad (19)$$

thus

$$\sigma_{33}' = \sum_{j=1}^{4} ikD_{1j}U_{1j}e^{ik(x_1'+\beta_j x_3'-ct)},$$
$$\sigma_{13}' = \sum_{j=1}^{4} ikD_{2j}U_{1j}e^{ik(x_1'+\beta_j x_3'-ct)}, \quad (20)$$

where

$$D_{1j} = C_{13}' + C_{33}'\beta_j W_j,$$
$$D_{2j} = C_{55}'\left(\beta_j + W_j\right),$$
$$W_j = \frac{U_{3j}}{U_{1j}} = \frac{\rho c^2 - C_{11}' - C_{55}'\beta_j^2}{\left(C_{13}' + C_{55}'\right)\beta_j}. \quad (21)$$

Using (18), (20), and (21) and after some simplifications, stress and displacement at $x_3' = 0$ may be related to those at $x_3' = h$ (h is thickness of plate) by following the relation

$$\left[u_1' \;\; u_3' \;\; \sigma_{33}' \;\; \sigma_{13}'\right]_{x_3'=h}^{t} = [T]\left[u_1' \;\; u_3' \;\; \sigma_{33}' \;\; \sigma_{13}'\right]_{x_3'=0}^{t}, \quad (22)$$

where $[T]$ is transfer matrix and is given by

$$[T] = T_1 T_2 T_1^{-1},$$
$$T_1 = \begin{bmatrix} 1 & 1 & 1 & 1 \\ W_1 & -W_1 & W_3 & -W_3 \\ D_{11} & D_{11} & D_{13} & D_{13} \\ D_{21} & -D_{21} & D_{23} & -D_{23} \end{bmatrix}, \quad (23)$$
$$T_2 = \operatorname{diag}\left(e^{ik\beta_j h}\right), \quad j = 1, 2, 3, 4.$$

By invoking free stress boundary conditions at lower and upper surfaces of plate, characteristic equation for single-layered plate may be obtained as follows:

$$\begin{vmatrix} T_{31} & T_{32} \\ T_{41} & T_{42} \end{vmatrix} = 0. \quad (24)$$

Substituting $k = \omega/c$ into (24) results in an equation with two unknown parameters ω and c called "dispersion equation of P and SV waves."

2.1.2. Wave Propagation along Off-Principle-Axes. Assume wave propagation along off-principle-axis x_1 (or x_2) with angle φ with respect to principle-axis x_1' (or x_2') as shown in Figure 1(b). In this situation, (4a), (4b), and (4c) are coupled for all materials except isotropic one. The reason is that

transformed stiffness matrix from system (x_1', x_2', x_3') into system (x_1, x_2, x_3) has a monoclinic form as follows:

$$C = \begin{bmatrix} C_{11} & C_{12} & C_{13} & 0 & 0 & C_{16} \\ C_{12} & C_{22} & C_{23} & 0 & 0 & C_{26} \\ C_{13} & C_{23} & C_{33} & 0 & 0 & C_{36} \\ 0 & 0 & 0 & C_{44} & C_{45} & 0 \\ 0 & 0 & 0 & C_{45} & C_{55} & 0 \\ C_{16} & C_{26} & C_{36} & 0 & 0 & C_{66} \end{bmatrix}. \quad (25)$$

Substituting (5) into (1a), (1b), and (1c) results in

$$\begin{aligned} &[K(\beta)]\, U_i = 0, \\ &K_{11} = C_{11} - \rho c^2 + C_{55}\beta^2, \\ &K_{12} = C_{16} + C_{45}\beta^2, \\ &K_{13} = (C_{13} + C_{55})\,\beta, \\ &K_{22} = C_{66} - \rho c^2 + C_{44}\beta^2, \\ &K_{23} = (C_{36} + C_{45})\,\beta, \\ &K_{33} = C_{55} - \rho c^2 + C_{33}\beta^2. \end{aligned} \quad (26)$$

By setting determinant $[K(\beta)]$ equal to zero, a six-degree polynomial equation is obtained as follows:

$$A\beta^6 + B\beta^4 + C\beta^2 + D = 0. \quad (27)$$

There are four solutions for β as follows:

$$\beta_1 = -\beta_2, \qquad \beta_3 = -\beta_4, \qquad \beta_5 = -\beta_6. \quad (28)$$

Therefore, displacements and stress components are given by

$$\begin{aligned} (u_1, u_2, u_3) &= \sum_{j=1}^{6} \left(1, V_j, W_j\right) U_{1j} e^{ik(x_1+\beta_j x_3 - ct)}, \\ (\sigma_{33}, \sigma_{13}, \sigma_{23}) &= \sum_{j=1}^{4} \left(D_{1j}, D_{2j}, D_{3j}\right) ikU_{1j} e^{ik(x_1+\beta_j x_3 - ct)}, \end{aligned} \quad (29)$$

where

$$\begin{aligned} D_{1j} &= C_{13} + C_{36}V_j + C_{33}\beta_j W_j, \\ D_{2j} &= C_{55}\left(\beta_j + W_j\right) + C_{45}\beta_j V_j, \\ D_{3j} &= C_{45}\left(\beta_j + W_j\right) + C_{44}\beta_j V_j, \\ V_j &= \frac{U_{2j}}{U_{1j}} = \frac{K_{11}K_{23} - K_{13}K_{12}}{K_{13}K_{22} - K_{12}K_{23}}, \\ W_j &= \frac{U_{3j}}{U_{1j}} = \frac{K_{11}K_{23} - K_{13}K_{12}}{K_{33}K_{22} - K_{13}K_{23}}. \end{aligned} \quad (30)$$

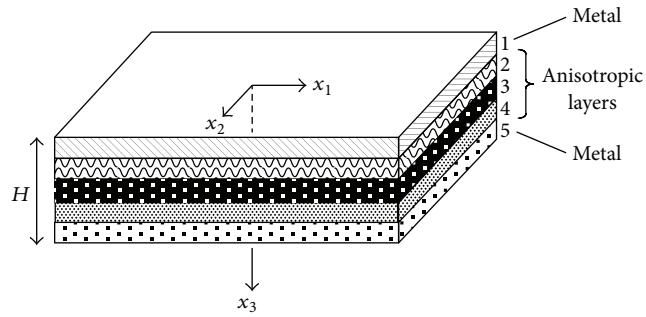

Figure 2: Multilayered plate.

Using (29) and (30) and after some simplifications, stress and displacement at $x_3 = 0$ may be related to those at $x_3 = x_3' = h$ (h is thickness of plate) by following the relation

$$\begin{aligned} &\left[u_1 \;\; u_2 \;\; u_3 \;\; \sigma_{33}^* \;\; \sigma_{13}^* \;\; \sigma_{23}^*\right]^t_{x_3'=h} \\ &\quad = [T]\left[u_1 \;\; u_2 \;\; u_3 \;\; \sigma_{33}^* \;\; \sigma_{13}^* \;\; \sigma_{23}^*\right]^t_{x_3'=0}, \\ &\sigma_{mn}^* = \frac{\sigma_{mn}}{ik}, \quad m, n = 1, 2, 3, \end{aligned} \quad (31)$$

where $[T]$is transfer matrix and is given by

$$\begin{aligned} [T] &= T_1 T_2 T_1^{-1}, \\ T_1 &= \begin{bmatrix} 1 & 1 & 1 & 1 & 1 & 1 \\ V_1 & V_1 & V_3 & V_3 & V_5 & V_5 \\ W_1 & -W_1 & W_3 & -W_3 & W_5 & -W_5 \\ D_{11} & D_{11} & D_{13} & D_{13} & D_{15} & D_{15} \\ D_{21} & -D_{21} & D_{23} & -D_{23} & D_{25} & -D_{25} \\ D_{31} & -D_{31} & D_{33} & -D_{33} & D_{35} & -D_{35} \end{bmatrix}, \\ T_2 &= \operatorname{diag}\left(e^{ik\beta_j h}\right), \quad j = 1, 2, \ldots, 6. \end{aligned} \quad (32)$$

By invoking free stress boundary conditions at lower and upper surfaces of plate, characteristic equation for single-layered plate may be obtained as follows:

$$\begin{vmatrix} T_{41} & T_{42} & T_{43} \\ T_{51} & T_{52} & T_{53} \\ T_{61} & T_{62} & T_{63} \end{vmatrix} = 0. \quad (33)$$

Substituting $k = \omega/c$ into (33) results in an equation with two unknown parameters ω and c.

Note 1. All of presented relations may be used for transversely isotropic, cubic, and isotropic materials, whereas (1a), (1b), and (1c)–(24) are enough for isotropic material because any arbitrary propagation direction coincides with one of the material symmetry axes!

Note 2. The presented procedure in Section 2.1.2 may be used for wave analysis in any direction of monoclinic plates.

2.2. Wave Propagation in a Multilayered Composite-Metal Plate. The above procedure for single-layered plate may

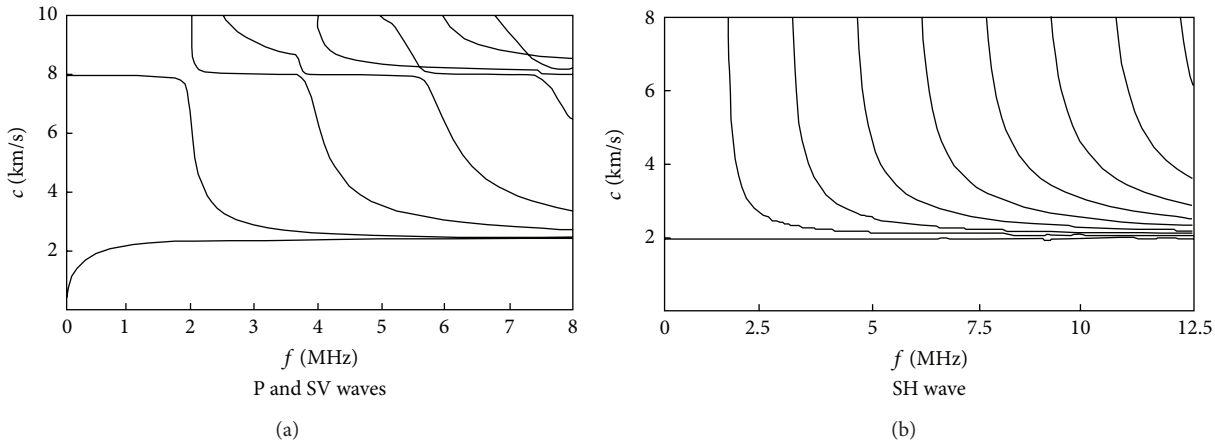

Figure 3: Wave propagation along principle-axes of a single-layered orthotropic plate.

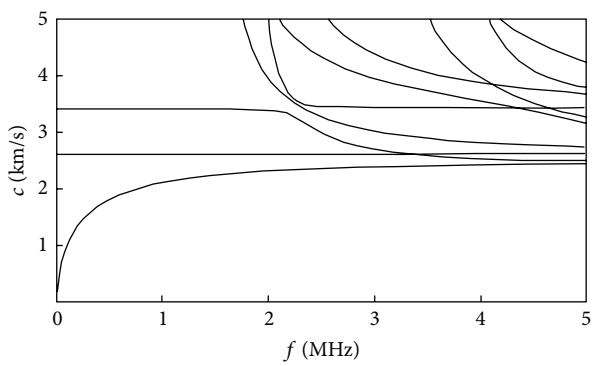

Figure 4: Wave propagation along off-principle-axes ($\varphi = 30^\circ$) of a single-layered orthotropic plate (SH, SV, and P waves).

be extended for a multilayered composite-metal plate (see Figure 2) by "transform matrix method." In this method by applying the continuity of the displacement and stress components at the layer interfaces of plate, displacements and stress components at lower surface can be related to those at upper one. For instance, in Figure 2, transfer matrix between $x_3 = 0$ and $x_3 = H$ is given by

$$T_{\text{Multi}} = T_{1m}T_{2a}T_{3a}T_{4a}T_{5m}, \tag{34}$$

where m and a refer to metal layer and anisotropic composite layer, respectively. By satisfying appropriate boundary condition on the outer boundaries, wave characteristic equations are obtained. It is noteworthy that a local coordinate system $(x_1', x_2', x_3')_p$ is considered for each layer p to obtain T_p using the presented equations in Section 2.1.

2.3. Dispersion Curves of Waves. Presented dispersion equations of waves in previous section such as (13), (24), and (33) may be used for plotting of dispersion curves of phase velocity c as function of frequency $f(= \omega/2\pi)$. These curves are important tools in damage detection techniques based on the wave propagation. However, the dispersion equations of waves do not generally have analytical solution and can be solved by numerical methods.

3. Numerical Examples

In this section, some numerical examples for calculation of dispersion curves in composite materials are presented in order to verify and validate the mentioned procedure. Two different cases are considered: wave propagation along principle- and off-principle-axes in (a) single-layered orthotropic plate and (b) two-layered composite-metal plate. We use MATLAB program to solve dispersion equation numerically. In the sequel, we elucidate each case study.

3.1. Dispersion Curves of Waves in Single-Layered Orthotropic Plate. In this subsection, dispersion curves of waves are plotted for a single-layered orthotropic plate with the following material properties: $\rho = 2\,\text{gr/cm}^3$, $h = 1\,\text{mm}$, $C_{11}' = 128, C_{12}' = 7, C_{13}' = 6, C_{22}' = 72, C_{23}' = 5, C_{33}' = 32, C_{44}' = 18, C_{55}' = 12.25, C_{66}' = 8, C_{11}' = 2\,(\text{GPa})$.

Two different cases are considered: (a) wave propagates along principle-axis x_1' in which (13) and (24) are used for SH wave and P and SV waves, respectively (see Figure 3); (b) wave propagates along off-principle-axis x_1 with angle $\varphi = 30^\circ$ with respect to x_1' in which (33) are used for SH, P, and SV waves as shown in Figure 4.

3.2. Dispersion Curves of Waves in Composite-Metal Plate. To verify the mentioned procedure in Section 2.2, we illustrate the wave dispersion curves in a double-layered plate including an orthotropic layer with the same material properties listed in Section 3.1 and an aluminum layer with the following material properties:

$$\begin{aligned} E &= 70\,\text{GPa}, \qquad \nu = 0.3, \\ \rho &= 2.7\,\text{gr/cm}^3, \qquad h = 1\,\text{mm}. \end{aligned} \tag{35}$$

In this situation, according to (34), transfer matrix is $= T_{\text{Al}}T_{\text{orth}}$, where T_{orth} and T_{Al} are calculated using (24) if

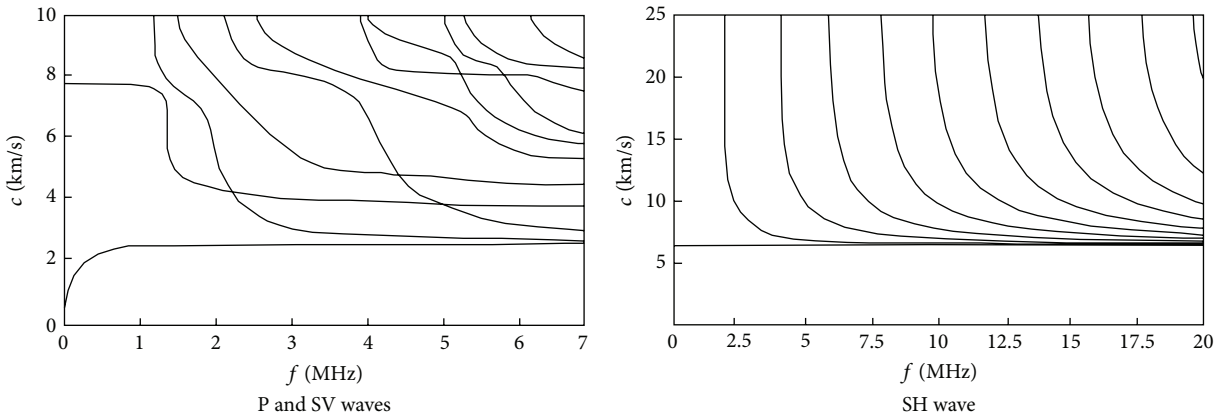

Figure 5: Wave propagation along principle-axes of a double-layered Al-orthotropic plate.

wave propagates along principle-axes of orthotropic layer. Dispersion curves of SH wave and P and SV waves are shown in Figure 5.

4. Conclusion

In this paper, wave dispersion relations of single anisotropic layer were presented. Two different cases were considered: propagation of wave along an axis of material symmetry and along off-axes of material symmetry. Since composite-metal structures have developed in last years, presented equations were extended for a multilayered composite-metal plate using the transfer matrix method. Suggested procedure is straightforward and applicable for damage detection based on wave propagation. However, the cost of calculations increases for large number of layers.

Conflict of Interests

The authors declare that there is no conflict of interests regarding the publication of this paper.

References

[1] V. Giurgiutiu, *Structural Health Monitoring with Piezoelectric Wafer Active Sensors*, Elsevier Academic Press, New York, NY, USA, 2008.

[2] V. Giurgiutiu, J. Bao, and W. Zhao, "Piezoelectric wafer active sensor embedded ultrasonics in beams and plates," *Experimental Mechanics*, vol. 43, no. 4, pp. 428–449, 2003.

[3] A. H. Nayfeh, "The general problem of elastic wave propagation in multilayered anisotropic media," *The Journal of the Acoustical Society of America*, vol. 89, no. 4, pp. 1521–1531, 1991.

[4] A. Demcenko and L. Mazeika, "Calculation of lamb waves dispersion curves in multi-layered planar structures," *Journal of Sound and Vibration*, vol. 329, no. 9, pp. 1435–1449, 2010.

[5] M. J. S. Lowe, "Matrix techniques for modeling ultrasonic waves in multilayered media," *IEEE Transactions on Ultrasonics, Ferroelectrics, and Frequency Control*, vol. 42, no. 4, pp. 525–542, 1995.

[6] K. L. Verma, "The general problem of thermoelastic wave propagation in multi-layered anisotropic media with application to periodic media," *International Journal of Applied Engineering*, vol. 1, no. 4, pp. 908–922, 2011.

Hindawi Publishing Corporation
Shock and Vibration
Volume 2014, Article ID 152145, 5 pages
http://dx.doi.org/10.1155/2014/152145

Research Article

Efficient Model Order Reduction of Structural Dynamic Systems with Local Nonlinearities under Periodic Motion

M. Mohammadali and H. Ahmadian

Center of Excellence in Experimental Solid Mechanics and Dynamics, School of Mechanical Engineering, Iran University of Science and Technology, Narmak, Tehran 16844, Iran

Correspondence should be addressed to M. Mohammadali; mohammadali@iust.ac.ir

Received 20 October 2012; Accepted 19 November 2012; Published 9 June 2014

Academic Editor: Hamid Mehdigholi

In many nonlinear structural systems, compared with the local regions with induced nonlinear effects, the main portions of the structures are linear. An exact condensation technique based on the harmonic balance method (HBM) in conjunction with the modal expansion technique is employed to convert the motion equations of such a system to a set of nonlinear algebraic equations that are considerably small and adequately accurate to determine periodic responses. To demonstrate the capability of the suggested method, few case studies consisting of discrete systems with weak and essential nonlinearities are studied, and the results are compared to other methodologies results.

1. Introduction

Compared with the local regions with induced nonlinear effects, the main portions of the structural systems are linear. Typical engineering examples of these localized nonlinear sources are friction and vibroimpact in joints, local buckling, crack, nonlinear isolator, dead zone (gap), and squeeze film dampers in mechanical systems. Consequently, the dynamic response of such a system is nonlinear. A dynamic model for this structural system is useful for detailed study, prediction of response, identification of unknown parameters, or health monitoring of the overall system. Therefore, much time and effort are consumed in the development of this dynamic model that includes desired effects. Usually, the dynamic properties of the structure components are known (analysed or tested) as separate components, and they are used for development of the dynamic model for the total assembled system.

Any nonlinear response analysis involves significant computational effort, especially if the full dynamic model is used and a set of performance characteristics related to temperature, preload, deflection, and so forth characterize the nonlinear elements. Although there is significant motivation to develop a set of model order reduction (MOR) techniques to project the system model to a condensed space and considerably reduce time of nonlinear response computation, accuracy of these MOR techniques and solution algorithms are still issues. For reduction of nonlinear discrete models one can apply linear MOR techniques [1] such as Guyan reduction [2, 3], improved reduced system (IRS) [4], iterated improved reduced system (IIRS) [5], system equivalent reduction expansion process (SEREP), [6] or component mode synthesis (CMS) [4, 7].

Other reduction methods that can be applied to reduce continuous and discrete models size are commonly used linear normal modes (LNMs) of linearized system and nonlinear normal modes (NNMs). Generation of NNMs for a small system requires considerable effort [8, 9], especially in the presence of internal resonance [10] and/or external excitation [11]. In the case of a large system, it is possible to use other reduction techniques and then generate NNMs of the reduced order model [12].

Reduction techniques based on linear MOR techniques, in best, will lead to an acceptable answer for weakly nonlinear system, and by growing the nonlinearity their accuracy will be lost due to their linear nature. Local equivalent linear stiffness method (LELMS) was proposed [13] to reduce the nonlinear discrete models size. In this method, an equivalent linear

system of the nonlinear system is iteratively calculated whose mode shapes are used to reduce the system size.

There are many different algorithms for solving nonlinear systems. A semianalytical method that is generally valid over a much larger domain compared to the other methodologies is the harmonic balance method (HBM) [14]. The HBM can solve many types of nonlinear problems in the form of periodic response. The HBM is used for handling nonlinear problems consisting of forced excited, strongly nonlinear response, chaotic behaviour, and internal resonance and has a great potential for identification and health monitoring. Furthermore, this technique is applied to estimate NNMs of nonlinear systems [8]. HBM expands the periodic response of the nonlinear system in the form of truncated Fourier series, whose coefficients are estimated by solving a set of nonlinear algebraic equations. In the absence of internal resonance in many cases, the solution of one term harmonic balance has good correlation with the recorded experimental results [15]. Typically, more accurate approximation to the solution obtained by using a Fourier series with a higher number of terms and, in general, the amplitudes of the higher terms gradually decrease. Consequently, in experiment if the higher term's amplitudes are small, then inclusion of measurement noise will result in the difference between these terms in the analysis and experiment.

HBM is improved in different ways because of its capability. Incremental harmonic balance (IHB) [16] suggests a new formulation based on HBM for achieving frequency responses of nonlinear systems. With the aim of reducing the computational cost and preserving the accuracy, adaptive HBM (AHBM) [17] has proposed selection algorithms for the number of Fourier series terms. Recently, a new exact reduction technique [18, 19] was proposed for discrete systems that condense the problem into the nonlinear DOFs only.

The aim of this work is to study the technique suggested by KIM [18, 19] and extend this by expanding the nonlinear DOFs motions by natural modes of the condensed system. To demonstrate the capability of the suggested method, few case studies consisting of a discrete system with weak and essential nonlinearity are studied and the results are compared.

2. Formulation

The general form of a nonlinear dynamic system with N degrees of freedom (DOFs) is shown below:

$$\mathbf{M}\ddot{\mathbf{q}} + \mathbf{C}\dot{\mathbf{q}} + \mathbf{K}\mathbf{q} + \mathbf{f}_{\mathrm{nl}} = \mathbf{f}_E, \tag{1}$$

where $\mathbf{q}$ is the field deformation vector, $\mathbf{M}$, $\mathbf{C}$, and $\mathbf{K}$ are mass, damping, and stiffness matrices, $\mathbf{f}_{\mathrm{nl}}$ is nonlinear force, and $\mathbf{f}_E$ is periodic excitation force. $\mathbf{q}$, $\mathbf{f}_{\mathrm{nl}}$, and $\mathbf{f}_E$ are function of time which time argument, t, is dropped for convenience. If the steady-state solution of above equation with the period of $T = 2\pi/\omega$ is requested, the deformation field can be expanded with the aid of HBM in the form of

$$\mathbf{q} = \sum_{j=0}^{m} \left(\boldsymbol{\psi}_j \cos(j\omega t) + \boldsymbol{\varphi}_j \sin(j\omega t)\right), \tag{2}$$

where $\boldsymbol{\psi}_j$ and $\boldsymbol{\varphi}_j$ are vectors of vibration amplitude at the frequency of $j\omega$. By substituting (2) into (1) and using Galerkin method, the equation of motion is decoupled in the form below:

$$\begin{gathered}
-j^2\omega^2\mathbf{M}\boldsymbol{\psi}_j + j\omega\mathbf{C}\boldsymbol{\varphi}_j + \mathbf{K}\boldsymbol{\psi}_j + \mathbf{f}_{\mathrm{nl},c_j} = \mathbf{f}_{E,c_j}, \\
-j^2\omega^2\mathbf{M}\boldsymbol{\varphi}_j - j\omega\mathbf{C}\boldsymbol{\psi}_j + \mathbf{K}\boldsymbol{\varphi}_j + \mathbf{f}_{\mathrm{nl},s_j} = \mathbf{f}_{E,s_j}, \\
j = 0, 1, 2, \ldots, m, \\
\left\{\mathbf{f}_{X,c_j}, \mathbf{f}_{X,s_j}\right\} = (1 + \operatorname{sgn}(j)) \\
\times \frac{\omega}{2\pi}\int_0^{2\pi/\omega} \left\{\mathbf{f}_X \cos(j\omega t), \mathbf{f}_X \sin(j\omega t)\right\} dt,
\end{gathered} \tag{3}$$

where X is replaced by arbitrary subscripts of force vectors. Equation (3) expresses one static equilibrium and $2m$ dynamic equations. By using imaginary unit $\imath = \sqrt{-1}$, (3) can be put together in the form

$$\begin{gathered}
\left(-j^2\omega^2\mathbf{M} - \imath j\omega\mathbf{C} + \mathbf{K}\right)\boldsymbol{\chi}_j + \mathbf{f}_{\mathrm{nl}\,j} = \mathbf{f}_{E\,j} \\
j = 0, 1, 2, \ldots, m,
\end{gathered} \tag{4}$$

where

$$\begin{gathered}
\boldsymbol{\chi}_j = \boldsymbol{\psi}_j + \imath\boldsymbol{\varphi}_j, \\
\mathbf{f}_{X\,j} = \mathbf{f}_{X,c_j} + \imath\mathbf{f}_{X,s_j}.
\end{gathered} \tag{5}$$

In the case of localized nonlinearity, it is possible to write nonlinear force vector in the form

$$\begin{gathered}
\mathbf{f}_{\mathrm{nl}}^T = \left\{f_{\mathrm{nl}1}, \ldots, f_{\mathrm{nl}p}, 0, 0, \ldots, 0\right\}, \\
\mathbf{f}_{\mathrm{nl}} = \begin{Bmatrix} \mathbf{f}_{\mathrm{nl}_\alpha} \\ \mathbf{0} \end{Bmatrix}.
\end{gathered} \tag{6}$$

Furthermore, the deformation field can be divided into two vectors with subscripts α and β, which stand for active or master coordinates and deleted or slave coordinates, respectively. Active coordinates are experiencing nonlinear forces and deleted coordinates are only subjected to linear forces. Also, $\mathbf{f}_E$ vector and $\mathbf{M}$, $\mathbf{C}$, and $\mathbf{K}$ matrices can be divided appropriately with subscripts α and β. Therefore, the motion equation in (4) can be written in the form

$$\begin{gathered}
\left(-j^2\omega^2\begin{bmatrix} \mathbf{M}_{\alpha\alpha} & \mathbf{M}_{\alpha\beta} \\ \mathbf{M}_{\beta\alpha} & \mathbf{M}_{\beta\beta} \end{bmatrix} - \imath j\omega\begin{bmatrix} \mathbf{C}_{\alpha\alpha} & \mathbf{C}_{\alpha\beta} \\ \mathbf{C}_{\beta\alpha} & \mathbf{C}_{\beta\beta} \end{bmatrix}\right. \\
\left. + \begin{bmatrix} \mathbf{K}_{\alpha\alpha} & \mathbf{K}_{\alpha\beta} \\ \mathbf{K}_{\beta\alpha} & \mathbf{K}_{\beta\beta} \end{bmatrix}\right)\begin{Bmatrix} \boldsymbol{\chi}_{\alpha_j} \\ \boldsymbol{\chi}_{\beta_j} \end{Bmatrix} + \begin{Bmatrix} \mathbf{f}_{\mathrm{nl}_\alpha} \\ \mathbf{0} \end{Bmatrix} \\
= \begin{Bmatrix} \mathbf{f}_{E_\alpha} \\ \mathbf{f}_{E_\beta} \end{Bmatrix}, \quad j = 0, 1, 2, \ldots, m.
\end{gathered} \tag{7}$$

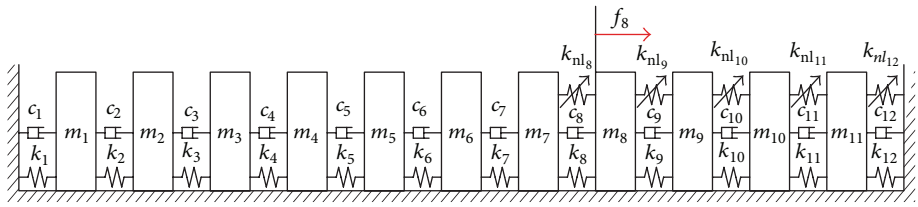

Figure 1: The discrete system model.

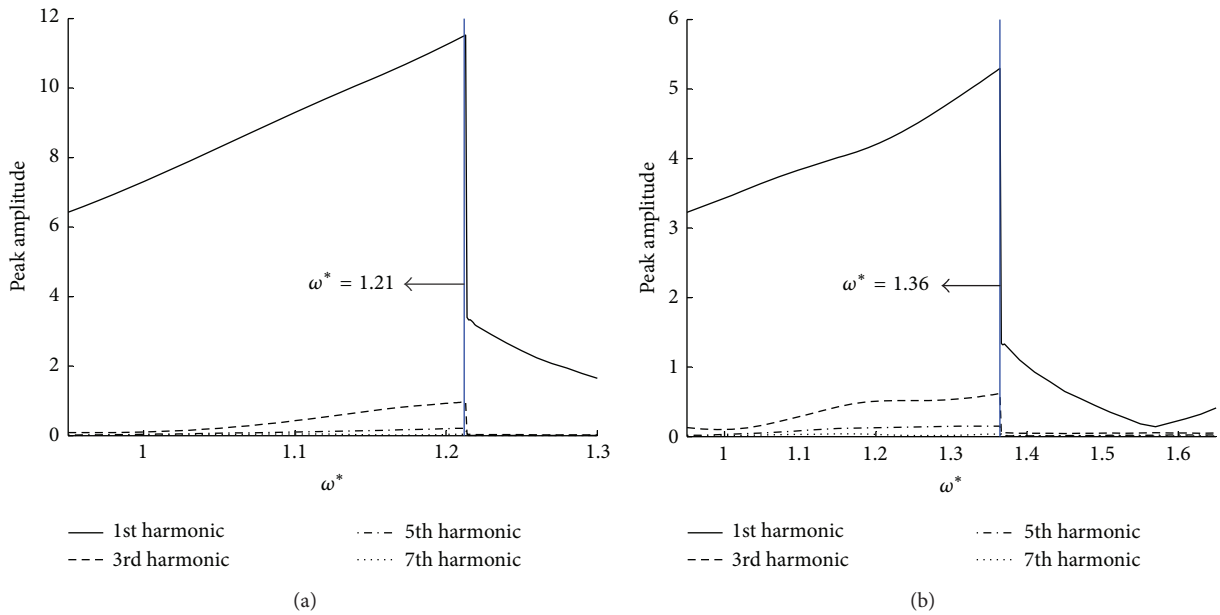

Figure 2: The response peak amplitudes of each harmonic at 8th DOF: (a) weakly nonlinear system; (b) essentially nonlinear system.

In above equation, one can eliminate $\boldsymbol{\chi}_{\beta_j}$ from the first row with the aid of the second row; this will result in exact reduced form of motion equation

$$\begin{aligned}
&\left(-j^2\omega^2\ \mathbf{M}_{\alpha\alpha}-\imath j\omega\mathbf{C}_{\alpha\alpha}+\mathbf{K}_{\alpha\alpha}-\mathbf{K}_{Mj}\right)\boldsymbol{\chi}_{\alpha_j}+\mathbf{f}_{\mathrm{nl}_{\alpha j}}\\
&\quad=\mathbf{f}_{E_{\alpha_j}}-\mathbf{f}_{ET_{\beta_j}},\\
&\mathbf{A}_j=\left(-j^2\omega^2\mathbf{M}_{\alpha\beta}-\imath j\omega\mathbf{C}_{\alpha\beta}+\mathbf{K}_{\alpha\beta}\right)\\
&\qquad\times\left(-j^2\omega^2\mathbf{M}_{\beta\beta}-\imath j\omega\mathbf{C}_{\beta\beta}+\mathbf{K}_{\beta\beta}\right)^{-1}\\
&\mathbf{K}_{Mj}=\mathbf{A}_j\left(-j^2\omega^2\mathbf{M}_{\beta\alpha}-\imath j\omega\mathbf{C}_{\beta\alpha}+\mathbf{K}_{\beta\alpha}\right),\\
&\qquad\mathbf{f}_{ET_{\beta_j}}=\mathbf{A}_j\mathbf{f}_{E_{\beta_j}}.
\end{aligned}\tag{8}$$

The deformation field vectors, $\boldsymbol{\chi}_{\alpha_j}$, can be expanded by one of its basis. Orthogonal bases which consist of arranged vectors with minimum energy required for excitation will be suitable bases to approximate the deformation field vectors and reduce the size of condense system. To find such bases, $\mathbf{K}_{Mj}$ can be considered as a constant stiffness matrix, whose dependence on frequency, $j\omega$, is neglected; then

$$\left(-\lambda_{jk}^2\ \mathbf{M}_{\alpha\alpha}-\imath\lambda_{jk}\mathbf{C}_{\alpha\alpha}+\mathbf{K}_{\alpha\alpha}-\mathbf{K}_{Mj}\right)\boldsymbol{\phi}_{jk}=\mathbf{0}\tag{9}$$

is the eigenvalue problem of the linearized condensed system, where $\boldsymbol{\phi}_{jk}$ is the kth mass normalized, maximum real right eigenvector and λ_{jk} is its companion eigenvalue. The $\boldsymbol{\phi}_{jk}$ are orthogonal basis of $\boldsymbol{\chi}_{\alpha_j}$ and by increasing the k index the required energy for excitation $\boldsymbol{\phi}_{jk}$ in linearized condensed system will grow. Considering that the motion of the nonlinear condensed system is close to linearized system, the deformation field in (8) can be approximated by few vectors of these orthogonal bases. Therefore, the deformation field can be written in the form

$$\boldsymbol{\chi}_{\alpha_j}\cong\boldsymbol{\Phi}_j\left(\boldsymbol{\eta}_{c_j}+\imath\boldsymbol{\eta}_{s_j}\right),\tag{10}$$

where $\boldsymbol{\eta}_{c_j}$ and $\boldsymbol{\eta}_{s_j}$ are unknown real vectors and $\boldsymbol{\Phi}_j$ is the modal matrix in which collaborated mode shapes, $\boldsymbol{\phi}_{jk}$, are arranged in column fashion. After substituting (10) into (8)

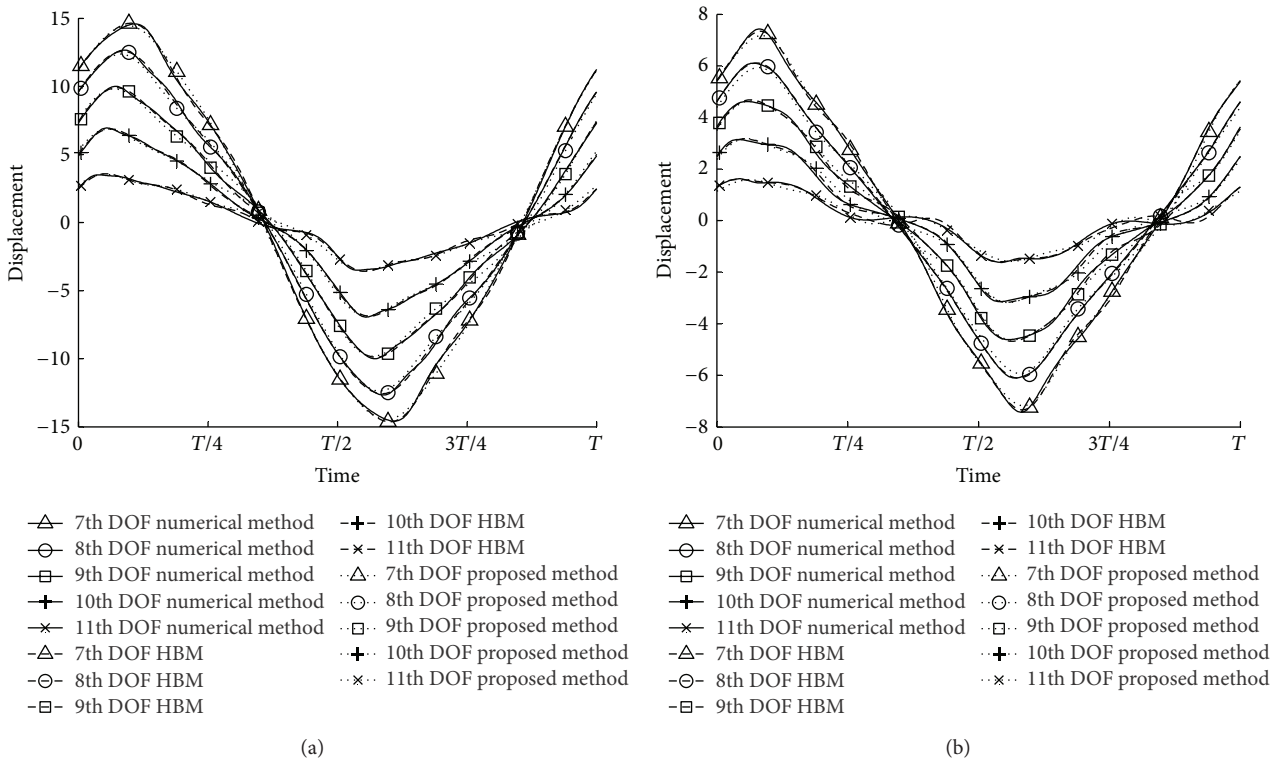

Figure 3: Time response of nonlinear systems at their resonance: (a) weakly nonlinear system $\omega^* = 1.21$; (b) essentially nonlinear system $\omega^* = 1.36$.

and using Galerkin method the motion equation will become in the form

$$\begin{gathered}\mathbf{\Theta}_j\left(\boldsymbol{\eta}_{c_j}+\imath\boldsymbol{\eta}_{s_j}\right)+\left\langle \mathbf{f}_{\mathrm{nl}_{\alpha j}},\mathbf{\Phi}_j\right\rangle=\left\langle \mathbf{f}_{E_{\alpha j}}-\mathbf{f}_{ET_{\beta_j}},\mathbf{\Phi}_j\right\rangle,\\ \mathbf{\Theta}_j=\left\langle\left(-j^2\omega^2\mathbf{M}_{\alpha\alpha}-\imath j\omega\mathbf{C}_{\alpha\alpha}+\mathbf{K}_{\alpha\alpha}-\mathbf{K}_{Mj}\right)\mathbf{\Phi}_j,\mathbf{\Phi}_j\right\rangle,\\ \langle\mathbf{a},\mathbf{b}\rangle=\mathbf{ba},\end{gathered}\tag{11}$$

where $*$ is transpose operator. The real and imaginary part of above equation will result in two different nonlinear equations. Therefore,

$$\begin{gathered}\begin{bmatrix}\mathrm{Re}\left(\mathbf{\Theta}_j\right) & -\mathrm{Im}\left(\mathbf{\Theta}_j\right)\\ \mathrm{Im}\left(\mathbf{\Theta}_j\right) & \mathrm{Re}\left(\mathbf{\Theta}_j\right)\end{bmatrix}\begin{Bmatrix}\boldsymbol{\eta}_{c_j}\\ \boldsymbol{\eta}_{s_j}\end{Bmatrix}+\begin{Bmatrix}\mathrm{Re}\left(\left\langle \mathbf{f}_{\mathrm{nl}_{\alpha_j}},\mathbf{\Phi}_j\right\rangle\right)\\ \mathrm{Im}\left(\left\langle \mathbf{f}_{\mathrm{nl}_{\alpha_j}},\mathbf{\Phi}_j\right\rangle\right)\end{Bmatrix}\\ =\begin{Bmatrix}\mathrm{Re}\left(\left\langle \mathbf{f}_{E_{\alpha_j}}-\mathbf{f}_{ET_{\beta_j}},\mathbf{\Phi}_j\right\rangle\right)\\ \mathrm{Im}\left(\left\langle \mathbf{f}_{E_{\alpha_j}}-\mathbf{f}_{ET_{\beta_j}},\mathbf{\Phi}_j\right\rangle\right)\end{Bmatrix}.\end{gathered}\tag{12}$$

By solving (12) with an arbitrary method the final solution of motion will be achieved.

3. Numerical Results

In what follows, to prove the power of the proposed reduction technique discrete vibrating systems are studied with weak and essential nonlinearities of the cubic form. These systems have 11 DOFs in which 5 of its DOFs are connected together with nonlinear stiffness (Figure 1).

The steady-state responses of the system under periodic excitation are determined by the numerical method, HBM, and proposed method. The resultant nonlinear algebraic equations of HBM and proposed method are solved by Newton-Raphson algorithm. The computational complexity of this method at each step can be approximated by the square of the number of equations.

The motion of these systems is governed by

$$\begin{gathered}m\ddot{x}_i+c\left(2\dot{x}_i-\dot{x}_{i+1}-\dot{x}_{i-1}\right)+k\left(2x_i-x_{i+1}-x_{i-1}\right)\\ +k_{\mathrm{nl}i}\left(x_i-x_{i-1}\right)^3+k_{\mathrm{nl}i+1}\left(x_i-x_{i+1}\right)^3=f_i,\end{gathered}\tag{13}$$

where $i=1,2,\ldots,11$, $m=1$, $c=1/10$, $k=1$, and

$$f_i=\begin{cases}0 & i\neq 8\\ \cos(\omega t) & i=8.\end{cases}\tag{14}$$

For the case of weak and essential nonlinearities $k_{\mathrm{nl}i}$ is taken as

$$\begin{cases}0 & i<7\\ \dfrac{1}{5} & i\geq 7,\end{cases}\qquad\begin{cases}0 & i<7\\ 2 & i\geq 7,\end{cases}\tag{15}$$

respectively. $\omega_1 = 0.26$ Hz, real part of the first resonance frequency of linearized system, is used to normalize the excitation frequency $\omega^* = \omega/\omega_1$. Peak amplitudes of each

harmonic at 8th DOF are shown in Figure 2 for different frequencies.

The steady-state responses of the systems at their resonances are approximated by first 7 harmonies.

The nonlinear systems with 11 DOFs are reduced to 5 master DOFs and solved using HBM, which causes around 80% decrease in computational cost. By applying the proposed method to the condensed system and expanding the response using its first three mode shapes, another 64% computational cost reduction is achieved due to reduction of systems size from 5 DOFs to 3 DOFs. The results are shown in Figure 3.

In both cases, there are negligible differences between numerical method and the HBM due to harmonic truncation order; therefore, this error is present in the proposed method results.

Compared to the results of the HBM and numerical method, phase of the DOFs vibration computed by the proposed method is accurate in both nonlinear systems. However, the difference between the calculated amplitudes with the proposed and other methods is increased with growing the nonlinearity, but the captured response is still acceptable. These differences are due to reduction of exact condensed system size, from 5 DOFs to 3 DOFs, which leads to a stiffer system.

4. Conclusion

In this paper, a new condensation technique is suggested for discrete systems by the combination of exact condensation techniques based on HBM and modal expansion technique to reduce the computational cost and preserve the accuracy. The proposed method is used to reduce the size of two nonlinear systems with weak and essential nonlinearity. At last, the predicted periodic responses are compared with other methodologies results. The correlation between the results of the proposed method and other techniques is appropriate. Using the suggested technique, the reduced form of the system is independent of system nonlinearities; therefore, this technique has a great potential for the identification of system nonlinearities. The main drawback of the suggested technique is its frequency dependency.

Conflict of Interests

The authors declare that there is no conflict of interests regarding the publication of this paper.

References

[1] Z. Qu, *Model Order Reduction Techniques*, 2004.

[2] R. J. Guyan, "Reduction of stiffness and mass matrices," *AIAA Journal*, vol. 3, no. 2, pp. 380–380, 1965.

[3] R. W. Stephenson and K. W. Rouch, "Modeling rotating shafts using axisymmetric solid finite elements with matrix reduction," *Journal of Vibration and Acoustics, Transactions of the ASME*, vol. 115, no. 4, pp. 484–489, 1993.

[4] M. I. Friswell, J. E. T. Penny, and S. D. Garvey, "Using linear model reduction to investigate the dynamics of structures with local non-linearities," *Mechanical Systems and Signal Processing*, vol. 9, no. 3, pp. 317–328, 1995.

[5] M. I. Friswell, S. D. Garvey, and J. E. T. Penny, "Model reduction using dynamic and iterated IRS techniques," *Journal of Sound and Vibration*, vol. 186, no. 2, pp. 311–323, 1995.

[6] J. O'Callahan, P. Avitabile, and R. Riemer, "System equivalent reduction expansion process (SEREP)," Tech. Rep., IMAC, 1989.

[7] M. C. C. Bampton and R. R. Craig, "Coupling of substructures for dynamic analyses," *AIAA Journal*, vol. 6, no. 7, pp. 1313–1319, 1968.

[8] G. Kerschen, M. Peeters, J. C. Golinval, and A. F. Vakakis, "Nonlinear normal modes, Part I: a useful framework for the structural dynamicist," *Mechanical Systems and Signal Processing*, vol. 23, no. 1, pp. 170–194, 2009.

[9] M. Peeters, R. Viguié, G. Sérandour, G. Kerschen, and J.-C. Golinval, "Nonlinear normal modes, Part II: toward a practical computation using numerical continuation techniques," *Mechanical Systems and Signal Processing*, vol. 23, no. 1, pp. 195–216, 2009.

[10] D. Jiang, C. Pierre, and S. W. Shaw, "The construction of nonlinear normal modes for systems with internal resonance," *International Journal of Non-Linear Mechanics*, vol. 40, no. 5, pp. 729–746, 2005.

[11] D. Jiang, C. Pierre, and S. W. Shaw, "Nonlinear normal modes for vibratory systems under harmonic excitation," *Journal of Sound and Vibration*, vol. 288, no. 4-5, pp. 791–812, 2005.

[12] M. Legrand, D. Jiang, C. Pierre, and S. Shaw, "Nonlinear normal modes of a rotating shaft based on the invariant manifold method," *The International Journal of Rotating Machinery*, vol. 10, no. 4, pp. 319–335, 2004.

[13] E. A. Butcher, "Clearance effects on bilinear normal mode frequencies," *Journal of Sound and Vibration*, vol. 224, no. 2, pp. 305–328, 1999.

[14] M. Peeters, G. Kerschen, and J. C. Golinval, "Dynamic testing of nonlinear vibrating structures using nonlinear normal modes," *Journal of Sound and Vibration*, vol. 330, no. 3, pp. 486–509, 2011.

[15] T. A. Doughty, P. Davies, and A. K. Bajaj, "A comparison of three techniques using steady state data to identify non-linear modal behavior of an externally excited cantilever beam," *Journal of Sound and Vibration*, vol. 249, no. 4, pp. 785–813, 2002.

[16] A. Grolet and F. Thouverez, "On a new harmonic selection technique for harmonic balance method," *Mechanical Systems and Signal Processing*, vol. 30, pp. 43–60, 2012.

[17] Y. B. Kim and S. T. Noah, "Response and bifurcation analysis of a MDOF rotor system with a strong nonlinearity," *Nonlinear Dynamics*, vol. 2, no. 3, pp. 215–234, 1991.

[18] Y. B. Kim and S. T. Noah, "Stability and bifurcation analysis of oscillators with piecewise-linear characteristics. A general approach," *Journal of Applied Mechanics, Transactions ASME*, vol. 58, no. 2, pp. 545–553, 1991.

[19] S. L. Lau and Y. K. Cheung, "Amplitude incremental variational principle for nonlinear vibration of elastic systems," *Journal of Applied Mechanics*, vol. 48, no. 4, pp. 959–964, 1981.

Hindawi Publishing Corporation
Shock and Vibration
Volume 2014, Article ID 809739, 8 pages
http://dx.doi.org/10.1155/2014/809739

Research Article

Bifurcation and Chaos Prediction in Nonlinear Gear Systems

Anooshirvan Farshidianfar and Amin Saghafi

Mechanical Engineering Department, Ferdowsi University of Mashhad, Mashhad, Iran

Correspondence should be addressed to Amin Saghafi; a.i.saghafi@gmail.com

Received 18 October 2012; Accepted 19 November 2012; Published 28 May 2014

Academic Editor: Abdolreza Ohadi

The homoclinic bifurcation and transition to chaos in gear systems are studied both analytically and numerically. Applying Melnikov analytical method, the threshold values for the occurrence of chaotic motion are obtained. The influence of system parameters on the character of vibration is studied. The numerical simulation of the system including bifurcation diagram, phase plane portraits, Fourier spectra, and time histories is considered to confirm the analytical predictions for the occurrence of homoclinic bifurcation and chaos in nonlinear gear systems.

1. Introduction

Gear systems are known as one of the important sources of noise and vibration in industrial rotating machinery and power transmission systems. With the development of nonlinear dynamics, the nonlinear characteristics in gear systems, such as stability, periodic responses, bifurcations, and chaotic behaviors, have become the most interesting research areas. For instance, Sato et al. [1] established a nonlinear model of gear system with the time dependence of tooth stiffness and backlash. They investigated the bifurcation and chaotic phenomena by using a shooting method. Padmanabhan and Singh [2] analyzed a 2-d.o.f system with clearance nonlinearity. They used a numerical simulation to demonstrate the existence of periodic and chaotic behaviors. Kahraman and Blankenship [3] performed experiments on a spur gear pair and observed various nonlinear phenomena including period doubling and chaos. Theodossiades and Natsiavas [4] investigated the motor-driven gear-pair systems and found periodic and chaotic behaviors in this system. Also, Chang-Jian and Chang [5] investigated the dynamic responses of a single-degree-of freedom spur gear system with and without nonlinear suspension and found the bifurcation and chaotic dynamics in this system.

From the above-mentioned references, one finds that chaotic phenomena have been found in nonlinear gear systems. Analytical [2], numerical [1, 4, 5], and experimental methods [3] were used by different authors to study chaos for spur gear systems. Due to the complexity of the gear systems and also the difficulty and limitation of the analytical methods, the numerical method was commonly used to analyze the nonlinear dynamics in gear systems, but they cannot provide any analytical expression of the solutions. Although significant amount of research has been devoted to nonlinear gear dynamic, few attempts have been made to investigate analytical solution of the system. Melnikov analysis is one of the few analytical methods to provide an approximate criterion for the occurrence of hetero/homoclinic bifurcation and chaos in nonlinear systems. According to this theory, the existence of transversal intersection of stable and unstable manifolds of saddle fixed points implies the occurrence of the chaos [6–8]. Thus, the current paper focuses on the study of the homoclinic bifurcation and chaos for the gear system by means of Melnikov analysis.

The organization of the paper is as follows. In Section 2, a model for the vibration of gear transmission system is presented. In Section 3, the conditions for chaotic behaviour in terms of homoclinic bifurcation are given by using Melnikov analysis. Finally, in Section 4, the threshold values for the occurrence of chaotic motion are obtained. Some numerical simulation of the system including bifurcation diagrams, plane phase portraits, Fourier spectra, and time histories is used to confirm the analytical predictions and show the transition to chaotic motion.

2. Problem Formulation

The mechanical model of a spur gear pair system investigated in the present study is shown in Figure 1(a). In this model, the gear mesh is modeled as a pair of rigid disks connected by a spring damper set along the line of action. The backlash function is usually used to represent gear clearances. Under these assumptions, the equations of motion can be expressed as

$$I_a \frac{d^2\theta_a}{d\bar{t}^2} + c\left(r_a \frac{d\theta_a}{d\bar{t}} - r_b \frac{d\theta_b}{d\bar{t}}\right) r_a + r_a K h\left(r_a\theta_a - r_b\theta_b\right) = T_a, \tag{1a}$$

$$I_b \frac{d^2\theta_b}{d\bar{t}^2} - c\left(r_a \frac{d\theta_a}{d\bar{t}} - r_b \frac{d\theta_b}{d\bar{t}}\right) r_b - r_b K h\left(r_a\theta_a - r_b\theta_b\right) = -T_b. \tag{1b}$$

In these equations, θ_a and θ_b are the torsional displacements of gears (a) and (b). I_a and I_b are the mass moments of inertia and r_a and r_b are the base circle radius of the gears. K and c represent the stiffness and linear viscous damping of the gear mesh. T_a and T_b are external torques acting on the driver and driven gear, respectively. An input torque T_a is applied to the driver gear (a) rotating at Ω_a and the mean braking torque T_b on the driven gear with angular velocity Ω_b. The excitation torque T_a fluctuates significantly between low and high values. Therefore, the T_a can be decomposed into average torque transmitted through the gear pair T_{ma} and the fluctuating external torque excitation $T_p(\bar{t})$ parts. Such excitations are typically at low frequencies Ω which are the first few multiples of the input shaft frequency. Also, output torque fluctuation will be neglected; that is, $T_b(\bar{t}) = T_{mb}$. Express T_a via Fourier series as [9]

$$T_a\left(\bar{t}\right) = T_{ma} + \sum_{r=1}^{\infty} T_{pr} \cos\left(r\Omega\bar{t} + \varphi_r\right). \tag{2}$$

So, (1a) and (1b) are simplified into (3) by introducing a new variable $\bar{x} = r_a\theta_a - r_b\theta_b$:

$$m\ddot{\bar{x}} + c\dot{\bar{x}} + kh\left(\bar{x}\right) = \bar{F}_m + \sum_{r=1}^{\infty} \bar{F}_{pr} \cos\left(r\Omega\bar{t} + \varphi_r\right) \tag{3}$$

with

$$h\left(\bar{x}\right) = \begin{cases} \bar{x} - (1-\alpha)\, d & d < \bar{x} \\ \alpha\bar{x} & -d \le \bar{x} \le d, \\ \bar{x} + (1-\alpha)\, d & d < -\bar{x} \end{cases}$$
$$m = \frac{I_a I_b}{I_b r_a^2 + I_a r_b^2}, \qquad \bar{F}_{pr} = m\left(\frac{r_a}{I_a}\right) T_{pr}, \tag{4}$$
$$\bar{F}_m = m\left(\frac{T_{ma} r_a}{I_a} + \frac{T_{mb} r_b}{I_b}\right),$$

Here m is the equivalent mass representing the total inertia of the gear pair, $\bar{F}_m$ is the average force transmitted through the gear pair, and $\bar{F}_p(\bar{t})$ is the fluctuating force related to the input torque excitation. $2d$ represent the backlash. $h(\bar{x})$ is the nonlinear displacement function due to backlash. It is a stepwise linear function. A nondimensional form of the above equation is obtained by letting

$$\Omega_n = \sqrt{\frac{k}{m}}, \qquad t = \Omega_n \bar{t}, \qquad x = \frac{\bar{x}}{d_c}, \qquad \hat{\mu} = \frac{c}{m\Omega_n},$$
$$\hat{F}_m = \frac{\bar{F}_m}{d_c k}, \qquad \hat{F}_{pr} = \frac{\bar{F}_{pr}}{d_c k}, \qquad \omega = \frac{\Omega}{\Omega_n}, \tag{5}$$

where d_c is characteristic length. By choosing the parameters $\alpha = 0$ and $d/d_c = 0.1745$ [9], the function $h(x)$ is approximated with a third-order polynomial as $h(x) = -0.1422x + 5.8093x^3$ (Figure 1(b)). Substituting $h(x)$, the nondimensional form of (3) could be rewritten as

$$\ddot{x} + \hat{\mu}\dot{x} + \left(-0.1422x + 5.8093x^3\right) = \hat{F}_m + \sum_{r=1}^{\infty} \hat{F}_{pr} \cos\left(\omega t + \varphi_r\right). \tag{6}$$

This equation considers the effect of backlash and so it is the equation which would be studied in this paper.

3. Global Bifurcation and Chaos in Gear Model

The study of homoclinic bifurcation that enables predicting the chaotic behaviors of nonlinear systems is well done by the Melnikov theory. The Melnikov method is one of the few analytical methods to study the global bifurcation of the system and gives a procedure for analyzing and estimating when a chaotic behavior of a nonlinear system is expected. According to this theory, the existence of transversal intersection of stable and unstable manifolds of homoclinic orbits implies the existence of the chaotic dynamic. In order to apply this technique and to carry out this study, the average force, the excitation term, and the damping are considered as small perturbations for the Hamiltonian system. Scaling $\hat{\mu} = \varepsilon\mu$, $\hat{F}_m = \varepsilon f_m$, and $\hat{F}_{pr} = \varepsilon f_{pr}$, (6) can be rewritten as

$$\dot{x} = y,$$
$$\dot{y} = -\varepsilon\mu\dot{x} + \left(0.1422x - 5.8093x^3\right) + \varepsilon\left(f_m + \sum_{r=1}^{\infty} f_{pr} \cos\left(\omega t + \varphi_r\right)\right), \tag{7}$$

where ε is a small parameter so that the damping, forcing, and excitation terms are perturbations to the unperturbed system.

3.1. Analysis of the Unperturbed Model. In this subsection, the homoclinic orbits of the unperturbed system are derived. For the unperturbed system, when $\varepsilon = 0$, (7) is simplified to

$$\dot{x} = y, \qquad \dot{y} = \left(bx - cx^3\right), \tag{8}$$

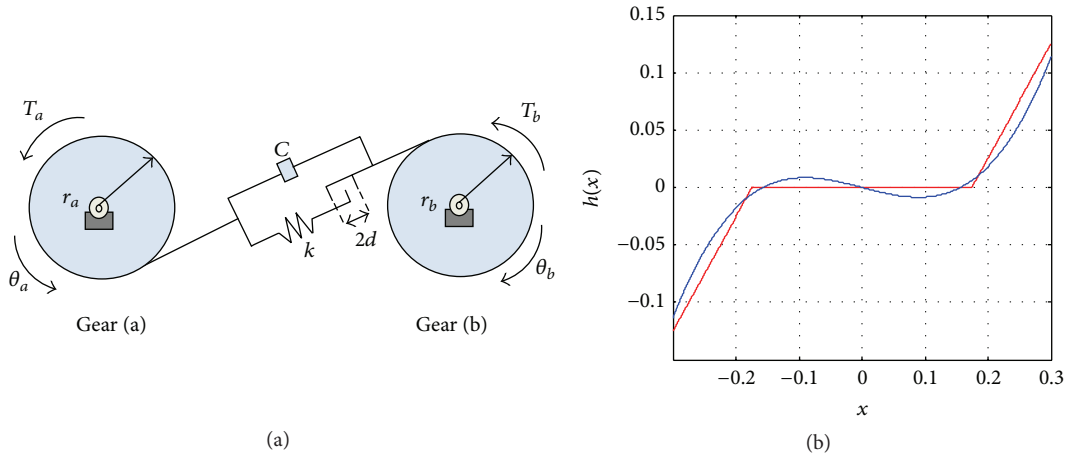

Figure 1: (a) A gear pair model and (b) the approximation of $h(x)$ based on a third-order polynomial.

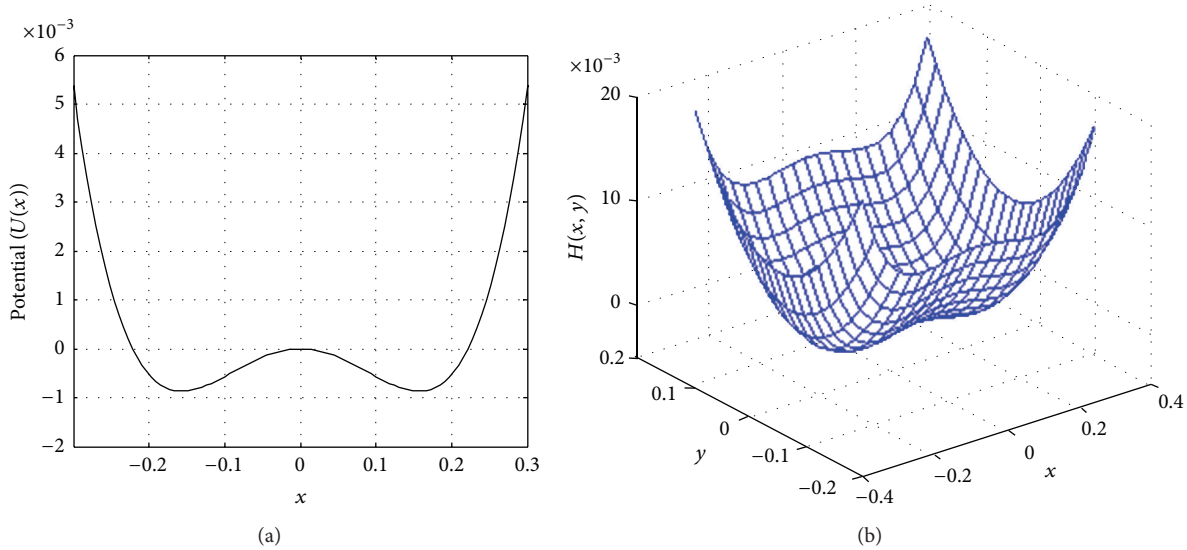

Figure 2: (a) Potential function and (b) Hamiltonian function of the unperturbed system.

where $b = 0.1422$ and $c = 5.8093$. The system of (8) is a Hamiltonian system with a potential function as

$$U(x) = -\frac{bx^2}{2} + \frac{cx^4}{4}. \tag{9}$$

The Hamiltonian function of the unperturbed system is given by

$$H(x, y) = \frac{y^2}{2} + U(x) = \frac{1}{2}y^2 - \frac{b}{2}x^2 + \frac{c}{4}x^4. \tag{10}$$

The potential function and the Hamiltonian function of the unperturbed system are shown in Figures 2(a) and 2(b), respectively. The unperturbed system has three fixed points: $(0, 0)$ and $(\pm\sqrt{b/c}, 0)$. From the linear stability analysis, $(\sqrt{b/c}, 0)$ and $(-\sqrt{b/c}, 0)$ are centers, and $(0, 0)$ is a saddle point. The saddle point is connected to itself by two homoclinic orbits. In order to obtain homoclinic function, transforming (10) for a constant energy, chosen as zero, the homoclinic trajectories are obtained as

$$\left(x_h^{\pm}(\tau), y_h^{\pm}(\tau)\right) = \left(\pm\sqrt{\frac{2b}{c}}\sec h\left(\sqrt{b}(\tau)\right), \mp\sqrt{\frac{2}{c}}b\sec h\left(\sqrt{b}(\tau)\right)\tanh\left(\sqrt{b}(\tau)\right)\right), \tag{11}$$

where $t - t_0 = \tau$. Stable and unstable manifolds of homoclinic orbits ($W_s^{\pm}$ and $W_u^{\pm}$) are shown in Figure 3.

3.2. Melnikov Analysis for Gear Equation. In this subsection, the conditions for existence of the homoclinic bifurcation and chaos by using the Melnikov method are given. The Melnikov function measures the distance between the stable and unstable manifolds in the Poincare section. According to

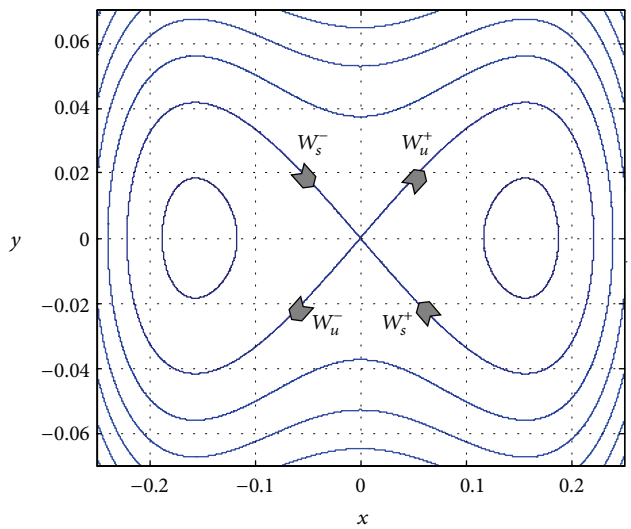

FIGURE 3: Phase portrait and homoclinic orbits of unperturbed system.

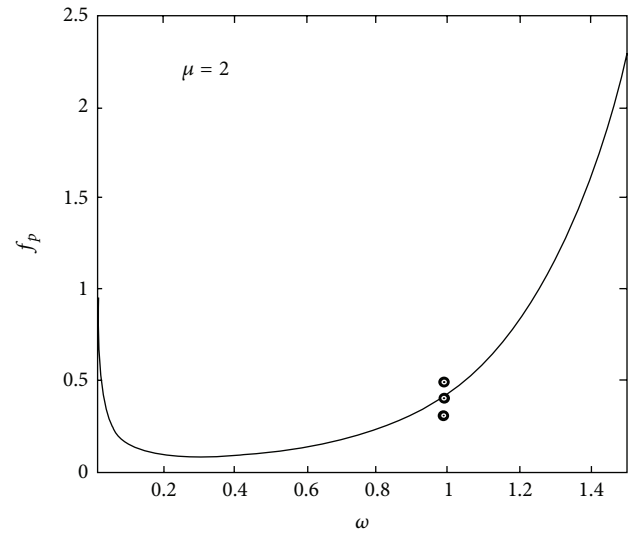

FIGURE 4: Homoclinic bifurcation curve in the $(f_p - \omega)$ plane.

this theory, the existence of transversal intersection of stable and unstable manifolds of homoclinic orbits implies the existence of the chaotic dynamics. The generalized equation (see (7)) can be written in the vector form as

$$\begin{aligned} \dot{x} &= p_1(x, y) + \varepsilon q_1(x, y, t), \\ \dot{y} &= p_2(x, y) + \varepsilon q_2(x, y, t), \end{aligned} \tag{12}$$

where

$$\begin{aligned} &p_1(x, y) = y, \qquad q_1(x, y, t) = 0, \\ &p_2(x, y) = \left(bx - cx^3\right), \\ &q_2(x, y, t) = -\mu\dot{x} + f_m + \sum_{r=1}^{\infty} f_{pr} \cos(\omega t + \varphi_r). \end{aligned} \tag{13}$$

Using the Melnikov function the distance between the stable and unstable manifolds is defined as [6]

$$\begin{aligned} M(t_0) = &\int_{-\infty}^{+\infty} p(X_h(\tau)) \wedge q(X_h(\tau), t) \\ &\times \exp\left[-\int_0^T \operatorname{trace}\left[D_X(p(X_h(s)))\right] ds\right] d\tau, \end{aligned} \tag{14}$$

where $X_h = (x_h, y_h)$ represents homoclinic orbits, D_X is the partial derivative with respect to $X = (x, y)$, and

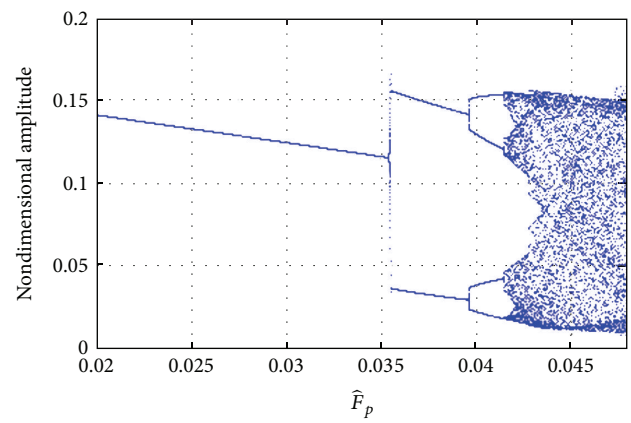

FIGURE 5: Bifurcation diagram using $\widehat{F}_p$ ($\widehat{F}_p = \varepsilon f_p$) as control parameter.

$p \wedge q = p_1 q_2 - p_2 q_1$. Substituting (12) into (14), the Melnikov integral could be rewritten as

$$\begin{aligned} M(t_0)^{\pm} = &\int_{-\infty}^{+\infty} \left[\mp\sqrt{\frac{2}{c}} b \operatorname{sech}\left(\sqrt{b}\tau\right) \tanh\left(\sqrt{b}\tau\right)\right] \\ &\cdots \left[-\mu\left(\mp\sqrt{\frac{2}{c}} b \operatorname{sech}\left(\sqrt{b}\tau\right) \tanh\left(\sqrt{b}\tau\right)\right)\right. \\ &\left. + f_m + \sum_{r=1}^{\infty} f_{pr} \cos\left(\omega(\tau + t_0) + \varphi_r\right)\right] d\tau. \end{aligned} \tag{15}$$

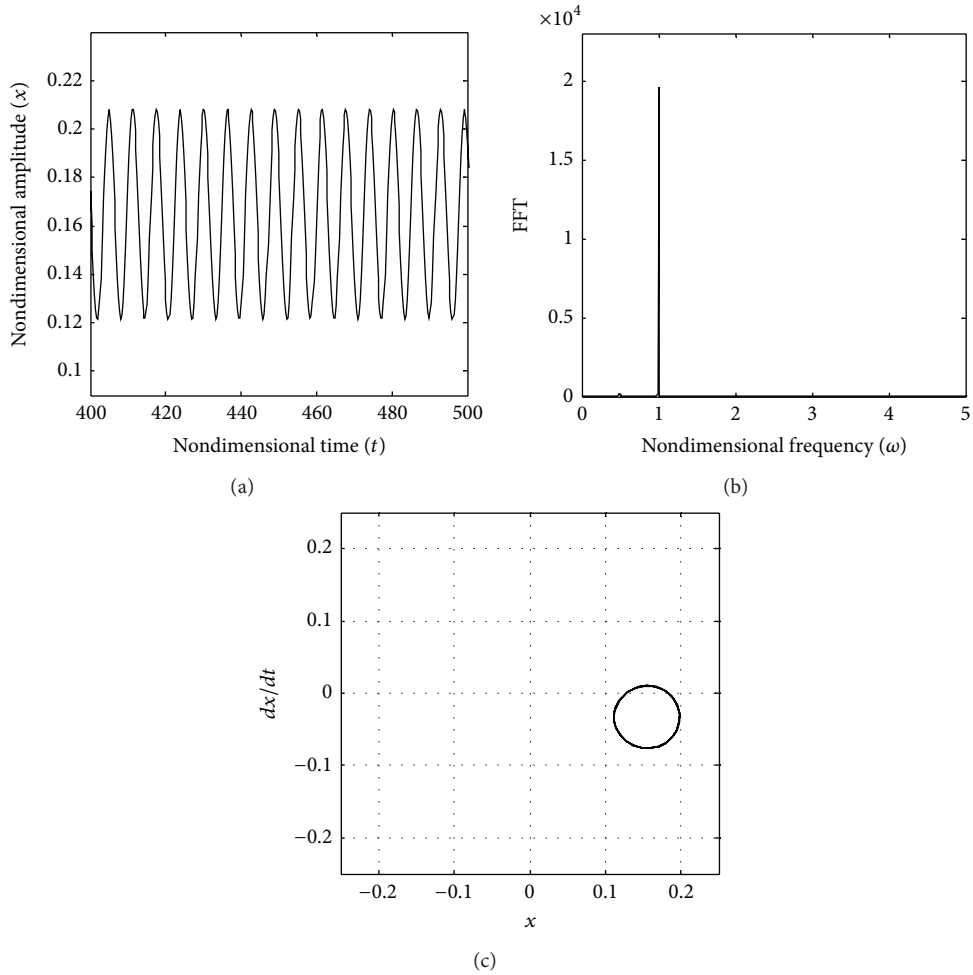

Figure 6: (a) Time history, (b) Fourier spectra, and (c) phase plane, for $f_p = 0.3$.

Considering only the first harmonics term ($r = 1$) and evaluating the integral, the Melnikov function can be written as

$$M(t_0)^{\pm} = -\frac{4}{3}\frac{\mu(b)^2}{c\sqrt{b}} \pm \sqrt{\frac{2}{c}} f_p \pi\omega \sec h\left(\frac{\pi\omega}{2\sqrt{b}}\right) \sin\left(\omega t_0 + \varphi_r\right)$$
$$= A \pm D \sin\left(\omega t_0 + \varphi_r\right). \tag{16}$$

If the Melnikov function has a simple zero, then the stable and unstable manifolds intersect transversally, homoclinic bifurcation occurs and hence chaotic behavior is expected. Thus, the conditions for the occurrence of chaos are obtained as

$$|A| \le |D| \Longrightarrow \left|-\frac{4}{3}\frac{\mu(b)^2}{c\sqrt{b}}\right| \le \left|\sqrt{\frac{2}{c}} f_p \pi\omega \sec h\left(\frac{\pi\omega}{2\sqrt{b}}\right)\right|. \tag{17}$$

This condition provides a domain on the parameter spaces where the system has transverse homoclinic orbits resulting in possible chaotic behavior.

4. Numerical Simulations

In this section, we give the numerical simulation to demonstrate the theoretical results from Melnikov analysis obtained in the previous section. The influence of control parameters on the character of vibration and frequency response is studied. Using (17) and choosing f_p as control parameter, the condition for transverse intersection of stable and unstable manifolds is obtained as

$$f_p \ge \frac{2\sqrt{2}}{3}\frac{\mu(b)^{3/2}}{\pi\omega\sqrt{c}} \cos h\left(\frac{\pi\omega}{2\sqrt{b}}\right). \tag{18}$$

This condition provides a domain on the parameter spaces where the system has transverse homoclinic orbits resulting in possible chaotic dynamics. Figure 4 depicts the threshold curves f_p for homoclinic bifurcation in the $(f_p - \omega)$ plane for $\mu = 2$. In the parameter region above the threshold curve the transverse intersections of stable and unstable manifolds occur. As it can be observed from this figure, the threshold value is $f_p = 0.43$, for $\omega = 1$. Since Melnikov function can change its sign for $f_p > 0.43$, chaos may occur.

To confirm the analytical prediction, the bifurcation diagram has been depicted. The nonlinear equation (6) is

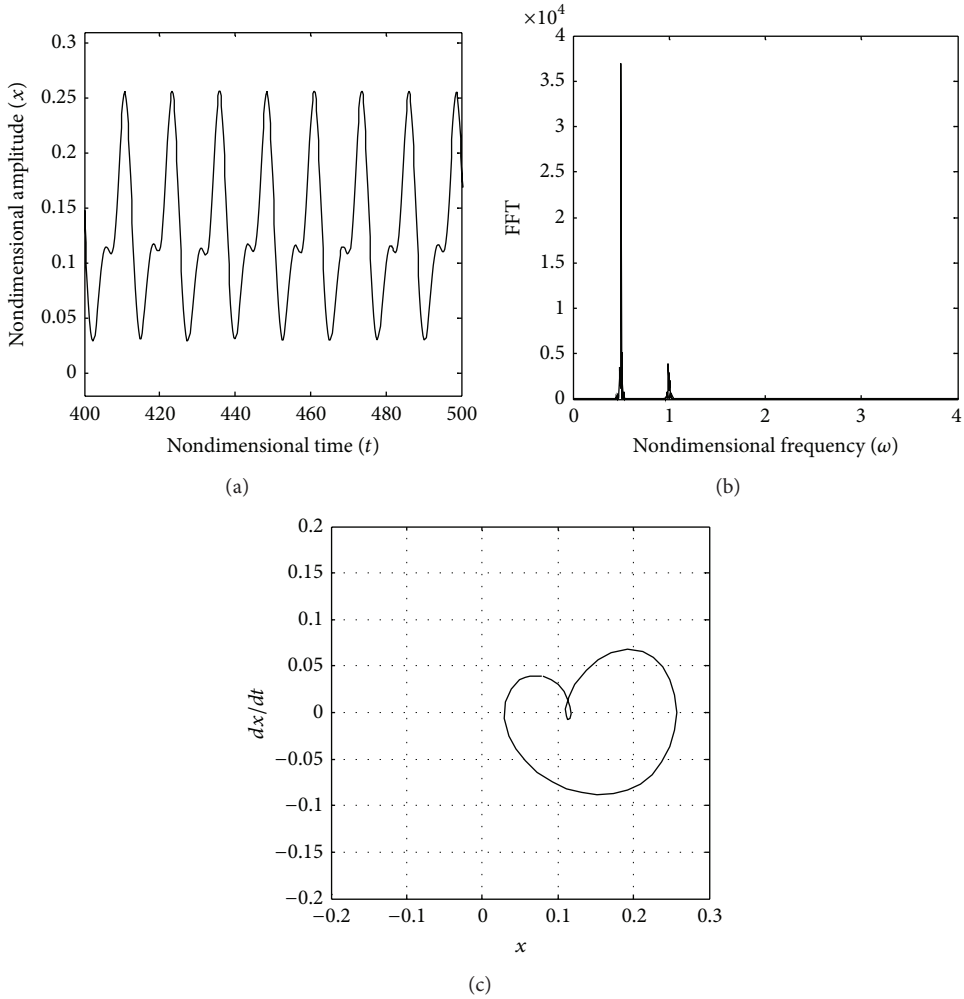

Figure 7: (a) Time history, (b) Fourier spectra, and (c) phase plane, for $f_p = 0.38$.

integrated numerically using the fourth-order Runge-Kutta method. Figure 5 presents the bifurcation diagram of system using the f_p as a bifurcation parameter. The values of the parameters are fixed as $\omega = 1$, $\mu = 2$, $f_m = 0.05$, and $\varepsilon = 0.1$ and initial conditions as $x = 0.01$ and $\dot{x} = 0.01$. It can be observed that the gear system exhibits a 1T-periodic response at low values of f_p; that is, $f_p \leq 0.35$. However, as f_p is increased the period 1 solution bifurcates to a 2T-periodic solution through a period doubling bifurcation. With the increase of the parameter f_p, period doubling occurs, and a bifurcation cascade leading to chaos, which is consistent with the prediction of analytical chaos, was presented in Figure 4.

For a better clarity, the transition to chaos through the numerical simulation is shown for three values of $f_p = 0.3$, $f_p = 0.38$, and $f_p = 0.45$ (see Figures 4 and 5). Point 1 ($f_p = 0.3$, $\omega = 1$) and point 2 ($f_p = 0.38$, $\omega = 1$), lying out of chaos, and point 3 ($f_p = 0.45$, $\omega = 1$), lying in the chaotic area, can be observed. Point 1 corresponds to the point situated below threshold values and is associated with the periodic motion. The numerical simulations of (6) are performed for the parameter sets associated with this point. The time history, phase plane diagram, and Fourier spectra are shown in Figure 6. These figures show the periodic response and confirm that the prediction of a periodic motion was obtained by Melnikov theory.

In the next computational step, $f_p = 0.38$ (point 2) is considered. It corresponds to the point situated below threshold values (Figure 4) and is associated with the 2T-periodic motion (Figure 5). The Melnikov function does not change its sign; thus, a periodic motion occurs. Figure 7 illustrates the time history, phase plane, and Fourier spectra for the parameter $f_p = 0.38$. Observe that for this point the 2T-periodic motion occurs.

Finally, the numerical analysis is carried out for the parameter $f_p = 0.45$. The Melnikov function changes its sign for $f_p = 0.45$ and corresponds to the chaotic motion. The chaotic trajectories are obtained by numerical integration. The time history, phase plane, and Fourier spectra corresponding to the chaotic response are presented in Figure 8. Chaotic behavior is clearly visible. The numerical computations confirm the prediction of analytical chaos for applied value of f_p.

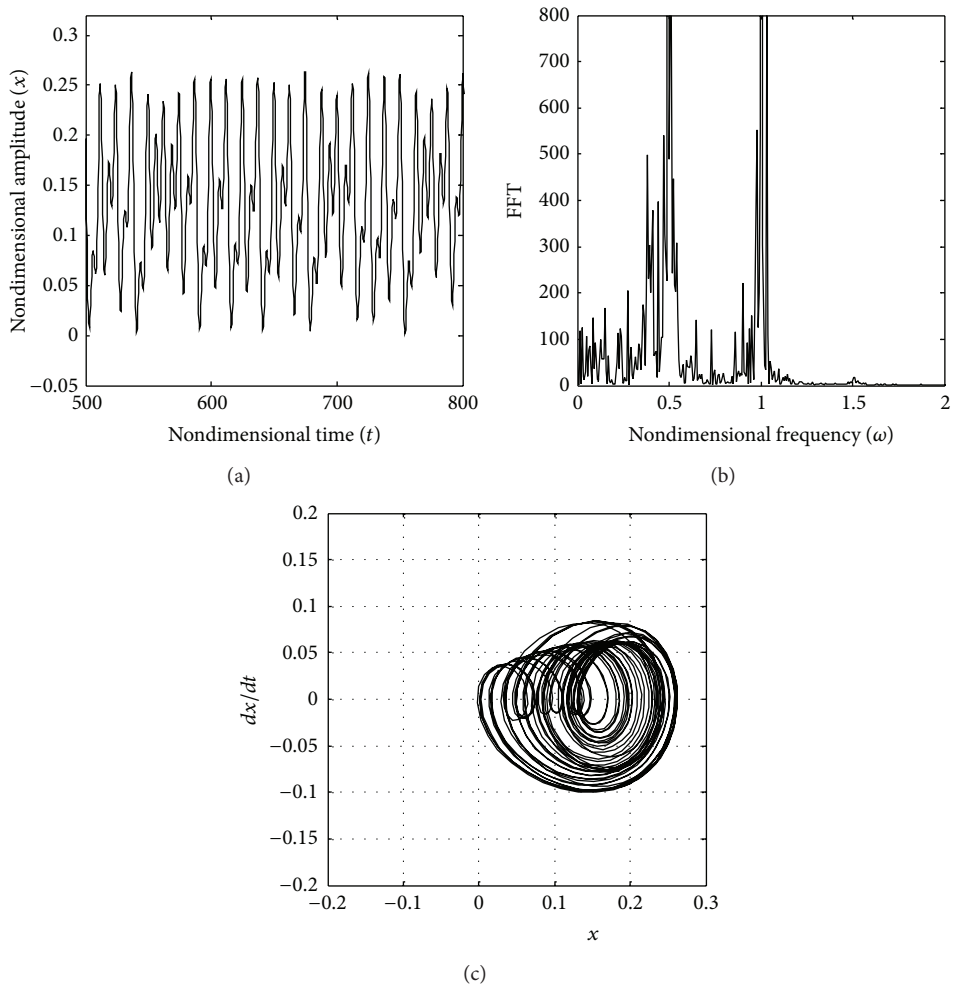

FIGURE 8: (a) Time history, (b) Fourier spectra, and (c) phase plane, for $f_p = 0.45$.

The dependence of the excitation f_p for homoclinic chaos for different values of the damping parameter μ for a frequency range $0 < \omega < 1.5$ has been plotted. The surfaces are shown in Figure 9(a). These surfaces play an important role in the formation of the chaotic region. More precisely, this condition provides a domain on the parameter spaces where the system has transverse homoclinic orbits resulting in possible chaotic behavior. As it can be observed from this figure, as μ increases the threshold f_p obtained by the Melnikov method increases on the frequency $0 < \omega < 1.5$.

Now we consider the effect of the parameter μ for the occurrence of homoclinic bifurcation and chaos in system. Using (17) and choosing μ as control parameter, the condition for transverse intersection of stable and unstable manifolds is given by

$$\mu \leq \frac{3\sqrt{2}}{4} \frac{\pi \omega c f_p}{b\sqrt{b}} \sec h\left(\frac{\pi\omega}{2\sqrt{b}}\right). \tag{19}$$

In order to have a better understanding, we have plotted in Figure 9(b) the dependence of the parameter μ on the frequency $0 < \omega < 2$ for different values of f_p. In the parameter region below the threshold curve transverse intersection of stable and unstable manifolds occurs, and the onset of chaos is expected. One observation from this figure is that the threshold μ increases when f_p increases. These surfaces provide a domain on the parameter spaces where the system has homoclinic bifurcation resulting in possible chaotic dynamic. More precisely, these results play an important role in the formation of the chaotic regions and could be used for the analysis and design of the gear system parameters.

5. Conclusions

In this paper, a nonlinear model of a spur gear system has been proposed to investigate the homoclinic bifurcation and the chaotic behaviors of system. From the Melnikov approach, the threshold values of the control parameter for the occurrence of homoclinic bifurcation and onset of chaos have been predicted. The analytical predictions have been validated with numerical simulations and good agreement is observed. Analyzing and predicting the chaotic behaviors of a gear system are useful. The results provide some idea and guidance for the analysis of the gear system parameters and

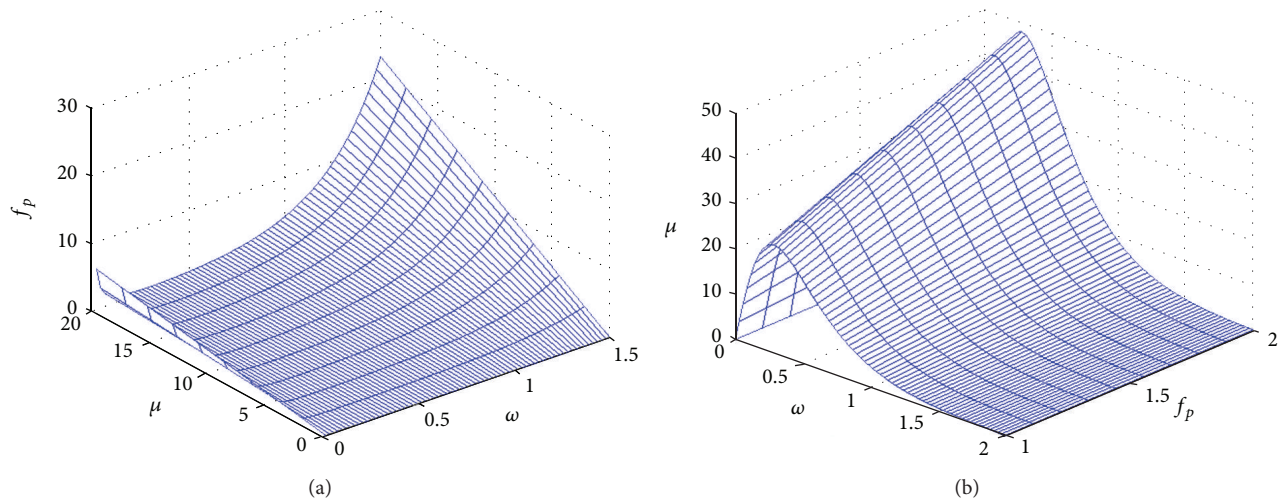

Figure 9: Homoclinic bifurcation curve for (a) control parameter f_p and (b) control parameter μ.

could be used for designing and developing an optimal gear transmission system.

Conflict of Interests

The authors declare that there is no conflict of interests regarding the publication of this paper.

References

[1] K. Sato, S. Yamamoto, and T. kawakami, "Bifurcation sets and chaotic states of a gear system subjected to harmonic excitation," *Computational Mechanics*, vol. 7, no. 3, pp. 173–182, 1991.

[2] C. Padmanabhan and R. Singh, "Spectral coupling issues in a two-degree-of-freedom system with clearance non-linearities," *Journal of Sound and Vibration*, vol. 155, no. 2, pp. 209–230, 1992.

[3] A. Kahraman and G. W. Blankenship, "Experiments on nonlinear dynamic behavior of an oscillator with clearance and periodically time-varying parameters," *Journal of Applied Mechanics, Transactions ASME*, vol. 64, no. 1, pp. 217–226, 1997.

[4] S. Theodossiades and S. Natsiavas, "Periodic and chaotic dynamics of motor-driven gear-pair systems with backlash," *Chaos, Solitons and Fractals*, vol. 12, no. 13, pp. 2427–2440, 2001.

[5] C.-W. Chang-Jian and S.-M. Chang, "Bifurcation and chaos analysis of spur gear pair with and without nonlinear suspension," *Nonlinear Analysis: Real World Applications*, vol. 12, no. 2, pp. 979–989, 2011.

[6] S. Wiggins, *Introduction to Applied Nonlinear Dynamical Systems and Chaos*, Springer, New York, NY, USA, 1990.

[7] W. Zhang, M. H. Yao, and J. H. Zhang, "Using the extended Melnikov method to study the multi-pulse global bifurcations and chaos of a cantilever beam," *Journal of Sound and Vibration*, vol. 319, no. 1-2, pp. 541–569, 2009.

[8] L. Zhou, Y. Chen, and F. Chen, "Global bifurcation analysis and chaos of an arch structure with parametric and forced excitation," *Mechanics Research Communications*, vol. 37, no. 1, pp. 67–71, 2010.

[9] T. C. Kim, T. E. Rook, and R. Singh, "Super- and sub-harmonic response calculations for a torsional system with clearance nonlinearity using the harmonic balance method," *Journal of Sound and Vibration*, vol. 281, no. 3–5, pp. 965–993, 2005.

Hindawi Publishing Corporation
Shock and Vibration
Volume 2014, Article ID 472524, 5 pages
http://dx.doi.org/10.1155/2014/472524

Research Article

Conference Room Reverberation Time Correction Using Helmholtz Resonators Lined with Absorbers

Hossein Namvar Arefi,[1] Seyyed Mohammad Amin Ghiasi,[2] Seyyede Mahshid Ghaffari,[2] Farhad Ramezanghorbani,[2] Shiva Sharifpour,[2] Peyman Irajizad,[2] Seyede Delaram Ghoreishi Langroudi,[2] and Ahmad Amjadi[2]

[1] *Audiology Department, Tehran University of Medical Sciences, Mirdamad Street, Tehran 1348715459, Iran*
[2] *Physics Department, Sharif University of Technology, Azadi Street, Tehran 111558639, Iran*

Correspondence should be addressed to Hossein Namvar Arefi; hnamvar91@gmail.com

Received 19 October 2012; Accepted 19 November 2012; Published 27 May 2014

Academic Editor: Hamid Ahmadian

Echo and sound resonance in a conference room cause obscure speech and make listeners tired. Thus, the acoustical properties of a conference room are vitally important. The conference room 412 at Sharif University Physics Department failed to meet basic acoustical standards. The aim of this research is to improve reverberation time (RT) of the conference room using Helmholtz resonators with defined dimensions, diffusers, and sound absorbers. Helmholtz resonators are widely used to absorb sound noise especially at low frequencies. They are particularly useful when noise has a narrow-frequency band. One of the advantages of using Helmholtz resonators is their capacity to be tuned on different frequencies. We enhanced acoustical properties of Helmholtz resonators using proper absorbers and diffusers. In order to decrease the RT, a large number of Helmholtz resonators have been made and installed in proper positions in the conference room. The RT was measured before and after installation. The measurements indicate that the acoustical characteristics of the conference room have been significantly improved.

1. Introduction

Helmholtz resonator is an acoustical tool frequently used in applied acoustics. Basically it is a cavity that is connected with the outside space through a neck or an opening and collects sound waves within its resonance frequency [1]. Acoustic resonators with sound absorbers efficiently absorb sounds near their resonance frequencies [2]. They have been in widespread use since Ancient Greece [3]. Today they are employed to enhance sound fields in large reverberant spaces such as churches [4] and as mufflers in ducts [5].

A well-tuned Helmholtz resonator is very useful for attenuating low-frequency noises [6], which makes them useful as low-frequency sound absorbers in large reverberant halls [7].

Reverberation time (RT) is a temporal parameter to evaluate properness of the acoustical properties in indoor spaces. It is defined as the time required for the sound pressure level to decay by 60 dB [8]. Since reverberation prolongs acoustic events, RT is an important parameter influencing the quality of our hearing [9]. Speech intelligibility improves at some defined RTs ranges. Thus, it is necessary for speech oriented rooms, such as conference rooms, to have short RTs. On the other hand, early reflection of reverberating sound improves speech intelligibility in large spaces [10].

In this research, we used Helmholtz resonators in order to reduce the RT at low frequencies. When a sound is reradiated from the resonator's opening, it tends to spread as a hemisphere; thereby, it diffuses unabsorbed energy and improves sound quality in a studio or listening room [11].

2. Description and Experiment

The reverberation time has always been the basic indicator of acoustical behavior [12]. In the present work, we measured

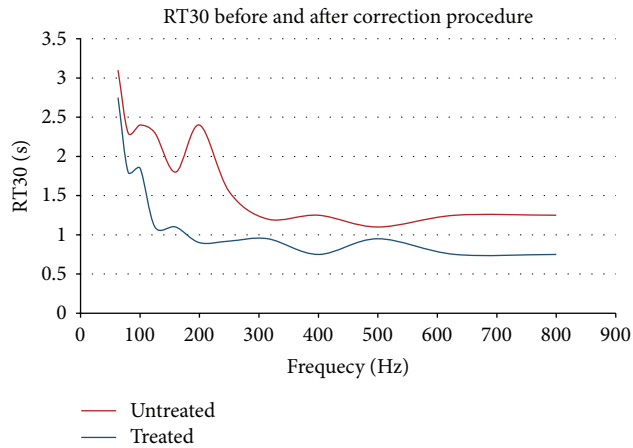

Figure 1: The RT30 of the conference room (a) before and (b) after correction.

RT30 (the time in which the sound intensity decreases by 30 dB) as Li and Lam [13]. It is measured in 1/3 octave frequencies before and after the placement of Helmholtz resonators in the conference room. The measurements were performed using a standard microphone calibrated by B&K 2250 Sound Level Meter (SLM) with ZC024 microphone. The accuracy of the SLM is 0.1 dB; therefore, accuracy of the microphone is also 0.1 dB.

The conference room number 412 of the Physics Department at Sharif University of Technology with dimension $11 \times 9 \times 4\,\mathrm{m}^3$ has moderately high RT30 for frequencies below 315 Hz. The standard RT30 for such a conference room is 0.5 seconds [11] but at the beginning of this work it was measured to be more than 1.5 seconds.

This phenomenon makes the speakers slightly obscure and the listeners uncomfortable by receiving a speech with high echo at low frequencies. Therefore, in this project, we tried to reduce RT of this room at frequencies below 315 Hz.

Figure 1 shows the measured RT30 before any acoustical correction in the conference room. The plot shows that there are three peaks in RT30 graph. The first peak is below 60 Hz, which human ear is not sensitive to [14]; that is, human thresholds below 60 Hz are very high [15]. The second and the third peaks are around 100 Hz and 200 Hz. We focused on decreasing the RTs of second and third peaks. The final results after positioning the designed resonators are shown in Figure 1(b).

It should be mentioned that when audiences are present in the conference room, RTs decrease from what is shown in Figure 1 [11]. Our focus is on low frequencies which are more difficult to be absorbed and have high RTs even in the presence of audience.

Helmholtz resonators were tuned at 100 Hz with desirable quality factor; they resonate approximately between 80 Hz and 140 Hz. Their resonance frequency is approximately given by [16]

$$f = \frac{c}{2\pi}\sqrt{\frac{A}{(L + 1.5a)\,V}}, \tag{1}$$

in which c is the speed of sound in air, A is the area of the neck, a, L and V are the radius of the neck, its length and chamber's volume respectively.

Regarding above equation, we calculated the area of neck and its length and the volume of the chamber. The calculations resulted in $A = 2.25\pi\,\mathrm{cm}^2$ (in circular form with radius = 1.5 cm), $L = 1.5$ cm, and $V = 5832\,\mathrm{cm}^3$. Dimensional restrictions also have contribution to these results, as we will discuss in the next paragraph.

Fortunately, the fluorescent lamps of the conference room had a suitable space to position our resonators. We put chambers above the fluorescent lamps and a velvet cloth was wrapped around them for beauty. We also lined the inner side of the Helmholtz resonators with carpet and placed some pieces of rock wool inside them with suitable acoustic absorption. The absorption of rock wool and carpet versus frequency were measured and shown in Figure 3. Selamet et al. investigated that the fibrous materials in the cavity lower the resonance frequency and the peak transmission loss. Due to this study it has been evidenced that using absorbers with different materials and thicknesses reduce resonant frequency [17].

The chambers were designed to be cubic, because of simplicity in production and stability after placement. The sides in cubic resonators were chosen equal to the lamps width. Then the length of neck acting as the acoustic reluctance was calculated from (1). In addition, we embedded the neck of resonators in its volume for protection (Figure 5). Embedding neck is discussed in [18]. Overall, we made 72 boxes of resonators. Figure 4 schematically shows position of fluorescent lamps and Helmholtz boxes in the conference room.

Helmholtz boxes were made of cardboard. We have analyzed cardboards in electroacoustic laboratory live room located at Physics Department. It was found that cardboards used in this study have a major absorbing characteristic from 200 Hz to 300 Hz. We covered approximately 70% of the live room floor by cardboards; and RT60 of the room was decreased from 3.2 seconds to 1.6 seconds in 250 Hz. But in other frequencies the changes were not significant.

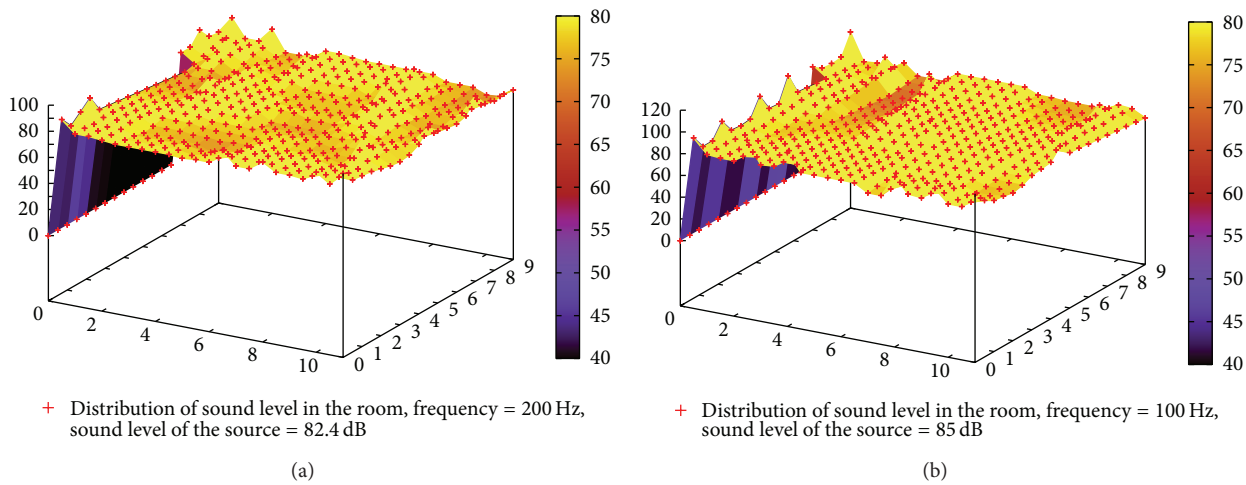

Figure 2: Noise map of the conference room in 100 Hz (a) and 200 Hz (b).

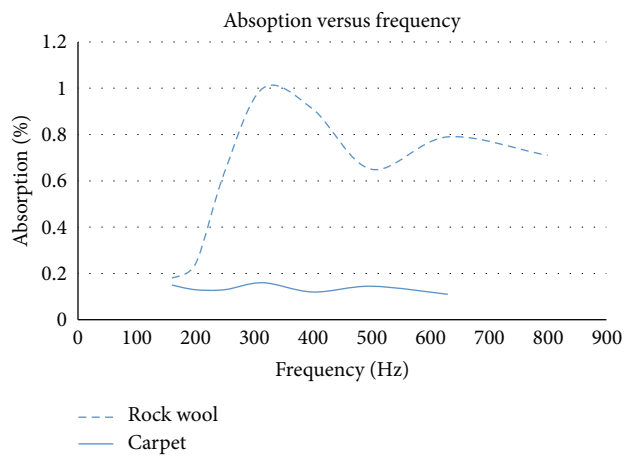

Figure 3: Absorption of rock wool and carpet versus frequency.

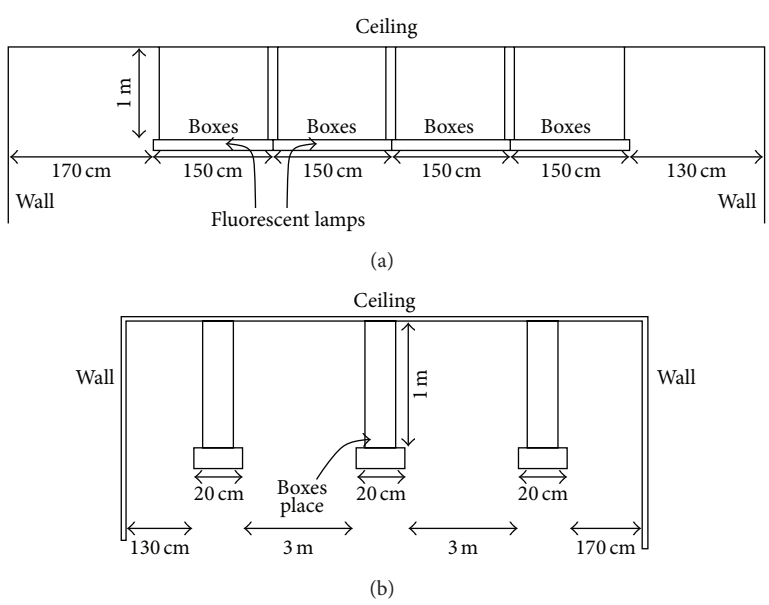

Figure 4: Schematic rear and side view of fluorescent lamps in conference room.

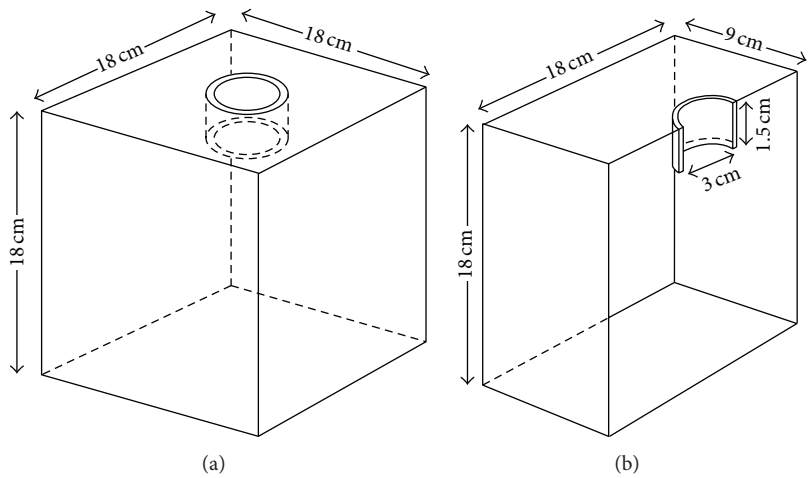

Figure 5: Schematic view of cubic Helmholtz resonators used in this project: (a) full view and (b) cross section view.

For instance, RT60 was decreased from 2.6 seconds only to 2.4 seconds in 150 Hz and from 1.8 to 1.6 in 350 Hz. Although Helmholtz boxes were made in order to resonate in 100 Hz, absorbing property of cardboards extends absorbing bandwidth up to 300 Hz. Thus, it can be used to remove 200 Hz peak in Figure 1.

Obviously, above approximately 100 Hz, we successfully decreased RT30 of the conference room below 1 second. This work took about 1000 student-hours' work.

3. Future Works

We have investigated that the presence of a spherical ball below the neck in a Helmholtz resonator increases its absorption while decreasing its bandwidth (Figures 6 and 7). The experiment was conducted using cylindrical Helmholtz resonator made of PVC. These measurements gave us the clue to insert a ball below the neck of the resonators in room number 412, in order to increase their absorption.

4. Conclusion

Our experiments indicate that there is a natural resonance frequency from 200 Hz to 300 Hz in the carton boxes used for construction of our Helmholtz resonators. By using this property and tuning the Helmholtz resonators in 100 Hz, we successfully reduced the reverberation time peaks in the conference room of Physics Department at Sharif University as shown in Figure 1. Also we are able to enhance the performance of Helmholtz resonators by positioning a sphere (ping pong ball) as a diffuser inside the resonator across the neck. The radius and the position of the sphere are the parameters which have to be investigated in more detail in the next work.

Conflict of Interests

The authors declare that there is no conflict of interests regarding the publication of this paper.

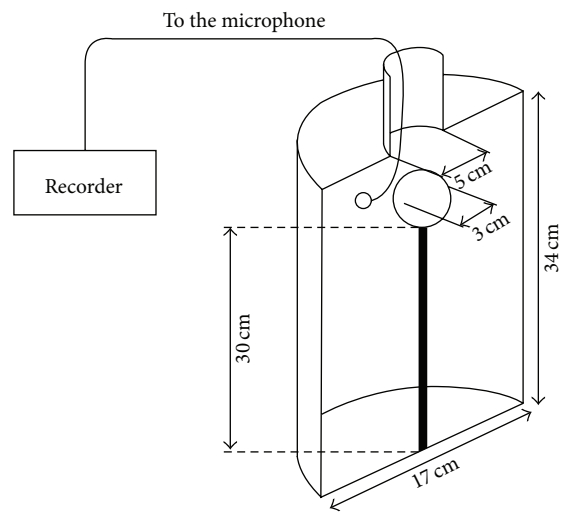

Figure 6: Schematic cross section view of the setup for ping pong ball below the neck of a Helmholtz resonator.

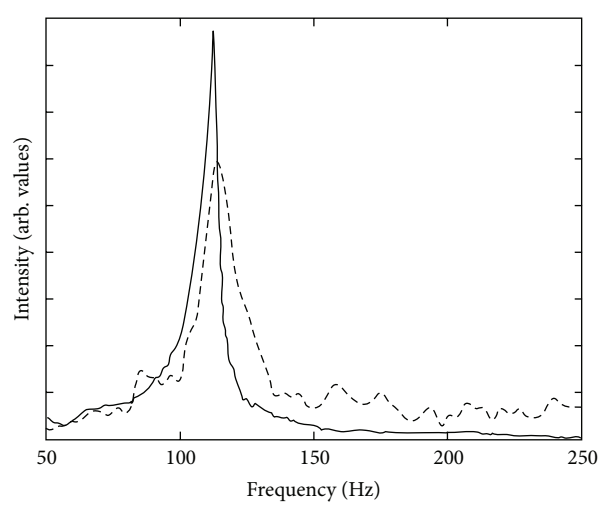

Figure 7: Response of a Helmholtz resonator with a ping pong ball below the neck (solid line) and the empty Helmholtz resonator (dashed line).

Acknowledgments

The authors thank Ramin Jafarzadegan, Zahra Mokhtari, Arezoo Dehghanfar, and Mohammad Alavi Tabar for measuring and plotting Figure 2 in this research.

References

[1] M. Alster, "Improved calculation of resonant frequencies of Helmholtz resonators," *Journal of Sound and Vibration*, vol. 24, no. 1, pp. 63–85, 1972.

[2] U. Ingard, "On the theory and design of acoustic resonators," *Journal of Acoustical Society of America*, vol. 25, no. 6, pp. 1037–1061, 1953.

[3] U. Ingard, *Notes on Sound Absorption Technology*, Noise Control Foundation, New York, NY, USA, 1994.

[4] J. S. Anderson and M. B. Anderson, *Noise: Its Measurement, Analysis, Rating and Control*, Gower Technical, 1993.

[5] M. L. Munjal, *Acoustics of Ducts and Mufflers with Application to Exhaust and Ventilation System Design*, John Wiley & Sons, New York, NY, USA, 1987.

[6] S. K. Tang, C. H. Ng, and E. Y. L. Lam, "Experimental investigation of the sound absorption performance of compartmented Helmholtz resonators," *Applied Acoustics*, vol. 73, no. 9, pp. 969–976, 2012.

[7] A. Fry, *Noise Control in Building Services*, Pergamon, Oxford, UK, 1988.

[8] L. K. Wang, *Advanced Air and Noise Pollution Control*, vol. 2, Humana Press, New York, NY, USA, 2004.

[9] F. E. Toole, *Sound Reproduction: Loudspeakers and Rooms*, Elsevier, New York, NY, USA, 2008.

[10] J. S. Bradley, H. Sato, and M. Picard, "On the importance of early reflections for speech in rooms," *The Journal of the Acoustical Society of America*, vol. 113, no. 6, pp. 3233–3244, 2003.

[11] F. A. Everest, *The Master Handbook of Acoustics*, McGraw-Hill, New York, NY, USA, 4th edition, 2001.

[12] K. Jambrosic, "Reverberation time measuring methods," *Journal of Acoustical Society of America*, vol. 123, p. 3617, 2008.

[13] K. M. Li and P. M. Lam, "Prediction of reverberation time and speech transmission index in long enclosures," *Journal of the Acoustical Society of America*, vol. 117, no. 6, pp. 3716–3726, 2005.

[14] R. J. Roeser, *Audiology Diagnosis*, Thieme, New York, NY, USA, 2007.

[15] G. Stanley, *Hearing: An Introduction to Psychological and Physiological Acoustics*, CRC Press, New York, NY, USA, 2009.

[16] E. Kinsler, A. R. Frey, A. B. Coppens, and L. E. Sanders, *Fundamentals of Acoustic*, John Wiley & Sons, New York, NY, USA, 1999.

[17] A. Selamet, M. B. Xu, I.-. Lee, and N. T. Huff, "Helmholtz resonator lined with absorbing material," *Journal of the Acoustical Society of America*, vol. 117, no. 2, pp. 725–733, 2005.

[18] R. Bi, Z. S. Liu, K. M. Li, J. Chen, and Y. Wang, "Helmholtz resonator with extended neck and absorbing material," *Applied Mechanics and Materials*, vol. 141, no. 1, pp. 308–312, 2012.

Hindawi Publishing Corporation
Shock and Vibration
Volume 2014, Article ID 592165, 8 pages
http://dx.doi.org/10.1155/2014/592165

Research Article

Dynamic Response of a Thick Piezoelectric Circular Cylindrical Panel: An Exact Solution

Atta Oveisi, Mohammad Gudarzi, and Seyyed Mohammad Hasheminejad

Department of Mechanical Engineering, Iran University of Science and Technology, Narmak, Tehran 1684613114, Iran

Correspondence should be addressed to Mohammad Gudarzi; gudarzi@iust.ac.ir

Received 26 September 2012; Accepted 19 November 2012; Published 27 May 2014

Academic Editor: Hamid Ahmadian

One of the interesting fields that attracted many researchers in recent years is the smart structures. The piezomaterials, because of their ability in converting both mechanical stress and electricity to each other, are very applicable in this field. However, most of the works available used various inexact two-dimensional theories with certain types of simplification, which are inaccurate in some applications such as thick shells while, in some applications due to request of large displacement/stress, thick piezoelectric panel is needed and two-dimensional theories have not enough accuracy. This study investigates the dynamic steady state response and natural frequency of a piezoelectric circular cylindrical panel using exact three-dimensional solutions based on this decomposition technique. In addition, the formulation is written for both simply supported and clamped boundary conditions. Then the natural frequencies, mode shapes, and dynamic steady state response of the piezoelectric circular cylindrical panel in frequency domain are validated with commercial finite element software (ABAQUS) to show the validity of the mathematical formulation and the results will be compared, finally.

1. Introduction

Piezoelectric materials have been extensively used as transducers and sensors due to their intrinsic direct and converse piezoelectric effects that take place between electric field and mechanical deformation. An important geometry in applied engineering problems is circular cylindrical panel because of its widespread application in actual structures such as aircraft wings, submarines, missiles, vessels, and high pressure cylindrical containers. The application of piezomaterial structures in this field is mainly concentrated on vibration suppression and acoustic noise reduction. Because of practical applications, piezoelectric circular cylindrical shells have attracted a considerable amount of research interests. Haskins and Walsh analyzed the free vibration of piezoelectric cylindrical shells with radially polarized transverse isotropy [1]; Martin investigated the vibration of longitudinally polarized piezoelectric cylindrical tubes and pointed out the limitations of the assumption [2]. Drumheller and Kalnins presented a coupled theory for the vibration of piezoceramic shells of revolution and analyzed the free axisymmetrical vibration of a circular cylindrical shell [3]. Burt simplified the circular cylinder to a two-dimensional model and then investigated the voltage response of radially polarized ceramic [4]. Tzou and Zhong gave a linear theory of piezoelectric shell vibration, which can be simplified to account for spheres [5]. Ebenezer and Abraham presented an Eigen function approach to determine the response of radially polarized piezoelectric cylindrical shells of finite length subjected to electrical excitation [6]. Many other researches by the methods of three-dimensional theory concentrated on the axisymmetrical and radial vibrations of cylinders, such as Stephenson [7, 8] and Adelman et al. [9, 10]. Paul derived the frequency equation of a piezoelectric cylindrical shell without presenting numerical results [11]. Paul and Venkatesan employed the same method to obtain the natural frequencies of infinite piezoelectric cylindrical shells [12]. However, some frequencies were missed in their calculation. Recently, Ding et al. exactly investigated the free vibration of hollow piezoelectric cylindrical shells on the basis of a decomposition formula for displacements, exactly [13]. Yang et al. considered the theory of the basic vibration characteristics of a circular cylindrical shell piezoelectric transducer [14]. They solved the vibration problem numerically for electrically

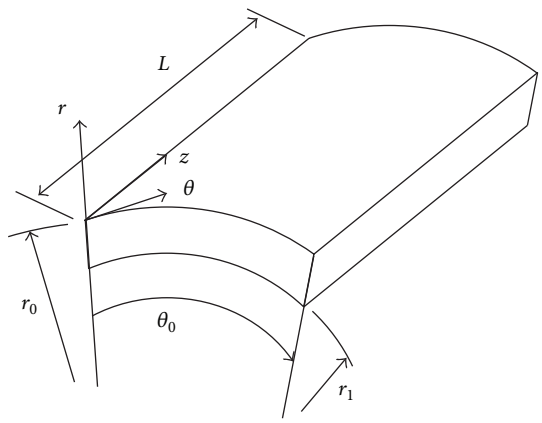

Figure 1: Cylindrical panel and its geometry.

forced case. Li et al. considered the spillover and harmonic effect in real active vibration control and they presented a novel composite controller based on disturbance observer (DOB) for the all-clamped panel [15]. Kumar and Singh aimed to examine through experiments vibration control of curved panel treated with optimally placed active or passive constrained layer damping patches and they found the optimum location for the application of ACLD/PCLD patches [16].

The main subject of this study is to investigate the free and forced vibration of transversely isotropic piezoelectric cylindrical panels. Based on the general solution for coupled equations for piezoelectric media presented in Ding et al. [17], three-dimensional exact solutions are obtained through the variable separation method. A numerical example is finally presented.

2. Problem Formulation

For dynamic modelling of piezoelectric layers, two displacement functions Ψ and F are considered [17]. Figure 1 shows the panel geometry.

2.1. Basic Equations. In circular cylindrical coordinates (r,θ,z), if the media is axially polarized the general solution can be written as

$$\begin{aligned} u_r^{Pi} &= \frac{1}{r}\frac{\partial\psi}{\partial\theta} - \frac{\partial}{\partial r}\mathscr{A}_1 F, \\ u_\theta^{Pi} &= -\frac{\partial\Psi}{\partial r} - \frac{1}{r}\frac{\partial}{\partial\theta}\mathscr{A}_1 F, \\ w^{Pi} &= \mathscr{A}_2 F, \qquad \phi = \mathscr{A}_3 F, \end{aligned} \tag{1}$$

where u_r^{Pi}, u_θ^{Pi}, and w^{Pi} are three displacement components, ϕ is the electric potential, and the differential operators $\mathscr{A}_1$, $\mathscr{A}_2$, and $\mathscr{A}_3$ are

$$\begin{aligned} \mathscr{A}_1 = {} & \left[\left(c_{13}^{Pi} + c_{44}^{Pi}\right)\varepsilon_{33} + \left(e_{15} + e_{31}\right)e_{33}\right]\frac{\partial^3}{\partial z^3} \\ & + \left[\left(c_{13}^{Pi} + c_{44}^{Pi}\right)\varepsilon_{11} + \left(e_{15} + e_{31}\right)e_{15}\right]\Lambda\frac{\partial}{\partial z}, \\ \mathscr{A}_2 = {} & c_{44}^{Pi}\varepsilon_{33}\frac{\partial^4}{\partial z^4} \\ & + \left\{\left[c_{11}^{Pi}\varepsilon_{33} + c_{44}^{Pi}\varepsilon_{11} + \left(e_{15} + e_{31}\right)^2\Lambda - \rho\varepsilon_{33}\frac{\partial^2}{\partial t^2}\right]\right\}\frac{\partial^2}{\partial z^2} \\ & + c_{11}^{Pi}\varepsilon_{11}\Lambda\Lambda - \rho\varepsilon_{11}\Lambda\frac{\partial^2}{\partial t^2}, \\ \mathscr{A}_3 = {} & c_{44}^{Pi}e_{33}\frac{\partial^4}{\partial z^4} \\ & + \left\{\left[c_{11}^{Pi}e_{33} + c_{44}^{Pi}e_{15} - \left(c_{13}^{Pi} + c_{44}^{Pi}\right)\left(e_{15} + e_{31}\right)\right]\Lambda \right. \\ & \left. -\rho e_{33}\frac{\partial^2}{\partial t^2}\right\}\frac{\partial^2}{\partial z^2} \\ & + c_{11}^{Pi}e_{15}\Lambda\Lambda - \rho e_{15}\Lambda\frac{\partial^2}{\partial t^2}, \end{aligned} \tag{2}$$

where $\Lambda = \partial^2/\partial r^2 + (1/r)\partial/\partial r + (1/r^2)\partial^2/\partial\theta^2$ is the two-dimensional Laplacian. The displacement functions Ψ and F must satisfy the following two equations:

$$\left(c_{66}^{\rho}\Lambda + c_{44}^{Pi}\frac{\partial^2}{\partial z^2} - \rho^{Pi}\frac{\partial^2}{\partial t^2}\right)\psi = 0, \qquad L_0 F = 0, \tag{3}$$

$$\begin{aligned} L_0 = {} & a_4\Lambda\Lambda\Lambda + \left(a_3\frac{\partial^2}{\partial z^2} + a_6\frac{\partial^2}{\partial t^2}\right)\Lambda\Lambda \\ & + \left(a_2\frac{\partial^4}{\partial z^4} + a_5\frac{\partial^4}{\partial t^4} + a_7\frac{\partial^4}{\partial z^2\partial t^2}\right)\Lambda + a_1\frac{\partial^6}{\partial z^6} \\ & + a_8\frac{\partial^6}{\partial z^4\partial t^2} + a_9\frac{\partial^6}{\partial z^2\partial t^4}. \end{aligned} \tag{4}$$

Here a_n $(n = 1, 2, \ldots, 9)$ can be expressed in terms of elastic constants c_{ij}^{Pi}, dielectric constants ε_{ij}, and piezoelectric coefficients e_{ij} as follows:

$$\begin{aligned}
a_1 &= c_{44}^{Pi}\left(e_{33}^2 + c_{33}^{Pi}\varepsilon_{33}\right),\\
a_4 &= c_{11}^{Pi}\left(e_{15}^2 + c_{44}^{Pi}\varepsilon_{11}\right), \qquad a_5 = \rho^2\varepsilon_{11},\\
a_2 &= c_{33}^{Pi}\left[c_{44}^{Pi}\varepsilon_{11} + \left(e_{15}+e_{31}\right)^2\right]\\
&\quad + \varepsilon_{33}\left[c_{11}^{Pi}c_{33}^{Pi} + c_{44}^2 - \left(c_{11}^{Pi}+c_{44}^{Pi}\right)^2\right]\\
&\quad + e_{33}\left[2c_{44}^{Pi}e_{15} + c_{11}^{Pi}e_{33} - 2\left(c_{13}^{Pi}+c_{44}^{Pi}\right)\left(e_{15}+e_{31}\right)\right],\\
a_3 &= c_{44}^{Pi}\left[c_{11}^{Pi}\varepsilon_{33} + \left(e_{15}+e_{31}\right)^2\right]\\
&\quad + \varepsilon_{11}\left[c_{11}^{Pi}c_{33} + c_{44}^2 - \left(c_{13}^{Pi}+c_{44}^{Pi}\right)^2\right]\\
&\quad + e_{15}\left[2c_{11}^{Pi}e_{33} + c_{44}^{Pi}e_{15} - 2\left(c_{13}^{Pi}+c_{44}^{Pi}\right)\left(e_{15}+e_{31}\right)\right],\\
a_6 &= -\rho\left[e_{15}^2 + \left(c_{11}^{Pi}+c_{44}^{Pi}\right)\varepsilon_{11}\right],\\
a_8 &= -\rho\left[e_{33}^2 + \left(c_{44}^{Pi}+c_{33}^{Pi}\right)\varepsilon_{33}\right], \qquad a_9 = \rho^2\varepsilon_{33},\\
a_7 &= -\rho\left[2e_{15}e_{33} + \left(c_{44}^{Pi}+c_{33}^{Pi}\right)\varepsilon_{11} + \left(c_{11}^{PI}+c_{44}^{Pi}\right)\varepsilon_{33}\right.\\
&\quad \left. + \left(e_{15}+e_{31}\right)^2\right].
\end{aligned} \tag{5}$$

The circular cylindrical coordinates as well as a circular cylindrical panel with outer radius b^{Pi}, inner radius a^{Pi}, circular center angle α^{Pi}, and length L^{Pi} are shown in Figure 1. If the panel is vibrating with a resonant frequency ω, the displacement functions can be assumed as

$$\begin{aligned}
F &= \frac{r_0^5}{c_{11}\varepsilon_{33}} P\left(\xi^P\right)\Theta\left(\mu\theta\right) Z\left(\beta\zeta^P\right) e^{i\omega t},\\
\psi &= r_0^2 P_4\left(\xi^P\right)\Theta'\left(\mu\theta\right) Z'\left(\beta\zeta^P\right) e^{i\omega t},
\end{aligned} \tag{6}$$

where $\xi^{Pi} = r^{Pi}/R^{Pi}$, $\zeta^{Pi} = z^{Pi}/L^{Pi}$ are the dimensionless coordinates in r and z directions and $\Theta'(\mu\theta^{Pi})$ and $Z'(\beta\zeta^{Pi})$ denote the derivation of $\Theta(\mu\theta^{Pi})$ with respect to $\mu\theta^{Pi}$ and the derivation of $Z(\beta\zeta^{Pi})$ with respect to $\beta\zeta^{Pi}$, respectively. In addition,

$$\begin{aligned}
\Theta\left(\mu\theta\right) &= C_1\cos\left(\mu\theta\right) + C_2\sin\left(\mu\theta\right),\\
Z\left(\beta\zeta\right) &= C_3\sin\left(\beta\zeta\right) + c_4\cos\left(\beta\zeta\right),
\end{aligned} \tag{7}$$

where C_m $(m = 1, 2, 3, 4)$ are constants. Substitution of (6) into (3) yields

$$\left(\Delta + k_4^2\right) P_4\left(\xi\right) = 0, \tag{8}$$

$$\left(\Delta + k_1^2\right)\left(\Delta + k_2^2\right)\left(\Delta + k_3^2\right) P_4\left(\xi\right) = 0, \tag{9}$$

where $\Delta = \partial^2/\partial(\xi^{Pi})^2 + (1/\xi^{Pi})\partial/\partial(\xi^{Pi}) - \mu^2/(\xi^{Pi})^2$ and

$$\begin{aligned}
k_4^2 &= \frac{\Omega^2 c_{11}^{pi}}{c_{66}^{pi}} - \frac{\gamma^2 c_{44}^{pi}}{c_{66}^{pi}},\\
\left(\Omega^{Pi}\right)^2 &= \frac{\rho^{Pi}\omega^2 r_0^2}{c_{11}}, \quad \gamma = \beta t_1, \quad t_1 = \frac{r_0}{h_0}
\end{aligned} \tag{10}$$

and $(k_m^{Pi})^2$, $(m = 1, 2, 3)$ (assuming $\mathrm{Re}[k_m^{Pi}] \geq 0$) are the eigenvalues of the following equation:

$$\begin{aligned}
&\bar{a}_4 k^6 + \left(\bar{a}_6\left(\Omega^{Pi}\right)^2 + \bar{a}_3\gamma^2\right)k^4\\
&\quad + \left(\bar{a}_2\gamma^4 + \bar{a}_7\gamma^2\left(\Omega^{Pi}\right)^2 + \bar{a}_5\left(\Omega^{Pi}\right)^4\right)k^2\\
&\quad + \left(\bar{a}_1\gamma^6 + \bar{a}_8\gamma^4\left(\Omega^{Pi}\right)^2 + \gamma^2\left(\Omega^{Pi}\right)^4\right) = 0
\end{aligned} \tag{11}$$

in which

$$\begin{aligned}
\bar{a}_n &= \frac{a_n}{\left(\left(c_{11}^{Pi}\right)^2\varepsilon_{33}\right)}, \quad (n = 1, 2, 3, 4),\\
\bar{a}_n &= \frac{a_n}{\left(\rho c_{11}^{Pi}\varepsilon_{33}\right)}, \quad (n = 6, 7, 8),\\
\bar{a}_5 &= \frac{a_5}{\left(\left(\rho^{Pi}\right)^2\varepsilon_{33}\right)}.
\end{aligned} \tag{12}$$

The solution of (9) can be assumed as

$$P\left(\xi\right) = P_1\left(\xi\right) + P_2\left(\xi\right) + P_3\left(\xi\right), \tag{13}$$

where $P_m(\xi^{Pi})$ is obtained as [18].

Substituting (6) into (1) gives the mechanical displacements and electric potential as follows:

$$u_r^{pi} = -r_0\left[\frac{\mu}{\xi}P_4\left(\xi\right) + \sum_{m=1}^{3}\alpha_{1m}P_m'\left(\xi\right)\right]\Theta\left(\mu\theta\right) Z'\left(\beta\zeta\right) e^{i\omega t}, \tag{14}$$

$$u_\theta^{pi} = -r_0\left[P_4'\left(\xi\right) + \frac{\mu}{\xi}\sum_{m=1}^{3}\alpha_{1m}P_m\left(\xi\right)\right]\Theta'\left(\mu\theta\right) Z'\left(\beta\zeta\right) e^{i\omega t}, \tag{15}$$

$$w^{pi} = r_0\left[\sum_{m=1}^{3}\alpha_{2m}P_m\left(\xi\right)\right]\Theta\left(\mu\theta\right) Z\left(\beta\zeta\right) e^{i\omega t}, \tag{16}$$

$$\Phi = r_0\sqrt{\frac{c_{11}^{pi}}{\varepsilon_{33}}}\left[\sum_{m=1}^{3}\alpha_{3m}P_m\left(\xi\right)\right]\Theta\left(\mu\theta\right) Z\left(\beta\zeta\right) e^{i\omega t}, \tag{17}$$

where

$$\begin{aligned}
\alpha_{1m} &= -\left(\left[\left(c_{13}^{Pi}+c_{44}\right)\left(\varepsilon_{11}k_m^2+\varepsilon_{33}\gamma^2\right)\right.\right.\\
&\qquad\left.\left.+\left(e_{15}+e_{31}\right)\left(e_{15}k_m^2+e_{33}\gamma^2\right)\right]\gamma\right)\\
&\qquad\times\left(c_{11}^{Pi}\varepsilon_{33}\right)^{-1},\\
\alpha_{2m} &= \left(\left[\left(c_{11}^{Pi}k_m^2+c_{44}^{Pi}\gamma^2-c_{11}^{Pi}\Omega_1^2\right)\left(\varepsilon_{11}k_m^2+\varepsilon_{33}\gamma^2\right)\right.\right.\\
&\qquad\left.\left.+\left(e_{15}+e_{31}\right)^2k_m^2\gamma^2\right]\right)\\
&\qquad\times\left(c_{11}^{Pi}\varepsilon_{33}\right)^{-1},\\
\alpha_{3m} &= \left(\left[\left(c_{11}^{Pi}k_m^2+c_{44}^{Pi}\gamma^2-c_{11}^{Pi}\Omega_1^2\right)\left(e_{15}k_m^2+e_{33}\gamma^2\right)\right.\right.\\
&\qquad\left.\left.-\left(c_{13}^{Pi}+c_{44}^{Pi}\right)\left(e_{15}+e_{31}\right)^2k_m^2\gamma^2\right]\right)\\
&\qquad\times\left(c_{11}^{Pi}\sqrt{c_{11}^{Pi}\varepsilon_{33}}\right)^{-1},\quad (m=1,2,3).
\end{aligned}\tag{18}$$

Utilizing the constitutive relations of piezoelectricity and (14)–(17), the stress components and electric displacement components can be derived as

$$\begin{aligned}
\sigma_r^{pi} &= \left\{\left(c_{12}^{pi}-c_{11}^{pi}\right)\left[\frac{\mu}{\xi}P_4'(\xi)-\frac{\mu}{\xi^2}P_4(\xi)\right]\right.\\
&\qquad+\left(c_{12}^{pi}-c_{11}^{pi}\right)\sum_{m=1}^{3}\alpha_{1m}P_m''(\xi)\\
&\qquad+\sum_{m=1}^{3}\left(c_{12}\alpha_{1m}k_m^2+c_{13}^{pi}\gamma\alpha_{2m}+e_{31}\sqrt{\frac{c_{11}^{pi}}{\varepsilon_{33}}}\gamma\alpha_{3m}\right)\\
&\qquad\left.\times P_m(\xi)\right\}\Theta(\mu\theta)Z'(\beta\zeta)e^{i\omega t},
\end{aligned}\tag{19}$$

$$\begin{aligned}
\sigma_\theta^{pi} &= \left\{\left(c_{11}^{pi}-c_{12}^{pi}\right)\left[\frac{\mu}{\xi}P_4'(\xi)-\frac{\mu}{\xi^2}P_4(\xi)\right]\right.\\
&\qquad+\left(c_{11}^{pi}-c_{12}^{pi}\right)\sum_{m=1}^{3}\alpha_{1m}P_m''(\xi)\\
&\qquad+\sum_{m=1}^{3}\left(c_{11}^{pi}\alpha_{1m}k_m^2+c_{13}^{pi}\gamma\alpha_{2m}+e_{31}\sqrt{\frac{c_{11}^{pi}}{\varepsilon_{33}}}\gamma\alpha_{3m}\right)\\
&\qquad\left.\times P_m(\xi)\right\}\Theta(\mu\theta)Z'(\beta\zeta)e^{i\omega t},
\end{aligned}\tag{20}$$

$$\begin{aligned}
\sigma_z^{pi} &= \sum_{m=1}^{3}\left[\left(c_{13}^{pi}\alpha_{1m}k_m^2+c_{33}^{pi}\gamma\alpha_{2m}+e_{33}\sqrt{\frac{c_{11}^{pi}}{\varepsilon_{33}}}\gamma\alpha_{3m}\right)\right.\\
&\qquad\left.\times P_m(\xi)\right]\Theta(\mu\theta)Z'(\beta\zeta)e^{i\omega t},
\end{aligned}\tag{21}$$

$$\begin{aligned}
\tau_{\theta z}^{pi} &= \left\{c_{44}^{pi}\gamma P_4'(\xi)\right.\\
&\qquad+\frac{\mu}{\xi}\sum_{m=1}^{3}\left[\left(c_{44}^{pi}\gamma\alpha_{1m}+c_{44}^{pi}\alpha_{2m}+e_{15}\sqrt{\frac{c_{11}^{pi}}{\varepsilon_{33}}}\alpha_{3m}\right)\right.\\
&\qquad\left.\left.\times P_m(\xi)\right]\right\}\Theta'(\mu\theta)Z(\beta\zeta)e^{i\omega t},
\end{aligned}\tag{22}$$

$$\begin{aligned}
\tau_{rz}^{pi} &= \left\{c_{44}^{pi}\gamma\frac{\mu}{\xi}Q(\xi)\right.\\
&\qquad+\left[\sum_{m=1}^{3}\left(c_{44}^{pi}\gamma\alpha_{1m}+c_{44}^{pi}\alpha_{2m}+e_{15}\sqrt{\frac{c_{11}^{pi}}{\varepsilon_{33}}}\alpha_{3m}\right)\right.\\
&\qquad\left.\left.\times p_M'(\xi)\right]\right\}\Theta(\mu\theta)Z(\beta\zeta)e^{i\omega t},
\end{aligned}\tag{23}$$

$$\begin{aligned}
\tau_{r\theta}^{pi} &= c_{66}\left[-k_4^2P_4(\xi)-2P_4''(\xi)\right.\\
&\qquad\left.+\frac{2\mu}{\xi^2}\sum_{m=1}^{3}\alpha_{1m}P_m(\xi)-\frac{2\mu}{\xi}\sum_{m=1}^{3}\alpha_{1m}p_M'(\xi)\right]\\
&\qquad\times\Theta'(\mu\theta)Z'(\beta\zeta)e^{i\omega t},
\end{aligned}\tag{24}$$

$$\begin{aligned}
D_r^{pi} &= \left\{e_{15}\gamma\frac{\mu}{\xi}P_4(\xi)\right.\\
&\qquad+\left[\sum_{m=1}^{3}\left(e_{15}\gamma\alpha_{1m}+e_{15}\alpha_{2m}+\varepsilon_{11}\sqrt{\frac{c_{11}^{pi}}{\varepsilon_{33}}}\alpha_{3m}\right)\right.\\
&\qquad\left.\left.\times p_M'(\xi)\right]\right\}\Theta(\mu\theta)Z(\beta\zeta)e^{i\omega t},
\end{aligned}\tag{25}$$

$$D_\theta^{pi} = \left\{ e_{15}\gamma P_4'(\xi) + \frac{\mu}{\xi}\left[\sum_{m=1}^{3}\left(e_{15}\gamma\alpha_{1m} + e_{15}\alpha_{2m} + \varepsilon_{11}\sqrt{\frac{c_{11}^{pi}}{\varepsilon_{33}}}\alpha_{3m}\right) \times P_m(\xi)\right]\right\} \Theta'(\mu\theta) Z(\beta\zeta) e^{i\omega t}, \tag{26}$$

$$D_z^{pi} = \left[\sum_{m=1}^{3}\left(e_{31}\alpha_{1m}k_m^2 + e_{33}\gamma\alpha_{2m} - \sqrt{c_{11}^{pi}\varepsilon_{33}}\gamma\alpha_{3m}\right)P_m(\xi)\right] \times \Theta(\mu\theta) Z'(\beta\zeta) e^{i\omega t}. \tag{27}$$

2.2. Boundary Conditions. The piezoelectric panel has 8 boundary conditions consist of 6 mechanical and 2 electrical ones.

By considering generalized simply support boundary conditions at $\theta^i = 0$ and $\theta^i = \alpha$ and $(i = Pi)$ we will have

$$w^i = u_r^i = 0, \quad \sigma_\theta^i = 0 \quad (i = Pi). \tag{28}$$

Note that for piezoelectric layers the following condition is added

$$\phi = 0. \tag{29}$$

One can take

$$C_1^i = 0, \qquad C_2^i = 1, \qquad \mu = \frac{(2m+1)\pi}{2\alpha}, \quad m = 0, 1, 2, \ldots. \tag{30}$$

And by considering generalized simply support boundary conditions at $\zeta^i = 0$ and $\zeta^i = 1$ $(i = Pi)$ we will have

$$u_r^i = u_\theta^i = 0, \quad \sigma_z^i = 0 \quad (i = Pi). \tag{31}$$

And for piezoelectric layers the following condition is added

$$D_z = 0. \tag{32}$$

One can take

$$C_3^i = 0, \qquad C_4^i = 1, \qquad \beta = n\pi, \quad n = 0, 1, 2, \ldots. \tag{33}$$

Without loss of generality, we suppose that external force acts on the outer surface of the actuator and inner surface of sensor has free boundary condition. So, we have

$$\begin{aligned} &\sigma_r^{Pi} = P, \qquad \tau_{r\theta}^{Pi} = \tau_{rz}^{Pi} = 0, \qquad \phi = I \quad \text{at } r = r_4, \\ &\sigma_r^{Pi} = \tau_{r\theta}^{Pi} = \tau_{rz}^{Pi} = 0, \qquad \phi = 0 \quad \text{at } r = r_1. \end{aligned} \tag{34}$$

For obtaining steady state frequency response of the cylindrical panel under a harmonic external excitation, we must solve the following matrix equation:

$$[T]_{m\times n}\{X\}_{n\times 1} = \{F\}_{m\times 1}, \tag{35}$$

where $[T]_{m\times n}$ is the coefficient matrix. Consider

$$\{X\}_{n\times 1} = [A_1 \;\; B_1 \;\; A_2 \;\; B_2 \;\; A_3 \;\; B_3 \;\; A_4 \;\; B_4] \tag{36}$$

and A_i, B_i, $i = 1, 2, 3, 4$ are the unknown constants that are in (19)–(27).

The vector $\{F\}_{m\times 1}$ denotes the force vector that acts on the structure. This force consists of the surface force that is considered as disturbance and has the breed of mechanical force such as wind effect. The effect of controller unit in the dynamic response of the piezo-panel is considered as an external electrical potential applied on the upper surface of the panel. These two external forces acted on the structure independently; however summation of their effects on the whole structure is the same as the case that both of them act on the structure simultaneously. So

$$\begin{aligned} \{F\}_{n\times 2} &= [F_1 \;\; F_2], \\ \{F_1\}_{n\times 1} &= [0 \;\; 0 \;\; 0 \;\; 0 \;\; 0 \;\; 0 \;\; I(r_0, \theta, z, \omega) \;\; 0]^T, \\ \{F_2\}_{n\times 1} &= [P(r_0, \theta, z, \omega) \;\; 0 \;\; 0 \;\; 0 \;\; 0 \;\; 0 \;\; 0 \;\; 0]^T, \end{aligned} \tag{37}$$

where $P(r_0, \theta, z, \omega)$ acting over the area $(L_q \le x \le L_q + a_q)$ on its top surface, while it is traction-free at the bottom surface. Thus

$$\begin{aligned} P(r, \theta, z, \omega) &= \sum_{n=-\infty}^{\infty}\sum_{m=0}^{\infty} p_{nm}(r, \omega) \operatorname{Sin}\left(\frac{m\pi z}{l}\right) e^{i(n\theta + \omega t)}, \\ I(r, \theta, z, \omega) &= \sum_{n=-\infty}^{\infty}\sum_{m=0}^{\infty} \iota_{nm}(r, \omega) \operatorname{Sin}\left(\frac{m\pi z}{l}\right) e^{i(n\theta + \omega t)}, \end{aligned} \tag{38}$$

where

$$\begin{aligned} p_{nm}(r, \omega) &= \begin{cases} A_{nm}(\omega) J_n(Kr), & K^2 > 0, \\ A_{nm}(\omega) r^n, & K^2 = 0, \\ A_{nm}(\omega) I_n(\overline{K}r), & K^2 = -\overline{K}^2 < 0, \end{cases} \\ \iota_{nm}(r, \omega) &= \begin{cases} B_{nm}(\omega) J_n(Kr), & K^2 > 0, \\ B_{nm}(\omega) r^n, & K^2 = 0, \\ B_{nm}(\omega) I_n(\overline{K}r), & K^2 = -\overline{K}^2 < 0 \end{cases} \end{aligned} \tag{39}$$

in which $K = \sqrt{k^2 - (\pi m/L)^2}$ and J_n and I_n denote the standard and modified cylindrical Bessel functions of first kind, respectively, and $A_{nm}(\omega)$ and $B_{nm}(\omega)$ are the amplitude of the applied forces. Substituting (21), (25), and (26) into the mechanical condition (39) and substituting (27) or (19) into the electric condition (40) yields homogeneous equations with respect to coefficients A_m and B_m, $(m = 1, 2, 3, 4)$. After finding these unknown constants that are functions of

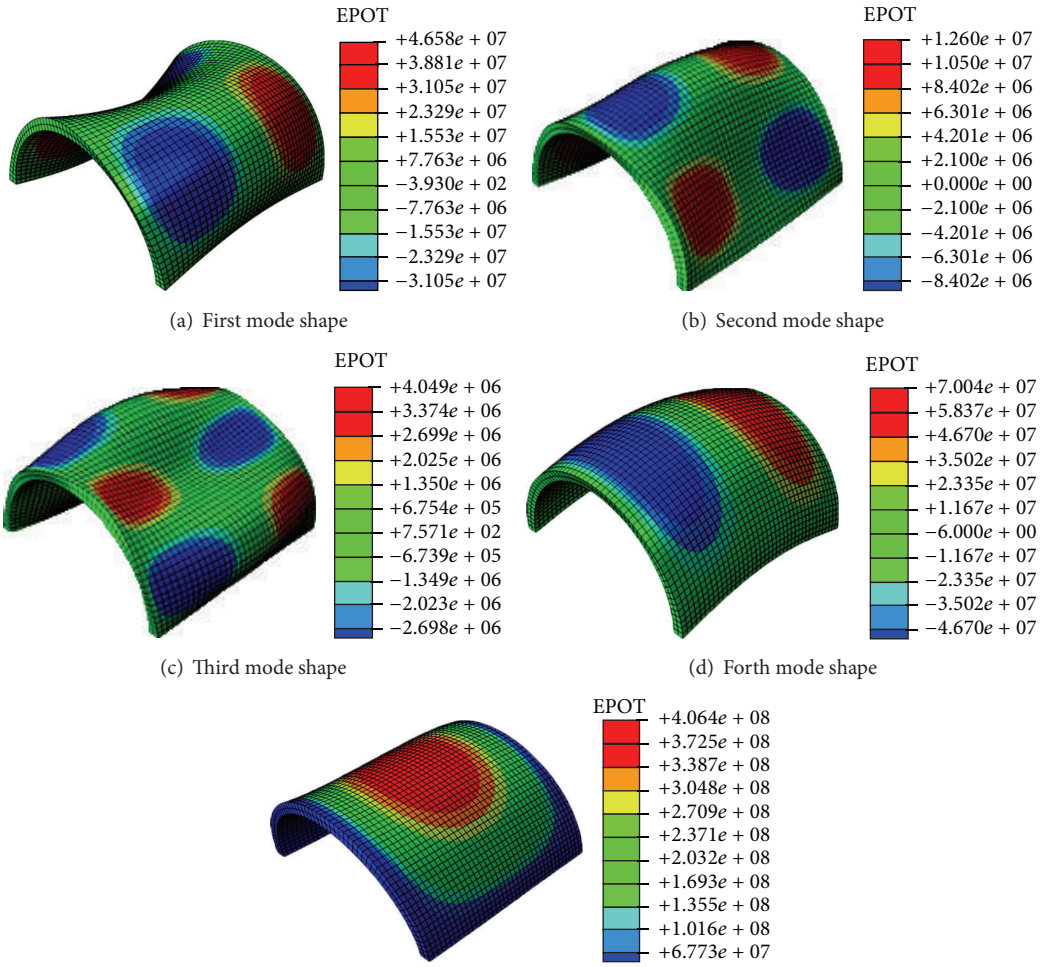

(a) First mode shape (b) Second mode shape

(c) Third mode shape (d) Forth mode shape

(e) Fifth mode shape

Figure 2: Mode shapes of the five first natural frequencies.

m, n by replacing them in the displacement and stress and electric displacement of corresponding equations (19)–(27), all of the system variables will be determined easily. However for control purposes the voltage obtained from the piezolayer as a sensor is the measured output and it is calculated as

$$q = \int_{\text{Area}} \overline{D} \cdot dA_{\text{Area}}, \tag{40}$$

where $\overline{D} = D_r\hat{r} + D_\theta\hat{\theta} + D_z\hat{z}$ is the electric displacement vector in the principle cylindrical coordinates. Area in the integration stands for the place that the sensor layer is active and voltage (control output) is measured and $dA_{\text{Area}} = (dz \times d\theta)\hat{r}$ which simplifies the above equation as

$$q_r = \int_{\theta_1^s}^{\theta_2^s} \int_{z_1^s}^{z_2^s} D_r dz\, d\theta. \tag{41}$$

Moreover, by considering the piezoelectric sensor layer as an electric capacity $V = q/c_{PS}$, one can obtain

$$V = \frac{1}{c_{PS}} \int_{\theta_1^s}^{\theta_2^s} \int_{z_1^s}^{z_2^s} D_r dz\, d\theta, \tag{42}$$

where c_{PS} is the capacitance of the piezoelectric sensor.

Table 1: First three nondimensional natural frequencies.

S		$\mu = 1.8$			$\mu = 0.9$	
0.1	0.9366	1.8562	2.3634	0.5178	1.4580	1.8160
0.2	0.8266	1.7995	2.3514	0.5109	1.4144	1.8214
0.3	0.7214	1.7650	2.3616	0.5043	1.3565	1.8434
0.4	0.6271	1.7193	2.3889	0.4975	1.2960	1.8666
0.5	0.5408	1.6549	2.4273	0.4906	1.2385	1.8741

3. Results and Discussion

Table 1 shows the first three nondimensional natural frequencies of some panels by different geometries. Mode shapes of the five first natural frequencies are shown in Figure 2. The panel dynamic responses under the aforementioned inputs (dynamic excitation and electric excitation) are shown in Figure 3 and are compared by FEM results.

It is obvious that a good accommodation exist between analytical solution and FEM (ABAQUS) method. In addition, the dynamic response of the panel in 450 Hz is shown in

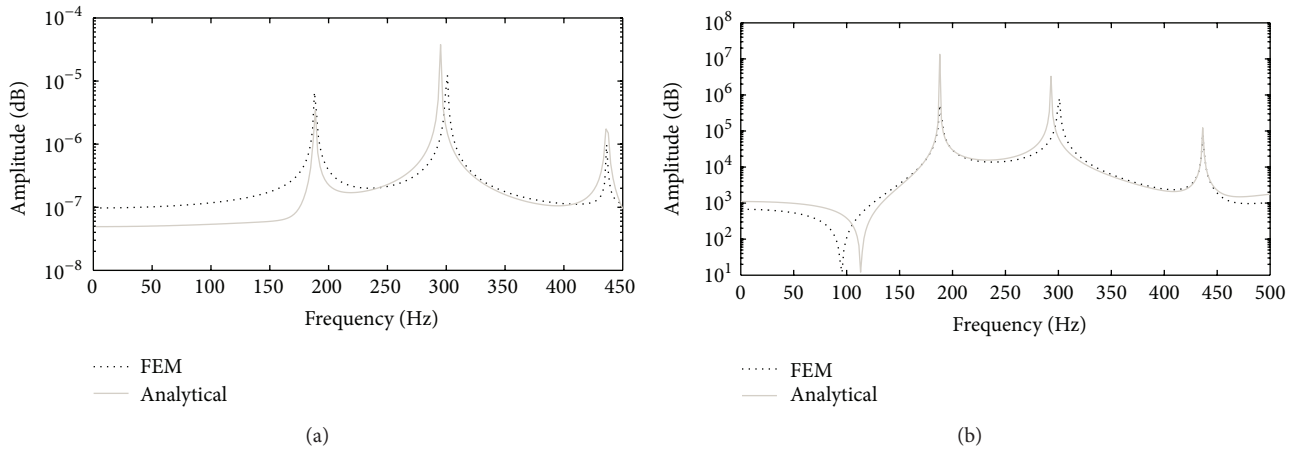

Figure 3: Panel dynamic response. (a) Mechanical excitation; (b) electrical excitation.

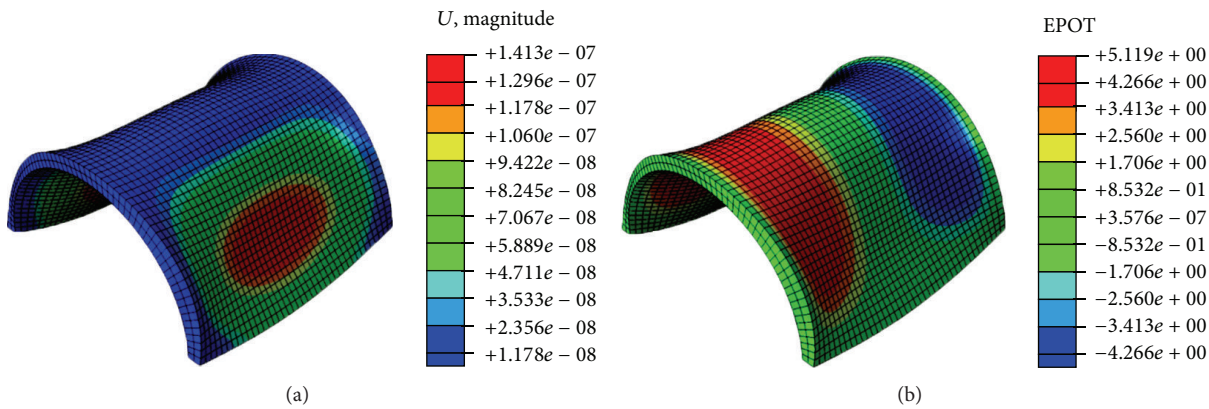

Figure 4: The dynamic response of the panel at 450 Hz due to (a) mechanical excitation; (b) electrical excitation.

Figure 4. It can be seen that the dominant mode shape in this frequency is the third mode shape.

4. Conclusion

Based on the general solution of the coupled equations for a piezoelectric media, the displacement functions are expanded in terms of trigonometric functions in z and θ directions. Three-dimensional exact solutions for the free vibration of a piezoelectric circular cylindrical panel are then obtained under several boundary conditions. Also the forced vibration is solved. The natural frequencies are compared with previous works. The dynamic responses with mechanical and electrical excitation are validated with FEM and the mode shapes are shown.

Conflict of Interests

The authors declare that there is no conflict of interests regarding the publication of this paper.

References

[1] J. F. Haskins and J. L. Walsh, "Vibrations of ferroelectric cylindrical shells with transverse isotropy: I. Radially polarized case," *The Journal of the Acoustical Society of America*, vol. 29, no. 6, pp. 729–734, 1975.

[2] G. E. Martin, "Vibrations of longitudinally polarized ferroelectric cylindrical tubes," *The Journal of the Acoustical Society of America*, vol. 35, no. 4, pp. 510–520, 1963.

[3] D. S. Drumheller and A. Kalnins, "Dynamic shell theory for ferroelectric ceramics ," *The Journal of the Acoustical Society of America*, vol. 47, no. 5, pp. 1343–1353, 1970.

[4] J. A. Burt, "The electroacoustic sensitivity of radially polarized ceramic cylinders as a function of frequency," *The Journal of the Acoustical Society of America*, vol. 64, no. 6, pp. 1640–1644, 1978.

[5] H. S. Tzou and J. P. Zhong, "A linear theory of piezoelastic shell vibrations," *Journal of Sound and Vibration*, vol. 175, no. 1, pp. 77–88, 1994.

[6] D. D. Ebenezer and P. Abraham, "Eigenfunction analysis of radially polarized piezoelectric cylindrical shells of finite length," *The Journal of the Acoustical Society of America*, vol. 102, no. 3, pp. 1549–1558, 1997.

[7] C. V. Stephenson, "Radial vibrations in short, hollow cylinders of barium titanate," *The Journal of the Acoustical Society of America*, vol. 28, no. 1, pp. 51–56, 1956.

[8] C. V. Stephenson, "Higher modes of radial vibrations in short, hollow cylinders of barium titanate," *The Journal of the Acoustical Society of America*, vol. 28, no. 5, pp. 928–929, 1956.

[9] N. T. Adelman, Y. Stavsky, and E. Segal, "Axisymmetric vibrations of radially polarized piezoelectric ceramic cylinders," *Journal of Sound and Vibration*, vol. 38, no. 2, pp. 245–254, 1975.

[10] N. T. Adelman, Y. Stavsky, and E. Segal, "Radial vibrations of axially polarized piezoelectric ceramic cylinders," *The Journal of the Acoustical Society of America*, vol. 57, no. 2, pp. 356–360, 1975.

[11] H. S. Paul, "Vibrations of circular cylindrical shells of piezoelectric silver iodide crystals," *The Journal of the Acoustical Society of America*, vol. 40, no. 5, pp. 1077–1080, 1966.

[12] H. S. Paul and M. Venkatesan, "Vibrations of a hollow circular cylinder of piezoelectric ceramics," *The Journal of the Acoustical Society of America*, vol. 82, no. 3, pp. 952–956, 1987.

[13] H.-J. Ding, W.-Q. Chen, Y.-M. Guo, and Q.-D. Yang, "Free vibrations of piezoelectric cylindrical shells filled with compressible fluid," *International Journal of Solids and Structures*, vol. 34, no. 16, pp. 2025–2034, 1997.

[14] Z. Yang, J. Yang, Y. Hu, and Q.-M. Wang, "Vibration characteristics of a circular cylindrical panel piezoelectric transducer," *IEEE Transactions on Ultrasonics, Ferroelectrics, and Frequency Control*, vol. 55, no. 10, pp. 2327–2335, 2008.

[15] S. Li, J. Qiu, H. Ji, K. Zhu, and J. Li, "Piezoelectric vibration control for all-clamped panel using DOB-based optimal control," *Mechatronics*, vol. 21, no. 7, pp. 1213–1221, 2011.

[16] N. Kumar and S. P. Singh, "Vibration control of curved panel using smart damping," *Mechanical Systems and Signal Processing*, vol. 30, pp. 232–247, 2012.

[17] H. J. Ding, B. Chen, and J. Liang, "General solutions for coupled equations for piezoelectric media," *International Journal of Solids and Structures*, vol. 33, no. 16, pp. 2283–2298, 1996.

[18] H. J. Ding, R. Q. Xu, and W. Q. Chen, "Free vibration of transversely isotropic piezoelectric circular cylindrical panels," *International Journal of Mechanical Sciences*, vol. 44, no. 1, pp. 191–206, 2002.

Hindawi Publishing Corporation
Shock and Vibration
Volume 2014, Article ID 676497, 5 pages
http://dx.doi.org/10.1155/2014/676497

Research Article

Adaptive Equalizer Using Selective Partial Update Algorithm and Selective Regressor Affine Projection Algorithm over Shallow Water Acoustic Channels

Masoumeh Soflaei and Paeiz Azmi

Faculty of Electrical and Computer Engineering, Tarbiat Modares University, P.O. Box 14115-194, Tehran, Iran

Correspondence should be addressed to Paeiz Azmi; pazmi@modares.ac.ir

Received 4 October 2012; Accepted 19 November 2012; Published 25 May 2014

Academic Editor: Hamid Ahmadian

One of the most important problems of reliable communications in shallow water channels is intersymbol interference (ISI) which is due to scattering from surface and reflecting from bottom. Using adaptive equalizers in receiver is one of the best suggested ways for overcoming this problem. In this paper, we apply the family of selective regressor affine projection algorithms (SR-APA) and the family of selective partial update APA (SPU-APA) which have low computational complexity that is one of the important factors that influences adaptive equalizer performance. We apply experimental data from Strait of Hormuz for examining the efficiency of the proposed methods over shallow water channel. We observe that the values of the steady-state mean square error (MSE) of SR-APA and SPU-APA decrease by 5.8 (dB) and 5.5 (dB), respectively, in comparison with least mean square (LMS) algorithm. Also the families of SPU-APA and SR-APA have better convergence speed than LMS type algorithm.

1. Introduction

Underwater acoustic communications suffer from doppler shifts, noise, scattering from surface, and reflecting from bottom that cause multipath spread especially in shallow water channels. Multipath spread causes intersymbol interference (ISI), which influences reliable transmission in underwater acoustic communications. One of the best ways suggested for overcoming this effect is using adaptive equalization methods in receivers. Some factors such as adaptive filter and adaptive algorithms influence this method, so it is important to choose adaptive algorithms with low computational complexity and more ability for tracking changes in channel.

Least mean square (LMS) algorithm is the most popular because of its simplicity in computations and implementation that is used by Stojanovic et al. [1, 2] in underwater acoustic communication. Recursive least square (RLS) due to the fastest convergence speed is the best adaptive filter algorithm used by Zheng et al. [3] and Freitag et al. [4] in this channel in spite of its computational complexity. Computational complexity in some algorithms such as RLS is one of the main problems, so some other algorithms such as selective regressor affine projection algorithm (SR-APA) and selective partial update (SPU) that have good tradeoff between computational complexity and convergence speed are suggested. In SPU algorithm, the blocks of filter coefficients have been updated in every iteration that is selected by special criteria. Important examples of this algorithm are different types of selective partial update normalized least mean square (SPU-NLMS) [5–7] such as MAX-NLMS [8], N-MAX NLMS [9] (the number of filter coefficients to be updated is N), and the family of SPU affine projection algorithms (SPU-APA) [10]. In selective regressor algorithm approach, a subset of input regressors should be selected by selection criteria in every iteration. In comparison with LMS, the value of the steady-state mean square error (MSE) of SR-APA by selecting 3 of 4 input regressors decreases by 5.8 (dB) and the value of the steady-state MSE of SPU-APA by selecting 3 of 4 blocks of filter coefficients decreases by 5.5 (dB).

In this paper, our objective is to apply SPU-APA and SR-APA algorithms that have a good tradeoff between convergence speed and computational complexity for underwater

acoustic communications. Also, we show the result of using the performance of these algorithms in comparison with RLS and NLMS.

This paper is organized as follows: in the next section, we present the basis of APA, SR-APA, and SPU-APA. In Section 3, we introduce a model for shallow water channel. Section 4 presents the computational complexity of different algorithms that are introduced. We show the simulation results in Section 5, and we conclude the paper in Section 6.

2. Basis of Affine Projection Algorithm, Selective Regressor Affine Projection Algorithm (SR-APA), and Selective Partial Update Affine Projection Algorithm (SPU-APA)

2.1. APA. In this paper, x, d, and e denote input, desired, and output error signals, respectively. $\mathbf{h}$ is the filter coefficients vector with order $M \times 1$ and μ is the step size. The family of affine projection algorithms (APA) is derived by solving

$$\text{Min} \left\|\mathbf{h}(n+1) - \mathbf{h}(n)\right\|^2 \tag{1}$$

subject to $\mathbf{d}(n) = \mathbf{X}^T(n)\mathbf{h}(n+1)$. Lagrange multipliers method leads to the following recursion:

$$\mathbf{h}(n+1) = \mathbf{h}(n) + \mu \mathbf{C}(n)\mathbf{X}(n)\mathbf{W}(n)\mathbf{e}(n), \tag{2}$$

where $\mathbf{e}(n) = \mathbf{d}(n) - \mathbf{X}^T(n)\mathbf{h}(n)$.

$\mathbf{h}$ is the $M \times 1$ column vector of filter coefficients, $\mathbf{X}$ is the $M \times P$ matrix of the input signal $\mathbf{X}(n) = [\mathbf{x}(n), \mathbf{x}(n-D), \ldots, \mathbf{x}(n-(P-1)D)]$, and $\mathbf{d}$ is a $P \times 1$ vector of desired signal $\mathbf{d}(n) = [d(n), d(n-D), \ldots, d(n-(P-1)D)]^T$. P must be a positive integer, and usually $P \leq M$. $\mathbf{C}(n)$ is equal to $\mathbf{I}$, and $\mathbf{W}(n) = (\mathbf{X}^T(n)\mathbf{X}(n))^{-1}$.

By substituting the parameters P and D and the matrices $\mathbf{C}$ and $\mathbf{W}$ from Table 1 in (2), we can acquire various types of conventional algorithms such as binormalized data reusing least mean square (BNDR-LMS), regularized APA, and the normalized LMS with orthogonal correction factor (NLMS-OCF) [11] that are various types of the affine projection's family. In Table 1, the parameter ε is the regularization parameter which is introduced for preventing division by zero, and μ is the step size that controls the convergence speed and steady-state mean square error.

If the filter coefficient equation is updated only once every K iterations, it is named partial rank algorithm (PRA) [12].

2.2. SR-APA. The filter coefficients update equation for SR-APA is given by [13]

$$\mathbf{h}(n+1) = \mathbf{h}(n) + \mu \mathbf{X}_G(n)\left(\mathbf{X}_G^T(n)\mathbf{X}_G(n)\right)^{-1}\mathbf{e}_G(n), \tag{3}$$

where $\mathbf{e}_G(n) = \mathbf{d}_G(n) - \mathbf{X}_G^T(n)\mathbf{h}(n)$.

$G = \{i_1, i_2, \ldots, i_q\}$ denotes a q-subset (subset with q members) of the set $\{0, 1, \ldots, P-1\}$, and also $\mathbf{X}_G(n)$ and $\mathbf{d}_G(n)$ are the $M \times q$ matrix of the input signal and the $q \times 1$ vector of the desired signal, respectively. They are defined as

$$\begin{aligned} \mathbf{X}_G(n) &= \left[\mathbf{x}(n-i_1D), \mathbf{x}(n-i_2D), \ldots, \mathbf{x}(n-i_qD)\right], \\ \mathbf{d}_G(n) &= \left[d(n-i_1D), d(n-i_2D), \ldots, d(n-i_qD)\right]^T. \end{aligned} \tag{4}$$

Table 1: Family of APA adaptive filter algorithms.

Algorithm	P	D	$\mathbf{C}(n)$	$\mathbf{D}(n)$
APA	$P \leq M$	$D = 1$	$\mathbf{I}$	$(\mathbf{X}^T(n)\mathbf{X}(n))^{-1}$
BNDR-LMS	$P = 2$	$D = 1$	$\mathbf{I}$	$(\mathbf{X}^T(n)\mathbf{X}(n))^{-1}$
R-APA	$P \leq M$	$D = 1$	$\mathbf{I}$	$(\varepsilon\mathbf{I} + \mathbf{X}^T(n)\mathbf{X}(n))^{-1}$
NLMS-OCF	$P \leq M$	$D \geq 1$	$\mathbf{I}$	$(\mathbf{X}^T(n)\mathbf{X}(n))^{-1}$

The indices of G are obtained by the following procedure.

(1) Compute the following values for $0 \leq i \leq P-1$:

$$\frac{e^2(n-iD)}{\left\|\mathbf{x}(n-iD)\right\|^2}, \tag{5}$$

where $\mathbf{e}(n) = [e(n), e(n-D), \ldots, e(n-(P-1)D)]^T$.

(2) Compute q largest values of (5) that corresponded to indices of G.

Setting $D = 1$ leads to SR-APA presented in [13]. By substituting the parameters D and P, various types of SR-APA and SR-BNDR-LMS, SR-NLMS-OCF can be established. The filter coefficient update for SR-APA can be represented as

$$\begin{aligned} \mathbf{h}(n+1) = \mathbf{h}(n) &+ \mu \mathbf{X}(n)\mathbf{B}(n) \\ &\times \left(\mathbf{B}^T(n)\mathbf{X}^T(n)\mathbf{X}(n)\mathbf{B}(n)\right)^{-1}\mathbf{B}^T(n)\mathbf{e}(n), \end{aligned} \tag{6}$$

where $\mathbf{B}(n) = \{\mathbf{1}_{i1}, \mathbf{1}_{i2}, \ldots, \mathbf{1}_{iq}\}$ is the $P \times q$ matrix and $\mathbf{1}_{iq} = [0, \ldots, 0, 1, 0, \ldots, 0]$ is the $P \times 1$ vector with the element 1 in the position i_q.

2.3. SPU-APA. We use the Lagrange multiplier method to solve the following optimization problem [6]:

$$\text{Min} \left\|\mathbf{h}_F(n+1) - \mathbf{h}_F(n)\right\|^2 \tag{7}$$

subject to $\mathbf{d}(n) = \mathbf{X}^T(n)\mathbf{h}(n+1)$. Recursive equation for updating filter coefficients can be written as

$$\mathbf{h}_F(n+1) = \mathbf{h}_F(n) + \mu \mathbf{X}_F(n)\left(\mathbf{X}_F^T(n)\mathbf{X}_F(n)\right)^{-1}\mathbf{e}(n). \tag{8}$$

$F = \{j_1, j_2, \ldots, j_S\}$ denotes the indices of the S blocks out of B blocks that should be updated at every adaptation, $\mathbf{X}_F(n) = [\mathbf{X}_{j_1}^T(n), \mathbf{X}_{j_2}^T(n), \ldots, \mathbf{X}_{j_S}^T(n)]^T$ is $SL \times P$ matrix, and $\mathbf{X}_i(n) = [\mathbf{x}_i(n), \mathbf{x}_i(n-D), \ldots, \mathbf{x}_i(n-(P-1)D)]_{L\times P}$.

The indices of F are obtained by the following procedure.

(1) Compute the following values for $1 \leq i \leq B$:

$$\text{Tr}\left(\mathbf{X}_i^T(n)\mathbf{X}_i(n)\right). \tag{9}$$

(2) Compute S largest values of (9) that corresponded to indices of F.

Table 2: Explanation of computational complexity of the APA, SR-APA, and SPU-APA.

Algorithm	Multiplications	Divisions	Additional multiplications	Comparisons
APA	$(P^2 + 2P)M + P^3 + P^2$			
SR-APA	$(q^2 + 2q)M + q^3 + q^2$	P	$(P - q)M + P + 1$	$P\log_2 q + O(P)$
SPU-APA	$(P^2 + 2P)SL + P^3 + P^2$		1	$B\log_2 S + O(B)$

3. Channel Modelling

Different types of attenuations such as scattering from surface, reflecting from bottom, frequency absorption, and noise influence the sound waves propagation and decrease the energy of wave in shallow water channel. Scattering from surface and reflecting from bottom are two important events that influence reliable transmission in underwater acoustic communication channels. For modelling of the scattering from surface, we use Rayleigh surface loss model. We use Strait of Hormuz conditions and Hamilton-Backman model for counting losses due to reflect from bottom. Loss due to frequency absorption is another type of loss that happened in underwater acoustic propagation. This phenomenon happens in some material such as magnesium sulphate ($MgSO_4$) and boric acid ($B(OH)_3$) [14, 15].

Noise in this channel is the combination of ambient noises such as turbulences, shipping noise, thermal noise, and sea-state noise that is dependent on frequency and can be described by Gaussian statistics. For studying multipath propagation in this channel, we consider ray theory model [16] as a mathematical model. The channel impulse response which is obtained from this channel is shown in Figure 1. We can conclude that after sixth-path channel pattern we have strong attenuation, so there is not a signal reception. We can consider sixth-path channel pattern for this channel.

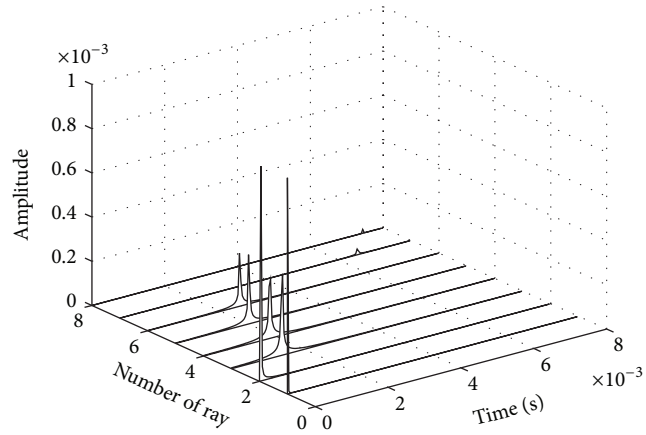

Figure 1: Impulse response of channel used in this paper.

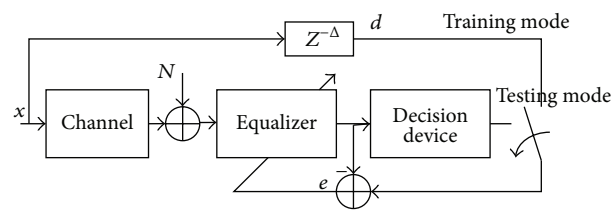

Figure 2: Structure of an adaptive channel equalizer.

4. Computational Complexity

The computational complexity of the introduced algorithms is shown in Table 2. This table shows the number of multiplications, divisions, and comparisons at each iteration. The computational complexity of APA and that of SR-APA are from [13]. By comparing computational complexity between APA and SPU-APA, we can see the reduction in multiplications equal to $(P^2 + 2P)(M - SL)$. Also, SPU-APA needs 1 additional multiplication and comparison $B\log_2 S + O(B)$.

5. Simulation and Results

In the channel model, the channel depth is 40 meters. Transmitter and receiver are placed in depth of 5 and 10 meters from the surface, respectively, and the distance between them is 1 Km. We use QPSK modulation with bandwidth of 5 KHz, carrier frequency of 23 KHz, and SNR of 20 dB. Also, channel characteristics are based on the data measured in the Strait of Hormuz by NOAA submarine during August of 2009.

We use the structure of Figure 2 for equalizer. In this structure, we have two modes, training and testing modes with 2500 and 5000 samples, respectively, and also the number of filter taps is 240 and $\Delta = 120$. For minimizing bit error rate, the step sizes of LMS, NLMS, and APA were set to 10^{-9}, 0.5, and 0.1, and the order of APA was equal to 4. In SR-APA, q parameter is the number of input regressors that have been selected. It can be changed from 1 to 4. In SPU-APA algorithm, the number of total blocks is 4, and S denotes the number of blocks that must be selected by (9).

Figure 3 shows the learning curve of LMS, APA, and SR-APA. We can observe that APA and SR-APA have faster convergence rate than LMS. Figure 4 shows the learning curve of LMS, APA, and SPU-APA. The SR-APA and SPU-APA have close convergence rate to APA with lower computational complexity than APA. In comparison with LMS, the steady-state mean square error (MSE) of SR-APA by selecting 3 of 4 input regressors decreases by 5.8 (dB), and the steady-state MSE of SPU-APA by selecting 3 of 4 blocks of filter coefficients decreases by 5.5 (dB).

Symbol error rate (SER) curves versus signal-to-noise ratio have been shown in Figures 5 and 6 for APA, SPU-APA,

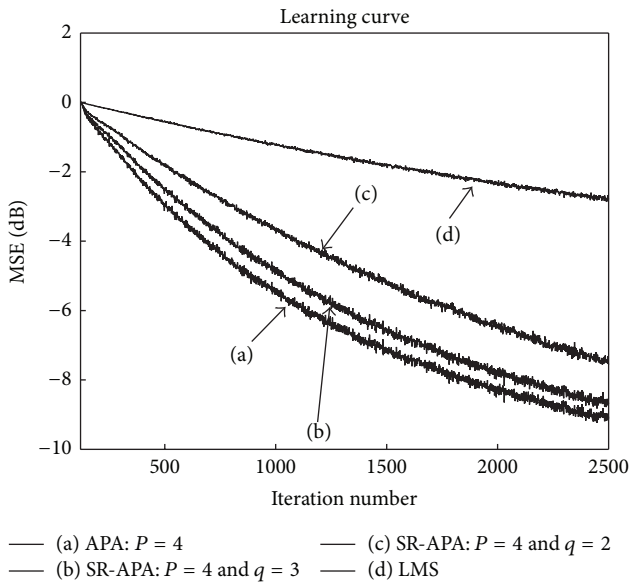

Figure 3: Learning curves for the LMS, APA, and SR-APA with $\mu = 10^{-9}$ for LMS and $\mu = 0.1$ and $P = 4$ for APA and SR-APA.

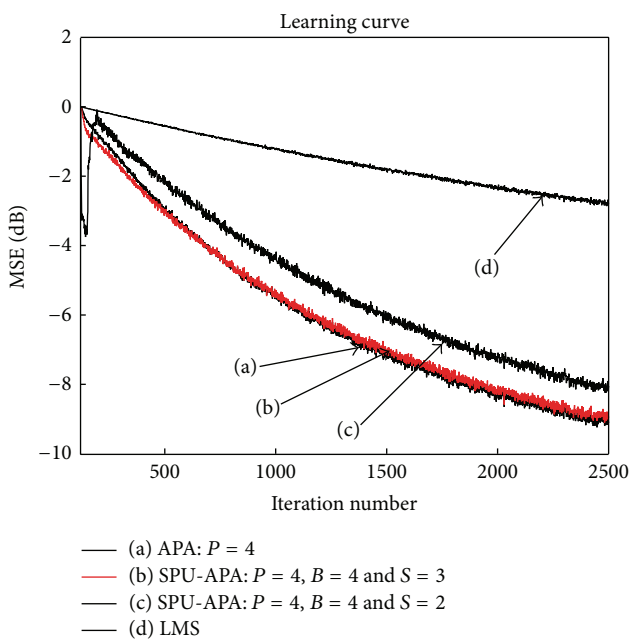

Figure 4: Learning curves for the LMS, APA, and SPU-APA with $\mu = 10^{-9}$ for LMS, $\mu = 0.1$ and $P = 4$ for APA, and $\mu = 0.1$, $P = 4$, $B = 4$, and $S = 2, 3$ for SPU-APA.

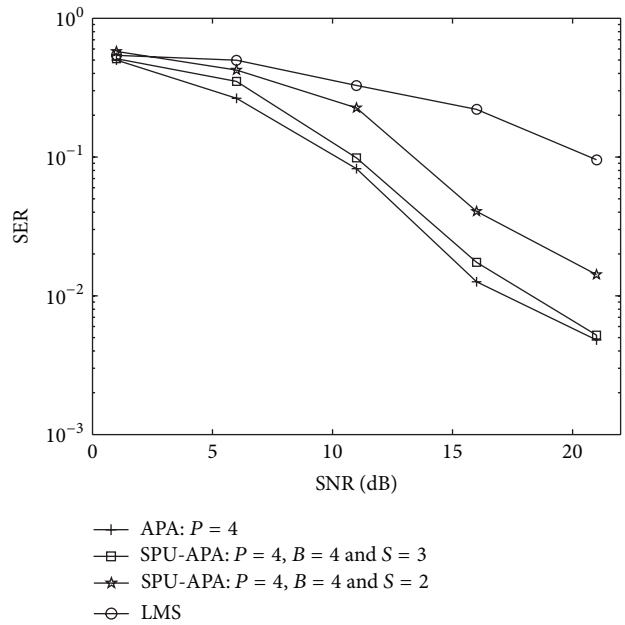

Figure 5: Symbol error rate versus SNR for APA and SPU-APA.

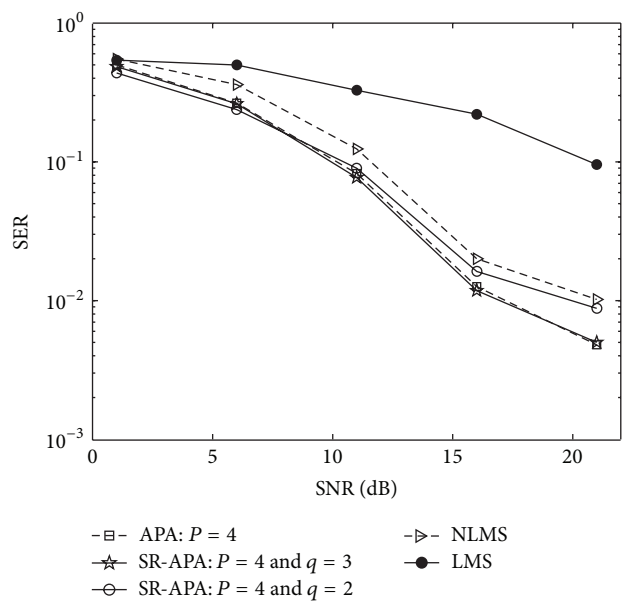

Figure 6: Symbol error rate versus SNR for APA and SR-APA.

and SR-APA, respectively. The SER of SR-APA and SPU-APA is $10e-2$, while the SER of LMS is $10e-1$ at SNR of 20 (dB).

6. Conclusion

In this paper, we have applied selective regressor affine projection algorithm (SR-APA) and selective partial update APA (SPU-APA) in shallow water channel. Also, we have compared the performances of these algorithms with the LMS and classical affine projection algorithm. These algorithms have good tradeoff between convergence rate and steady-state mean square error in comparison with APA algorithms.

Conflict of Interests

The authors declare that there is no conflict of interests regarding the publication of this paper.

References

[1] M. Stojanovic, J. A. Catipovic, and J. G. Proakis, "Phase-coherent digital communications for underwater acoustic channels," *IEEE Journal of Oceanic Engineering*, vol. 19, no. 1, pp. 100–111, 1994.

[2] M. Stojanovic, J. Catipovic, and J. G. Proakis, "Adaptive multichannel combining and equalization for underwater acoustic communications," *Journal of the Acoustical Society of America*, vol. 94, no. 3, pp. 1621–1631, 1993.

[3] Y. R. Zheng, C. Xiao, T. C. Yang, and W.-B. Yang, "Frequency-domain channel estimation and equalization for shallow-water acoustic communications," *Physical Communication*, vol. 3, no. 1, pp. 48–63, 2010.

[4] L. Freitag, M. Johnson, and M. Stojanovic, "Efficient equalizer update algorithms for acoustic communication channels of varying complexity," in *Proceedings of the IEEE Conference on Oceans*, pp. 580–585, October 1997.

[5] T. Schertler, "Selective block update of NLMS type algorithms," in *Proceedings of the International Conference on Acoustics, Speech and Signal Processing (ICASSP '98)*, pp. 1717–1720, Seattle, Wash, USA, May 1998.

[6] K. Dogançay and O. Tanrikulu, "Adaptive filtering algorithms with selective partial updates," *IEEE Transactions on Circuits and Systems II: Analog and Digital Signal Processing*, vol. 48, no. 8, pp. 762–769, 2001.

[7] S. Werner, M. L. R. de Campos, and P. S. R. Diniz, "Partial-update NLMS algorithms with data-selective updating," *IEEE Transactions on Signal Processing*, vol. 52, no. 4, pp. 938–949, 2004.

[8] S. C. Douglas, "Analysis and implementation of the max-NLMS adaptive filter," in *Proceedings of the 29th Asimolar Conference on Signals, Systems and Computers*, pp. 659–663, Pacific Grove, Calif, USA, October 1995.

[9] T. Aboulnasr and K. Mayyas, "Selective coefficient update of gradient-based adaptive algorithms," in *Proceedings of the International Conference on Acoustics, Speech, and Signal Processing*, pp. 1929–1932, Munich, Germany, April 1997.

[10] G. L. Sicuranza and A. Carini, "Filtered-X affine projection algorithm for multichannel active noise control using second-order Volterra filters," *IEEE Signal Processing Letters*, vol. 11, no. 11, pp. 853–857, 2004.

[11] S. G. Sankaran and A. A. Beex, "Normalized LMS algorithm with orthogonal correction factors," in *Proceedings of the 31st Asilomar Conference on Signals, Systems & Computers*, pp. 1670–1673, November 1997.

[12] S. G. Kratzer and D. R. Morgan, "The partial-rank algorithm for adaptive beamforming," in *Real-Time Signal Processing VIII*, vol. 0564 of *Proceedings of SPIE*, pp. 9–14, 1985.

[13] K.-Y. Hwang and W.-J. Song, "An affine projection adaptive filtering algorithm with selective regressors," *IEEE Transactions on Circuits and Systems II: Express Briefs*, vol. 54, no. 1, pp. 43–46, 2007.

[14] H. Medwin and C. S. Clay, *Fundamentals of Acoustical Oceanography*, Academic Press, San Diego, Calif, USA, 1998.

[15] R. P. Hodges, *Underwater Acoustics Analysis, Design and Performance of Sonar*, John Wiley & Sons, New York, NY, USA.

[16] L. M. Brekhovskikh and Y. Lysanov, *Fundamentals of Ocean Acoustics*, Springer, Berlin, Germany, 3rd edition, 2003.

Hindawi Publishing Corporation
Shock and Vibration
Volume 2014, Article ID 164542, 5 pages
http://dx.doi.org/10.1155/2014/164542

Research Article

Dynamic Pull-In Investigation of a Clamped-Clamped Nanoelectromechanical Beam under Ramp-Input Voltage and the Casimir Force

Amir R. Askari and Masoud Tahani

Department of Mechanical Engineering, Ferdowsi University of Mashhad, Mashhad 91775-1111, Iran

Correspondence should be addressed to Amir R. Askari; amaskari@gmail.com

Received 19 October 2012; Accepted 19 November 2012; Published 14 May 2014

Academic Editor: Hamid Mehdigholi

The influence of the Casimir excitation on dynamic pull-in instability of a nanoelectromechanical beam under ramp-input voltage is studied. The ramp-input actuation has applications in frequency sweeping of RF-N/MEMS. The presented model is nonlinear due to the inherent nonlinearity of electrostatics and the Casimir excitations as well as the geometric nonlinearity of midplane stretching. A Galerkin based reduced order modeling is utilized. It is found that the calculated dynamic pull-in ramp input voltage leads to dynamic pull-in step input voltage by increasing the slope of voltage-time diagram. This fact is utilized to verify the results of present study.

1. Introduction

Nano/microelectromechanical systems (N/MEMS) are mostly used as sensors and actuators. Because of their small size, low power consumption, and the reliability of batch fabrications, there are lots of potential applications in engineering. Clamped-clamped microbeams represent major structural components and play crucial roles in these systems. One of the most important phenomena associated with electrostatically actuated N/MEMS is pull-in instability which occurs when input voltage exceeds its critical value. In this manner, the movable part is suddenly collapsed toward the substrate. This phenomenon was observed experimentally by many researchers. Nathanson et al. [1] and Taylor [2] have investigated this phenomenon experimentally. This instability can occur in both static and dynamic circumstances. If the rate of applied voltage is negligible, the static pull-in instability may be observed; otherwise, one can observe DC dynamic pull-in.

At the nanoscale, the intermolecular forces significantly influence dynamics of nanobeams. The Casimir effect is the most important force at the scale of N/MEMS. It represents attractive force between two flat parallel plates of solids that arises from quantum fluctuations in the ground state of the electromagnetic field [3]. The Casimir interaction becomes operative at separations less than several micrometers and above 20 nm [4]. The influence of Casimir force on the pull-in instability of nano- and microsystems has been investigated by many researchers. Lin and Zhao [5] studied the influence of the Casimir force on static pull-in behaviour of nano-electromechanical systems using lumped model. Ramezani et al. [6] proposed a distributed parameter model to study the static pull-in instability of nanocantilevers subjected to intermolecular and electrostatic forces. They transferred nonlinear differential equation of the model into the integral form by using Green's function of the cantilever beam. Koochi et al. [7] investigated the effect of the Casimir attraction on the nonlinear pull-in behaviour of cantilever and double cantilever NEMS using modified Adomian decomposition method (MAD). They neglected the effect of inertia and the von Kármán nonlinearity; in other words, they have investigated the static pull-in case. Dynamic pull-in instability of electrically actuated microbeams in presence of the Casimir force has been investigated by Moghimi Zand and Ahmadian [8]. They consider the von Kármán nonlinearity of midplane stretching, applied axial loading, fringing field effect, and the

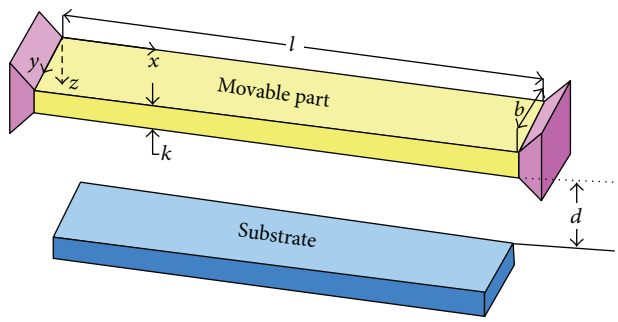

Figure 1: Schematic of a ramp-input voltage actuated clamped-clamped nano/microbeam under the effect of Casimir force.

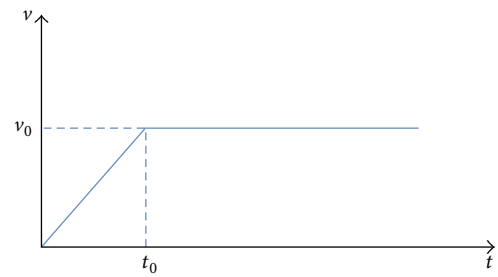

Figure 2: Ramp-input voltage.

Casimir attraction and solved the governing equation using nonlinear finite element method (NFEM).

Most of the studies on microstructures have been performed using step-input and harmonic actuations. However, other actuation shapes also have application in microstructures. Ramp-input actuation has applications in frequency sweeping and contact time study of RF-MEMS. Contact time is defined as the time taken by a microstructure to move from the initial position to the position where the deformable part contacts the substrate. It is noted that the interaction of Casimir force and ramp voltage excitation has not been investigated to date.

In present study, the governing equation of motion of nano/microbeams under the combined effect of electrostatic excitation due to ramp-input voltage and the Casimir force has been derived. This model is nonlinear due to the inherent nonlinearity of electrostatic excitation, Casimir attraction, and the geometric nonlinearity of the von Kármán midplane stretching. A numerical analytical method based on Galerkin reduced order modelling has been used to convert the partial differential equation of motion to a set of ordinary differential equations in order to investigate the nonlinear response of double clamped nano/microbeams. The results are in good agreement with those presented in the literature for dynamic pull-in case due to the step input voltage.

2. Modelling and Formulation

Consider a fully clamped nano/microbeam of length l, width b, thickness k, and density ρ under the combined action of the electrostatic excitation due to ramp-input voltage and the Casimir force (Figure 1). The distance between the beam and the stationary electrode is d. Also, x, y, and z are, respectively, the coordinate along the length, width, and thickness. W is deflection, t is time, I is the moment of inertia of the cross-section about the y axis, ν is Poisson's ratio, and E is the effective Young modulus of the nano/microbeam which is replaced by $E/(1-\nu^2)$ when $b > 5k$.

The electrostatic excitation by ramp-input DC voltage v_{DC} per unit length of the beam can be expressed as

$$F_{es} = \frac{\varepsilon b v_{DC}^2}{2(d-W)^2}, \tag{1}$$

where

$$v_{DC} = \frac{v_0}{t_0} t U(t_0 - t) + v_0 U(t - t_0), \tag{2}$$

where v_0 is the maximum value of input voltage and t_0 is the duration in which this voltage is applied (see Figure 2) and $U(t)$ is the unit step function.

The Casimir force per unit length of the beam takes the following form [9]:

$$f_{cas} = \frac{\pi^2 \hbar c b}{240(d-W)^4}, \tag{3}$$

where ε is dielectric constant of medium, $\hbar = 1.055 \times 10^{-34}$ J is Planck's constant divided by 2π, and $c = 2.998 \times 10^8$ m/s is the speed of light in vacuum.

Due to the elongation of fixed-fixed nano/microbeam which is called the midplane stretching effect and the mismatch of both thermal expansion coefficient and crystal lattice period between substrate and microbeam film which is unavoidable in surface micromachining techniques, the resultant axial force is applied to the nano/microbeam [10]:

$$F_{axial} = F_r + F_a. \tag{4}$$

The axial force due to the midplane stretching effect takes the following form [11]:

$$F_a = \frac{Ebk}{2l} \int_0^1 W'^2 dx \tag{5}$$

and the one due to the residual stress can be defined as

$$F_r = \sigma_r b k. \tag{6}$$

So the equation of motion of the clamped-clamped nano/microbeam subjected to the combined effect of ramp-input voltage and the Casimir force is as follows:

$$\begin{aligned} &EIW'''' + f\dot{W} + \rho b k \ddot{W} \\ &\quad = \left(F_r + \frac{Ebk}{2l}\int_0^1 W'^2 dx\right) W'' + F_{es} + F_{cas}, \end{aligned} \tag{7}$$

where dot and prime signs denote derivatives with respect to t and x, respectively, f is equivalent viscose damping coefficient per unit length of the beam due to squeeze film

damping [12]. The nano/microbeam deflection is subjected to the following kinematic boundary conditions:

$$W(0,t)=0; \qquad \frac{\partial W(0,t)}{\partial x}=0;$$
$$W(l,t)=0; \qquad \frac{\partial W(l,t)}{\partial x}=0. \tag{8}$$

The initial conditions are assumed as follows:

$$W(x,0)=0; \qquad \frac{\partial W(x,0)}{\partial t}=0. \tag{9}$$

For convenience, the following dimensionless variables are introduced:

$$\widehat{W}=\frac{W}{d}; \qquad \widehat{x}=\frac{x}{l}; \qquad \widehat{t}=\frac{t}{\widetilde{t}}, \tag{10}$$

where

$$\widetilde{t}=\sqrt{\frac{\rho bkl^4}{EI}}. \tag{11}$$

Upon substitution of the dimensionless quantities given in (10) into (7) and *dropping the hats*, one would get

$$W''''+\ddot{W}+C_{\text{non}}\dot{W}=\left[\alpha_1\int_0^1 W'^2dx+N\right]W''+\frac{\beta(t)}{(1-W)^2}+\frac{\lambda_4}{(1-W)^4}, \tag{12}$$

where

$$\beta(t)=\frac{\beta_0}{t_{\text{non}}}tU(t_{\text{non}}-t)+\beta_0U(t-t_{\text{non}}), \tag{13}$$

where for rectangular cross-section one can obtain

$$C_{\text{non}}=\frac{12fl^4}{Ebk^3\widetilde{t}}; \qquad \alpha_1=6\left(\frac{d}{k}\right)^2; \qquad N=\frac{12F_rl^2}{Ebk^3};$$
$$\beta_0=\frac{6\varepsilon v_{\text{DC}}^2l^4}{Ek^3d^3}; \qquad \lambda_4=\frac{12l^4\pi^2\hbar c}{240Ek^3d^5}; \tag{14}$$
$$\alpha_3=\frac{12\rho a_0l^4}{Edk^2}; \qquad t_{\text{non}}=\frac{t_0}{\widetilde{t}}.$$

3. Solution Procedure

Herein the Galerkin based reduced order modelling is used in order to solve the nonlinear partial differential equation (12) [13]. To this aim, (12) is discretized into a finite degree of freedom system consisting of ordinary differential equations in time. The undamped modeshape of straight clamped-clamped nano/microbeam is used as a basis function in Galerkin procedure. To this end, the deflection is expressed as

$$W(x,t)=\sum_{i=1}^{M}\varphi_i(x)u_i(t), \tag{15}$$

where $u_i(t)$ is the ith generalized coordinate and $\varphi_i(x)$ is the ith linear undamped modeshape of the straight clamped-clamped nano/microbeam, normalized such that $\int_0^1\varphi_i\varphi_j=\delta_{ij}$ and expressed as [14]

$$\varphi_i(x)=\cosh\left(\sqrt{\omega_i}x\right)-\cos\left(\sqrt{\omega_i}x\right)-\sigma_n\left[\sinh\left(\sqrt{\omega_i}x\right)-\sin\left(\sqrt{\omega_i}x\right)\right], \tag{16}$$

where σ_n is defined as

$$\sigma_n=\frac{\sinh\left(\sqrt{\omega_i}\right)+\sin\left(\sqrt{\omega_i}\right)}{\cosh\left(\sqrt{\omega_i}\right)-\cos\left(\sqrt{\omega_i}\right)} \tag{17}$$

and ω_i is the ith nondimensional natural frequency of the nano/microbeam and governed by

$$\cos\left(\sqrt{\omega_i}\right)\cosh\left(\sqrt{\omega_i}\right)=1. \tag{18}$$

Next we multiply (12) by $\varphi_n(x)\cdot(1-W)^4$, substitute (15) into the resulting equation, integrate the outcome from $x=0$ to 1, use integration by parts, and obtain

$$\begin{aligned}
&\ddot{u}_n+C_{\text{non}}\dot{u}_n+\left[\omega_n^2+2\beta\right]u_n-\left[\beta+\lambda_4\right]\int_0^1\varphi_ndx\\
&-4\sum_{i,j=1}^{M}\omega_i^2u_iu_j\int_0^1\varphi_i\varphi_j\varphi_ndx+6\sum_{i,j,k=1}^{M}\omega_i^2u_iu_ju_k\\
&\times\int_0^1\varphi_i\varphi_j\varphi_k\varphi_ndx-4\sum_{i,j,k,m=1}^{M}\omega_i^2u_iu_ju_ku_m\\
&\times\int_0^1\varphi_i\varphi_j\varphi_k\varphi_m\varphi_ndx+\sum_{i,j,k,m,p=1}^{M}\omega_i^2u_iu_ju_ku_mu_p\\
&\times\int_0^1\varphi_i\varphi_j\varphi_k\varphi_m\varphi_p\varphi_ndx-4\sum_{i,j=1}^{M}\ddot{u}_iu_j\\
&\times\int_0^1\varphi_i\varphi_j\varphi_ndx+6\sum_{i,j,k=1}^{M}\ddot{u}_iu_ju_k\int_0^1\varphi_i\varphi_j\varphi_k\varphi_ndx\\
&-4\sum_{i,j,k,m=1}^{M}\ddot{u}_iu_ju_ku_m\int_0^1\varphi_i\varphi_j\varphi_k\varphi_m\varphi_ndx\\
&+\sum_{i,j,k,m,p=1}^{M}\ddot{u}_iu_ju_ku_mu_p\int_0^1\varphi_i\varphi_j\varphi_k\varphi_m\varphi_p\varphi_ndx
\end{aligned}$$

$$
\begin{aligned}
&- 4C_{\text{non}} \sum_{i,j=1}^{M} \dot{u}_i u_j \int_0^1 \varphi_i \varphi_j \varphi_n dx + 6C_{\text{non}} \sum_{i,j,k=1}^{M} \dot{u}_i u_j u_k \\
&\times \int_0^1 \varphi_i \varphi_j \varphi_k \varphi_n dx - 4C_{\text{non}} \sum_{i,j,k,m=1}^{M} \dot{u}_i u_j u_k u_m \\
&\times \int_0^1 \varphi_i \varphi_j \varphi_k \varphi_m \varphi_n dx + C_{\text{non}} \sum_{i,j,k,m,p=1}^{M} \dot{u}_i u_j u_k u_m u_p \\
&\times \int_0^1 \varphi_i \varphi_j \varphi_k \varphi_m \varphi_p \varphi_n dx + \alpha_1 \sum_{i,j,k=1}^{M} u_i u_j u_k \\
&\times \Gamma\left(\varphi_i, \varphi_j\right) \Gamma\left(\varphi_k, \varphi_n\right) + 4\alpha_1 \sum_{i,j,k,m=1}^{M} u_i u_j u_k u_m \Gamma\left(\varphi_i, \varphi_j\right) \\
&\times \int_0^1 \varphi_k'' \varphi_m \varphi_n dx - 6\alpha_1 \sum_{i,j,k,m,p=1}^{M} u_i u_j u_k u_m u_p \\
&\times \Gamma\left(\varphi_i, \varphi_j\right) \int_0^1 \varphi_k'' \varphi_m \varphi_p \varphi_n dx + 4\alpha_1 \\
&\times \sum_{i,j,k,m,p,q=1}^{M} u_i u_j u_k u_m u_p u_q \Gamma\left(\varphi_i, \varphi_j\right) \int_0^1 \varphi_k'' \varphi_m \varphi_p \varphi_q \varphi_n dx \\
&- \alpha_1 \sum_{i,j,k,m,p,q,l=1}^{M} u_i u_j u_k u_m u_p u_q u_l \Gamma\left(\varphi_i, \varphi_j\right) \\
&\times \int_0^1 \varphi_k'' \varphi_m \varphi_p \varphi_q \varphi_l \varphi_n dx + N \sum_{i=1}^{M} u_i \Gamma\left(\varphi_i, \varphi_n\right) \\
&+ 4N \sum_{i,j=1}^{M} u_i u_j \int_0^1 \varphi_i'' \varphi_j \varphi_n dx - 6N \sum_{i,j,k=1}^{M} u_i u_j u_k \\
&\times \int_0^1 \varphi_i'' \varphi_j \varphi_k \varphi_n dx + 4N \sum_{i,j,k,m=1}^{M} u_i u_j u_k u_m \\
&\times \int_0^1 \varphi_i'' \varphi_j \varphi_k \varphi_m \varphi_n dx - N \sum_{i,j,k,m,p=1}^{M} u_i u_j u_k u_m u_p \\
&\times \int_0^1 \varphi_i'' \varphi_j \varphi_k \varphi_m \varphi_p \varphi_n dx - \beta \sum_{i,j=1}^{M} u_i u_j \int_0^1 \varphi_i \varphi_j \varphi_n dx = 0,
\end{aligned}
\tag{19}
$$

where the function $\Gamma(\varphi_i, \varphi_j)$ is given by

$$
\Gamma\left(\varphi_i, \varphi_j\right) = \int_0^1 \varphi_i' \varphi_j' dx. \tag{20}
$$

Equation (19) represents an implicit system of M nonlinear second order ordinary differential equations. Using an implicit scheme such as Adams-Moulton implicit methods [15] or transforming them into an explicit system in $\ddot{u}_n$ by multiplying (19) with the inverse of the coefficients of $\ddot{u}_n$ and using fourth order Runge-Kutta method may lead to the solution of (19). The latter approach was used in the present calculations.

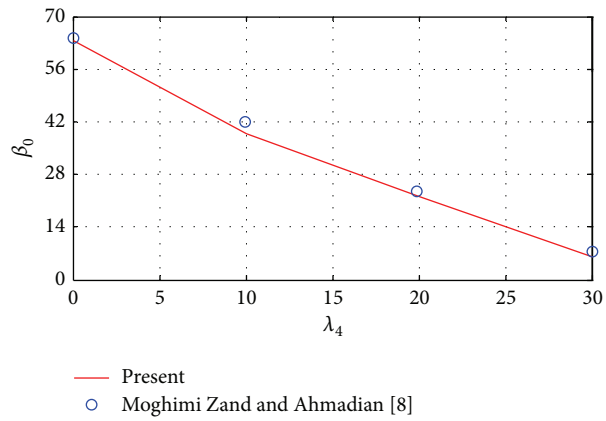

Figure 3: Nondimensional Casimir parameter versus the nondimensional parameter of maximum value for the case in which $\alpha_1 = 6$, $N = 0$, $C_{\text{non}} = 0$, and $t_0 = 10^{-7}$ sec.

4. Results and Discussion

Assuming that the only dominant mode in the response of the nano/microbeam is its first mode (i.e., $M = 1$), so using the single mode approximation may lead to accurate results. In order to validate the model, the results are compared with those presented in the literature for DC dynamic pull-in case in which the Casimir effect has been taken into account [8]. For this aim we set $\alpha_1 = 6$, $N = 0$, $C_{\text{non}} = 0$, and $t_0 = 10^{-7}$ sec, then plot the nondimensional max voltage parameter β_0 versus nondimensional Casimir force parameter λ_4, and compare the outcome with the results of Moghimi Zand and Ahmadian [8] (see Figure 3).

Consider a polysilicon microbeam with length $l = 900\,\mu$m, thickness $k = 1.5\,\mu$m, width $b = 100\,\mu$m and gap width $d = 2\,\mu$m. The material properties of this microbeam are $\nu = 0.28$, $E = 169$ GPa which is replaced by $E/(1-\nu^2)$ because $b > 5k$, and $\rho = 2332$ Kg/m^3. The DC dynamic pull-in step voltage for this case without considering damping coefficient and Casimir effect is 3.11 V. The response of this microbeam under ramp-input voltage with and without considering the effect of Casimir force before and after bechancing pull-in instability is plotted in Figure 4. From this figure, one can observe the major effect of Casimir force on nano/microstructures.

Figure 4 illustrated that neglecting the effect of Casimir force on nano/microstructures may lead to very inaccurate results, so it is very important to consider this effect when the nondimensional Casimir parameter (λ_4) takes noticeable values.

5. Conclusion

In the present paper, reduced order modelling based on the Galerkin procedure was utilized to study the effect

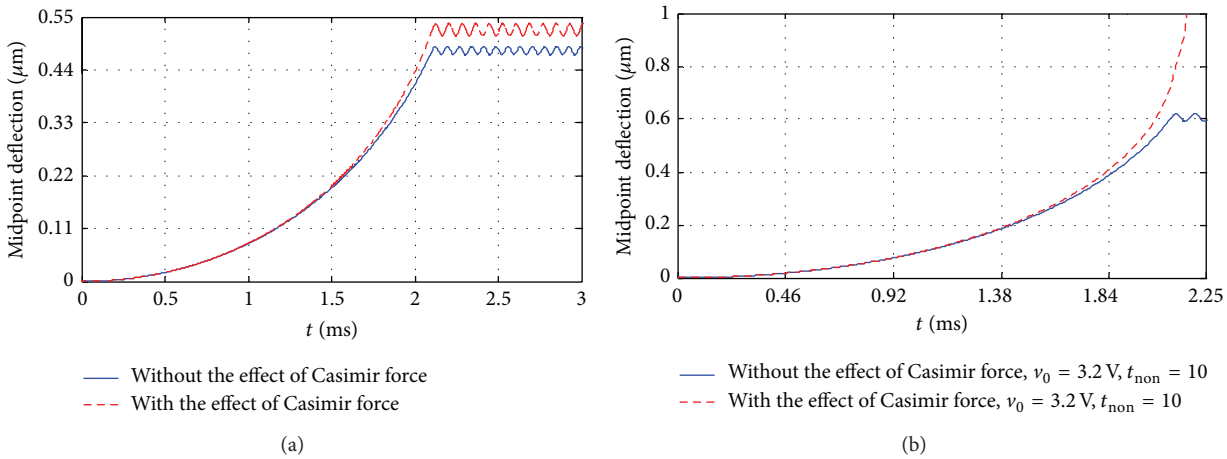

FIGURE 4: The response of polysilicon microbeam under combined effect of ramp-input voltage and the Casimir force force. (a) $v_0 = 3$ V, $t_{non} = 10$ and (b) $v_0 = 3.2$ V, $t_{non} = 10$.

of Casimir attraction on the response of a fully clamped nano/microbeam under ramp-input voltage. The model accounted for geometric nonlinearity of von Kármán midplane stretching, applied axial loading, equivalent viscose damping, and inherent nonlinearity of distributed electrostatic and Casimir forces. It was found that considering the Casimir force may lead to early instability in nano/microelectromechanical devices through dynamic pull-in.

Conflict of Interests

The authors declare that there is no conflict of interests regarding the publication of this paper.

References

[1] H. C. Nathanson, W. E. Newell, R. A. Wickstrom, and J. R. Davis, "The resonant gate transistor," *IEEE Transactions on Electron Devices*, vol. 14, no. 3, pp. 117–133, 1967.

[2] G. I. Taylor, "The coalescence of closely spaced drops when they are at different electric potentials," *Proceedings of the Royal Society A*, vol. 306, pp. 423–434, 1968.

[3] H. B. G. Casimir, "On the attraction between two perfectly conducting plates," in *Proceedings of the Koninklijke Nederlandse Akademie van Wetenschappen*, vol. 51, pp. 793–795, 1948.

[4] F. M. Serry, D. Walliser, and G. J. Maclay, "Anharmonic casimir oscillator (ACO)—the casimir effect in a model microelectromechanical system," *Journal of Microelectromechanical Systems*, vol. 4, no. 4, pp. 193–205, 1995.

[5] W.-H. Lin and Y.-P. Zhao, "Nonlinear behavior for nanoscale electrostatic actuators with Casimir force," *Chaos, Solitons and Fractals*, vol. 23, no. 5, pp. 1777–1785, 2005.

[6] A. Ramezani, A. Alasty, and J. Akbari, "Closed-form solutions of the pull-in instability in nano-cantilevers under electrostatic and intermolecular surface forces," *International Journal of Solids and Structures*, vol. 44, no. 14-15, pp. 4925–4941, 2007.

[7] A. Koochi, A. S. Kazemi, Y. Tadi Beni, A. Yekrangi, and M. Abadyan, "Theoretical study of the effect of Casimir attraction on the pull-in behavior of beam-type NEMS using modified Adomian method," *Physica E*, vol. 43, no. 2, pp. 625–632, 2010.

[8] M. Moghimi Zand and M. T. Ahmadian, "Dynamic pull-in instability of electrostatically actuated beams incorporating Casimir and van der Waals forces," *Journal of Mechanical Engineering Science*, vol. 224, no. 9, pp. 2037–2047, 2010.

[9] S. K. Lamoreaux, "The Casimir force: background, experiments, and applications," *Reports on Progress in Physics*, vol. 68, no. 1, pp. 201–236, 2005.

[10] J. Qian, C. Liu, D. Zhang, and Y. Zhao, "Residual stresses in micro-electro-mechanical systems," *Journal of Mechanical Strength*, vol. 23, no. 4, pp. 393–401, 2001.

[11] L. D. Landau and E. M. Lifshitz, *Theory of Elasticity*, Pergamon Press, New York, NY, USA, 1986.

[12] A. H. Nayfeh and M. I. Younis, "A new approach to the modeling and simulation of flexible microstructures under the effect of squeeze-film damping," *Journal of Micromechanics and Microengineering*, vol. 14, no. 2, pp. 170–181, 2004.

[13] M. I. Younis, E. M. Abdel-Rahman, and A. Nayfeh, "A reduced-order model for electrically actuated microbeam-based MEMS," *Journal of Microelectromechanical Systems*, vol. 12, no. 5, pp. 672–680, 2003.

[14] B. Balachandran and E. Magrab, *Vibrations*, Cengage Learning, Toronto, Canada, 2nd edition, 2009.

[15] J. D. Faires and R. L. Burden, *Numerical Methods*, Faires and Burden, Brooks/Cole, 3rd edition, 2002.